

DIELECTRIC PHENOMENA OF OXIDES WITH FLUORITE RELATED SUPER
STRUCTURES

By

CHRISTOPHER GEORGE TURNER

A DISSERTATION PRESENTED TO THE GRADUATE SCHOOL
OF THE UNIVERSITY OF FLORIDA IN PARTIAL FULFILLMENT
OF THE REQUIREMENTS FOR THE DEGREE OF
DOCTOR OF PHILOSOPHY

UNIVERSITY OF FLORIDA

2014

© 2014 Christopher Turner

To my parents, friends and everyone who helped me push through the last four years

ACKNOWLEDGMENTS

First, I would like to thank my advisor Dr. Juan C. Nino for his support and guidance. He gave me the opportunity to conduct research that always challenged me and through his knowledge and support allowed me to thoroughly enjoy my time in and out of the lab.

I would also like to thank my parents for helping me get to where I am today. It has always been comforting to know that no matter how bad or great of a day I had they would always be there to love and support me. My brothers have also been a fantastic support throughout my graduate study by giving me a distraction from work every once in a while.

Kathleen Moffitt has also been one of my biggest supporters, especially in times of high stress she was always there to calm my nerves. Her love and support through the proposal defense, thesis writings, and her ability to listen to my science filled day was just the thing I needed in my life and I only wish I had met you sooner.

I would like to thank all my friends who came to visit every football season and gave me a reason to take Saturdays off every Fall. Your support was always appreciated and a special shout out to my roommates Mo and Trey for putting up with my strange hours and letting me burn things in the kitchen every once in a while.

There have also been a number of students and professors who have helped me with my research that deserve special mention, and they are as follows: Dr. David Tanner and Evan Thatcher (IR), Dr. Beverly Hinojosa (DFT), Dr. Brendan Kennedy (Neutron), and Dr. Matt Suchomel (APS).

The friends at turntable.fm for providing constant music for the day and encouraging me throughout, thanks Indie Mix.

I would not have been able to get this far without the considerable help of previous and current Nino research group members. When I first came in they answered any and all questions I had and then later I then became the source of answers for younger members. I would like to give a special thanks to the following people: Roberto Esquivel for letting me tag along the $\text{Bi}_2\text{Ti}_2\text{O}_7$ synthesis process (even though he wasn't any good at lab basketball), Beverly Hinojosa for being fantastic help in understanding anything to do with crystallography, the magic of theoretical experiments, and the joys and wonders of being in charge of purchasing, Trey Davis while also having to live with me also had the added benefit of dealing with me at work, Alex Arias for teaching me all the basics of dielectrics that I was able to build on, Don Moore, Paul Johns, Hyuksu Han, Brittnee Mound, George Baure, Mehrad Mehr, Soumitra Sulekar, Bryce Edwards, and all of the other undergraduate members who helped me along. Apart from the science and work I will always carry the memories of the off-time at UF. Whether it was Ninolympics, Lab Basketball, Lab Office Darts, It's Kind of a Big Deal Friday, Food Truck Friday, and just everyday laughs to break up the monotony of writing a paper (and thesis).

TABLE OF CONTENTS

	<u>page</u>
ACKNOWLEDGMENTS.....	4
LIST OF TABLES.....	9
LIST OF FIGURES.....	10
LIST OF ABBREVIATIONS.....	13
LIST OF SYMBOLS	14
ABSTRACT	16
CHAPTER	
1 INTRODUCTORY REMARKS	18
1.1 Statement of Problem and Motivation.....	18
1.2 Scientific Approach	19
1.3 Organization of Dissertation.....	21
1.4 Contributions to the Field.....	23
2 BACKGROUND	25
2.1 Fluorite Related Superstructures	25
2.1.1 The pyrochlore structure.....	25
2.1.2 The defect-fluorite structure.....	29
2.2 The Bond Valence Model.....	30
2.3 Polarization Mechanisms	31
2.3.1 Electronic polarization	32
2.3.2 Ionic polarization	34
2.3.3 Dipolar polarization.....	35
2.3.4 Space charge polarization	38
2.3.5 The dielectric spectrum	38
2.4 Dielectric Relaxation in Pyrochlores.....	39
2.5 Vibrational Spectroscopy	42
2.5.1 Normal mode determination	42
2.5.2 Raman scattering	43
2.5.3 Infrared absorption	43
3 EXPERIMENTAL PROCEDURES AND PROCESSING.....	45
3.1 Bi ₂ Ti ₂ O ₇ Synthesis	45
3.1.1 Powder synthesis	45
3.1.2 Pellet formation	45

3.2	Solid State Synthesis	46
3.2.1	Powder synthesis	46
3.2.2	Pellet formation	47
3.3	Characterization.....	48
3.3.1	Structural characterization.....	48
3.3.2	Infrared and Raman characterization	49
3.3.3	Dielectric characterization	49
3.4	Computational Methods	50
4	CRYSTALLOGRAPHY OF $\text{Bi}_2\text{Ti}_2\text{O}_7$ AND OTHER PYROCHLORES	52
4.1	Introduction	52
4.2	Crystal Structure of $(\text{Sm}_x\text{Yb}_{1-x})_2\text{Ti}_2\text{O}_7$ ($x = 0.25, 0.5, 0.75$).....	53
4.3	Crystal Structure of $\text{Sm}_2(\text{Sn}_{0.5}\text{Ti}_{0.5})_2\text{O}_7$	55
4.4	Structural Study of $\text{Bi}_2\text{Ti}_2\text{O}_7$	56
4.4.1	Synchrotron X-ray diffraction	57
4.4.2	Neutron diffraction	60
4.4.3	DFT calculations.....	63
4.5	Conclusion.....	66
5	DIELECTRIC PROPERTIES OF $\text{Bi}_2\text{Ti}_2\text{O}_7$ AND OTHER PYROCHLORES	67
5.1	Introduction	67
5.2	Dielectric Analysis of $\text{Bi}_2\text{Ti}_2\text{O}_7$	69
5.2.1	Dielectric analysis as a function of temperature	69
5.2.2	Dielectric analysis as a function of frequency	74
5.3	Dielectric properties of the $(\text{Sm}_x\text{Yb}_{1-x})_2\text{Ti}_2\text{O}_7$ and $\text{Sm}_2(\text{Sn}_x\text{Ti}_{1-x})_2\text{O}_7$ system.....	79
5.3.1	Dielectric analysis of $(\text{Sm}_x\text{Yb}_{1-x})_2\text{Ti}_2\text{O}_7$ ($x = 0.25, 0.5, 0.75$).....	79
5.3.2	Dielectric analysis of $\text{Sm}_2(\text{Sn}_{0.5}\text{Ti}_{0.5})_2\text{O}_7$	81
5.4	Conclusion	82
6	RAMAN AND IR PROPERTIES OF $\text{Bi}_2\text{Ti}_2\text{O}_7$	83
6.1	Introduction	83
6.2	Raman Spectroscopy.....	86
6.3	Infrared Spectroscopy.....	94
6.3.1	Reflectance spectra.....	94
6.3.2	Kramers-Kronig analysis	95
6.3.3	Oscillator-model analysis.....	97
6.4	Conclusion	101
7	ORIGIN OF DIELECTRIC RELAXATION IN PYROCHLORES	102
7.1	Introduction	102
7.2	Discussion	103
7.3	Conclusion.....	110
8	DIELECTRIC PROPERTIES OF TYPE-II Bi_3NbO_7	112

8.1 Introduction	112
8.2 Dielectric Spectroscopy	113
8.3 Defect Fluorite Structure-Dielectric Property Relationship	116
8.4 Conclusion	125
9 DIELECTRIC RESPONSE AND PHASE TRANSITION OF Gd_3NbO_7	126
9.1 Introduction	126
9.2 Results and Discussion.....	127
9.3 Conclusion.....	133
10 SUMMARY AND FUTURE WORK	135
10.1 Summary	135
10.2 Future Work	137
APPENDIX	
A EQUIVALENT CIRCUIT ANALYSIS OF $Bi_2Ti_2O_7$	139
A.1 Introduction	139
A.2 Equivalent Circuit Analysis.....	140
B $Bi_2Ti_2O_7$ TEMPERATURE EFFECTS ON STRUCTURE AND DIELECTRIC PROPERTIES.....	147
LIST OF REFERENCES	149
BIOGRAPHICAL SKETCH.....	163

LIST OF TABLES

<u>Table</u>	<u>page</u>
2-1 Pyrochlore ($A_2B_2O_6O'$) structure (origin choice 2) ²⁹	26
2-2 Pyrochlores and the conditions present for possible relaxation	41
3-1 The calcination and sintering times and temperatures for the solid state synthesized oxides.	47
4-1 The 2θ positions and the apparent lattice parameter of $(Sm_{0.25}Yb_{0.75})_2Ti_2O_7$	54
4-2 Lattice Parameters of $(Sm_{0.25}Yb_{0.75})_2Ti_2O_7$, $(Sm_{0.50}Yb_{0.50})_2Ti_2O_7$, and $(Sm_{0.75}Yb_{0.25})_2Ti_2O_7$	55
4-3 Refined positions and parameters of $Bi_2Ti_2O_7$ at 3 K	57
6-1 Optical modes for $Bi_2Ti_2O_7$	84
6-2 Parameters for $Bi_2Ti_2O_7$ in the Lorentzian fitting of the Raman spectra.....	90
6-3 The observed Raman vibrational mode frequencies of bismuth and titanate pyrochlores	93
6-4 Parameters for the phonon modes in the 20 K infrared spectrum of $Bi_2Ti_2O_7$. .	99
7-1 Pyrochlores and the conditions present for possible relaxation	104
7-2 New pyrochlores from this work and the conditions present for possible relaxation	105
8-1 Lattice parameters of Ln_3NbO_7 ($Ln = Dy, Er, Yb, Y$) and Bi_3NbO_7	117
9-1 Crystal data and refinement parameters of the two proposed low temperature Gd_3NbO_7	131

LIST OF FIGURES

<u>Figure</u>	<u>page</u>
1-1 Dielectric relaxation in $\text{Bi}_{1.5}\text{Zn}_{0.92}\text{Nb}_{1.5}\text{O}_{6.92}$ pyrochlore.	19
2-1 The fluorite structure of CaF_2	25
2-2 The pyrochlore structure visualization.	27
2-3 The $\text{A}_2\text{O}'$ tetrahedral and B_2O_6 octahedral networks.....	28
2-4 [001] view of pyrochlores.	29
2-5 The four main polarization mechanisms.	33
2-6 Dipolar polarization energy schematic.....	35
2-7 Frequency response of a dielectric material for dipolar polarization.	37
2-8 Real and imaginary parts of the permittivity as a function of frequency, showing the contribution from the four polarization mechanism.	39
2-9 Dielectric relaxation for BZN shown at 2MHz vs temperature.	40
4-1 XRD patterns of $(\text{Sm}_{0.25}\text{Yb}_{0.75})_2\text{Ti}_2\text{O}_7$, $(\text{Sm}_{0.50}\text{Yb}_{0.50})_2\text{Ti}_2\text{O}_7$, and $(\text{Sm}_{0.75}\text{Yb}_{0.25})_2\text{Ti}_2\text{O}_7$	53
4-2 Nelson-Riley function for the lattice parameter calculations of $(\text{Sm}_{0.25}\text{Yb}_{0.75})_2\text{Ti}_2\text{O}_7$, $(\text{Sm}_{0.50}\text{Yb}_{0.50})_2\text{Ti}_2\text{O}_7$, and $(\text{Sm}_{0.75}\text{Yb}_{0.25})_2\text{Ti}_2\text{O}_7$	54
4-3 XRD patterns of $\text{Sm}_2(\text{Sn}_{0.25}\text{Ti}_{0.75})_2\text{O}_7$, $\text{Sm}_2(\text{Sn}_{0.5}\text{Ti}_{0.5})_2\text{O}_7$, and $\text{Sm}_2(\text{Sn}_{0.75}\text{Ti}_{0.25})_2\text{O}_7$	56
4-4 High resolution XRD at temperatures from 6 k to 250 K.....	58
4-5 Rietveld fit of the room temperature x-ray diffraction pattern.....	59
4-6 The lattice parameter between 6 K and 150 K	60
4-7 Rietveld fit of the room temperature neutron diffraction pattern.....	61
4-8 Temperature dependence of the lattice parameters of $\text{Bi}_2\text{Ti}_2\text{O}_7$	63
5-1 The real and imaginary part of the dielectric permittivity as a function of temperature from 10 kHz.....	70
5-2 Imaginary and real part of the dielectric permittivity as a function of temperature from 80 Hz to 2 MHz.	71

5-3	Arrhenius plot of $\text{Bi}_2\text{Ti}_2\text{O}_7$ dielectric relaxation using Equation 5-1.	72
5-4	Imaginary and real part of the dielectric permittivity as a function of temperature.	74
5-5	Frequency plots at varying temperatures of ϵ'' , M'' , Y'' , and Z''	76
5-6	Normalized functions of Z'' , Y'' , M'' , and ϵ'' at 290 K.	77
5-7	Frequency dependent plot of the real part of the dielectric permittivity.	78
5-8	Imaginary and real part of the dielectric permittivity as a function of temperature from 10kHz to 2 Mhz Sm-Compounds	80
5-9	Imaginary and real part of the dielectric permittivity as a function of temperature of $\text{Sm}_2(\text{Sn}_{0.5}\text{Ti}_{0.5})\text{O}_7$	81
6-1	Room temperature Raman spectra of $\text{Bi}_2\text{Ti}_2\text{O}_7$ powder and sintered pellet.....	87
6-2	Raman spectra fitted to a sum of Lorentzian functions.	88
6-3	Raman spectra fitted to a sum of Gaussian functions.	89
6-4	The reflectance of $\text{Bi}_2\text{Ti}_2\text{O}_7$ at temperatures between 20 and 300 K.....	94
6-5	The real part of the dielectric function (ϵ') of $\text{Bi}_2\text{Ti}_2\text{O}_7$ at temperatures between 20 and 300K.....	96
6-6	The imaginary part of the dielectric function (ϵ'') of $\text{Bi}_2\text{Ti}_2\text{O}_7$ at temperatures between 20 and 300 K.....	96
6-7	The real part of the optical conductivity (σ') of $\text{Bi}_2\text{Ti}_2\text{O}_7$ at temperatures between 20 and 300 K.....	97
7-1	The electron localization function (ELF) for a portion of the (111) plane	108
7-2	The relative energy landscape.....	109
8-1	Real and imaginary part of the permittivity of single crystal type-II Bi_3NbO_7	114
8-2	Normalized functions of the imaginary components of the impedance (Z''), admittance (Y''), modulus (M''), and permittivity (ϵ'').	115
8-3	Experimental and theoretical permittivity of type-II Bi_3NbO_7 and Ln_3NbO_7 defect fluorites.	118
8-4	TCC of defect-fluorite Ln_3NbO_7 and type-II Bi_3NbO_7 from 218 K to 350 K.....	120
8-5	BVS of Ln_3NbO_7 and type-II Bi_3NbO_7 defect fluorites	122

8-6	BSI of Ln_3NbO_7 and type-II Bi_3NbO_7 defect fluorites	123
8-7	GII of Ln_3NbO_7 and type-II Bi_3NbO_7 defect fluorites	124
9-1	Real and imaginary components of the permittivity of Gd_3NbO_7	127
9-2	Arrhenius plot of temperature of Gd_3NbO_7	129
9-2	Heat capacity of Gd_3NbO_7	130
9-3	Infrared Spectroscopy of Gd_3NbO_7 at 50 K, 300 K, and 360 K.....	130
9-4	Imaginary and real part of the permittivity of Gd_3TaO_7	132
A-1	Capacitance, C' vs frequency	141
A-2	Admittance, Y' vs frequency	142
A-3	Equivalent circuit showing different R, C, and CPE combinations.....	143
A-4	Fit of the 210K to circuit in Figure A-3A	144
A-5	Fit of the 210K to circuit in Figure A-3B	145
B-1	A comparison of the temperature anomalies found in the specific heat, neutron diffraction and dielectric permittivity.....	148

LIST OF ABBREVIATIONS

a.c.	Alternating current
ANL	Argonne National Laboratory
APS	Advanced Photon Source
ANSTO	Australian Nuclear Science and Technology Organization
BSI	Bond Strain Index
BVS	Bond Valence Sum
d.c.	Direct current
GII	Global instability Index
IR	Infrared
MLCC	Multilayer ceramic capacitors
OPAL	Open Pool Australian Reactor

LIST OF SYMBOLS

ϵ_r	Permittivity
μ	Dipole moment
δ	Distance between charges
ϵ_r'	Real permittivity
E_{loc}	Local electric field
E_{ext}	External electric field (or applied field)
m_e	Mass of an electron
Z	Atomic Number
P	Polarization
q	Charge
ω_o	Natural frequency of vibration (resonant frequency)
ω	Frequency
ϵ_o	Permittivity of free space
ζ	Damping constant (friction coefficient)
Hz	Hertz
N_{ion}	Number of ion pairs per cubic meter
ω_{ion}	The natural frequency of vibration of the ion pairs
M_r	Reduced mass of the system
ΔH_m	Energy Barrier between two equivalent sites
λ_s	Distance between two equivalent sites
N_{dip}	Number of dipoles per cubic meter
k	Boltzmann's constant ($1.3806488 \times 10^{-23} \text{ m}^2 \text{ kg s}^{-2} \text{ K}^{-1}$)
T	Temperature

P_s	Static value of polarization
τ	Relaxation time
R_{ij}	The length of the bond between atoms i and j
S_{ij}	The bond valence between atoms i and j
R_o	Standard bond distance
b	An empirically derived constant
BVS_i	The bond valence sum for ion i

Abstract of Dissertation Presented to the Graduate School
of the University of Florida in Partial Fulfillment of the
Requirements for the Degree of Doctor of Philosophy

DIELECTRIC PHENOMENA OF OXIDES WITH FLUORITE RELATED SUPER
STRUCTURES

By

Christopher George Turner

May 2014

Chair: Juan C. Nino

Major: Materials Science and Engineering

Fluorite related super structures have been extensively studied due to their attractive composition-dependent dielectric properties. A combination of their high permittivity values, low dielectric loss, and low sintering temperatures ($1000^{\circ}\text{C} \pm 150$) makes them ideal candidates for embedded capacitors. Several pyrochlores and all Bi-pyrochlores display an interesting dielectric phenomenon, dielectric relaxation. A comprehensive investigation of the dielectric phenomena of fluorite related superstructures and a study of pyrochlore relaxation is the topic of this dissertation.

A structural study of $\text{Bi}_2\text{Ti}_2\text{O}_7$ was performed using neutron diffraction, synchrotron x-ray diffraction (SXR), and DFT. Both the neutron and SXR revealed displacements of the Bi cation to the $96g$ site and the displacement of the O' oxygen. The proposed atomic displacements of the Bi and O' atoms in $\text{Bi}_2\text{Ti}_2\text{O}_7$ are similar to that observed in another bismuth pyrochlore, $\text{Bi}_{1.5}\text{Zn}_{0.92}\text{Nb}_{1.5}\text{O}_{6.92}$ (BZN).¹⁻³ Nonetheless, what is striking is that displacement would occur without atomic substitutions and multiple site occupancy like in BZN and related pyrochlores.

Raman and IR studies also suggest displacements in the atomic positions of bismuth and oxygen away from their higher symmetry conventional pyrochlore Wyckoff positions and are show strong and surprising evidence of disorder at the titanium site.

As for dielectric properties, Cubic pyrochlore $\text{Bi}_2\text{Ti}_2\text{O}_7$ was found to have a low frequency (<10 kHz) and relatively high temperature (~125 K) dielectric relaxation was observed in $\text{Bi}_2\text{Ti}_2\text{O}_7$. An Arrhenius function was used to model the relaxation behavior and yielded an activation energy of 0.162 eV and an attempt jump frequency of ~1MHz. This response is consistent with space charge polarization and not the result of dipolar or ionic disorder.

The work presented in this dissertation adds a final link to the question of what conditions are required in pyrochlores to exhibit dielectric relaxation. An in depth investigation into the structure and dielectric properties of $\text{Bi}_2\text{Ti}_2\text{O}_7$ showed that a pyrochlore displaying atomic displacements without substitution does not display relaxation. This result points suggests that substitutional cations play a major role in the origin of dielectric relaxation in pyrochlores.

CHAPTER 1 INTRODUCTORY REMARKS

1.1 Statement of Problem and Motivation

The storage of energy in materials is of great interest due to the boom in the technology industry. As devices become smaller and more integrated; efforts in the miniaturization of electronic components, such as capacitors, require new materials with improved dielectric properties.^{4,5} Materials with superior dielectric properties (high permittivity and low loss) would allow for capacitors to significantly decrease in size.^{6,7}

The fluorite structure (AO_2) is considered to be one of the most flexible structures for its ability to form superstructures or derivatives.⁸ The pyrochlore structure ($A_2B_2O_7$) can be seen as an anion-deficient fluorite-related structure that is able to maintain the closed-packed layers of cations throughout. Pyrochlores and other fluorite-related structures can accommodate various cations on both the A-site and B-site. This cation flexibility allows compounds with fluorite-related structures to exhibit interesting properties, such as: conductivity (e.g. $Gd_2Zr_2O_7$ ⁹⁻¹¹), dielectric properties (e.g. $Bi_{1.5}Zn_{0.92}Nb_{1.5}O_{6.92}$ ¹²⁻¹⁴), ferroelectric properties (e.g. $Cd_2Nb_2O_7$ ^{15,16}), magnetic properties (e.g. $Gd_2Ru_2O_7$ ^{17,18}), and photocatalytic activity (e.g. La_3NbO_7 ¹⁹)

Bismuth based pyrochlores have been extensively studied due to their attractive composition-dependent dielectric properties.^{12,20-24} A combination of their high permittivity values (usually above 100), low dielectric loss, and low sintering temperatures ($1000^\circ\text{C} \pm 150$) makes them ideal candidates for embedded capacitors and multilayer ceramic capacitors (MLCC). Several pyrochlores and most Bi-pyrochlores display an interesting dielectric phenomenon, dielectric relaxation (Figure 1-1), where on cooling below room temperature, these materials exhibit a step-like

decrease in the real part of the dielectric permittivity accompanied by a broad frequency-dependent peak in the imaginary part. There are several proposed explanations for the observed relaxation in Bi-pyrochlores,^{12,23,25} however, there is no definite answer as to what induces this dielectric behavior in Bi-pyrochlores. To address this issue an in depth investigation into cubic pyrochlores is needed in order to achieve a fundamental understanding of the necessary conditions to display dielectric relaxation in pyrochlores.

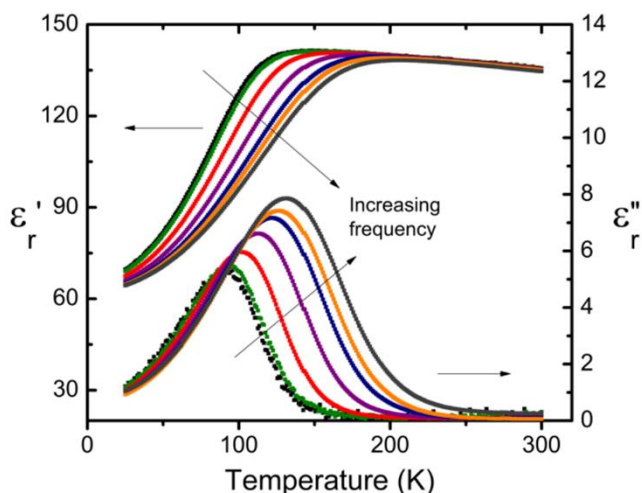


Figure 1-1. Dielectric relaxation in $\text{Bi}_{1.5}\text{Zn}_{0.92}\text{Nb}_{1.5}\text{O}_{6.92}$ pyrochlore.

In addition, other compounds with anion-deficient fluorite-related ($A_2B_2O_7$) structures, such as weberites, were investigated to help elucidate the dielectric response of fluorite related superstructures.

1.2 Scientific Approach

With the aim of identifying the conditions necessary for pyrochlores to exhibit dielectric relaxation, key pyrochlores were selected, synthesized, and characterized. The achievement of synthesizing and sintering phase pure $\text{Bi}_2\text{Ti}_2\text{O}_7$ ²⁶ has opened the door for in-depth studies into the dielectric properties, structure, and even provide insight into the dielectric relaxation phenomena in bismuth-based pyrochlores.

In an effort to investigate the role of atomic displacements on pyrochlore dielectric relaxation, an in-depth structural study was performed using both neutron and high resolution x-ray diffraction on $\text{Bi}_2\text{Ti}_2\text{O}_7$. Both the high resolution x-ray diffraction, conducted at the Advanced Photon Source (APS) of Argonne National Laboratory (ANL), and neutron diffraction studies, conducted at the Open Pool Australian Lightwater Reactor (OPAL) at the Australian Nuclear Science and Technology Organization (ANSTO), were performed down to cryogenic temperatures (~ 6 K) in order to compare any structural changes with the associated dielectric response in $\text{Bi}_2\text{Ti}_2\text{O}_7$. The presence of atomic displacements in Sm-pyrochlores was also probed through x-ray diffraction.

The second step of this research was to provide an in-depth dielectric characterization of fully sintered phase pure $\text{Bi}_2\text{Ti}_2\text{O}_7$ and other Sm-pyrochlores. The dielectric properties of $\text{Bi}_2\text{Ti}_2\text{O}_7$ were comprehensively studied as a function of temperature and frequency in order to clarify the presence of relaxation in this material, and in turn, better understand the nature of the dielectric relaxation phenomena observed in Bi-pyrochlores. Along with $\text{Bi}_2\text{Ti}_2\text{O}_7$, other key pyrochlores are also investigated in order to fully understand the conditions required for dielectric relaxation in pyrochlores.

Vibrational spectroscopy can relate the phonon modes with the observed dielectric properties and, perhaps even more importantly for the case of $\text{Bi}_2\text{Ti}_2\text{O}_7$, gain an insight into the nature and characteristics of the local structure of $\text{Bi}_2\text{Ti}_2\text{O}_7$. This will be accomplished by analysis of Raman and IR (infrared) spectra collected at room and cryogenic temperatures.

The next research area aims to understand what conditions are necessary to be present in pyrochlores for dielectric relaxation. In order to accomplish this goal several newly synthesized pyrochlores, including $\text{Bi}_2\text{Ti}_2\text{O}_7$, and a comprehensive literature review of other Bi-pyrochlores will be presented, experimentally determining what factors are necessary to be present in pyrochlores in order to exhibit dielectric relaxation.

An investigation into the structure-property relationship of a fluorite-related compound, Bi_3NbO_7 , will be presented and will link its dielectric response to its unique structure using Bond Valence Sum (BVS) analysis.

Finally, of Gd_3NbO_7 structure will be discussed by comparing the dielectric response of Gd_3NbO_7 with Gd_3TaO_7 and linking their response with complimentary structure data (HR-XRD, IR).

These results not only contribute to the identification of structure-dielectric property relationships in fluorite related super structures, but also provides a definitive answer for the necessary conditions for dielectric relaxation in pyrochlores.

1.3 Organization of Dissertation

Chapter 2 provides background information necessary for a better understanding of the work presented in subsequent chapters. Information regarding fluorite related superstructures, polarization mechanisms, vibrational spectroscopy, bond valence sum model, and impedance and dielectric spectroscopy is provided.

Chapter 3 discusses the experimental procedures, including sample preparation and materials characterization techniques, used in the execution of the research.

Chapter 4 reports the crystallographic study performed on $\text{Bi}_2\text{Ti}_2\text{O}_7$, $(\text{Sm}_x\text{Yb}_{1-x})_2\text{Ti}_2\text{O}_7$, and $\text{Sm}_2(\text{Sn}_x\text{Ti}_{1-x})_2\text{O}_7$ (where $x = 0, 0.25, 0.5, 0.75, \text{ and } 1$ for all compounds).

Both neutron and synchrotron x-ray diffraction results are presented at varying temperatures (6 K – 400 K) for $\text{Bi}_2\text{Ti}_2\text{O}_7$. Crystallographic refinements of $\text{Bi}_2\text{Ti}_2\text{O}_7$ are also presented at room and cryogenic temperatures. The Sm-pyrochlores are also examined in order to discern the presence of displacements from the ideal pyrochlore structure, one of the possible factors contributing to dielectric relaxation.

Chapter 5 reports the dielectric properties for $\text{Bi}_2\text{Ti}_2\text{O}_7$, and the Sm-pyrochlores investigated in Chapter 4. An in depth study of the dielectric properties of $\text{Bi}_2\text{Ti}_2\text{O}_7$ were measured as a function of frequency (40 Hz – 2MHz) and temperature (20 K – 500 K). The dielectric response of other key pyrochlores were investigated to probe for the presence of dielectric relaxation.

Chapter 6 includes the analysis of Raman and infrared (IR) spectroscopy studies in $\text{Bi}_2\text{Ti}_2\text{O}_7$. A detailed analysis linking non-correlated atomic displacements to the Raman and IR spectra is presented. The nuclear site group analysis is used to ascribe the possible modes in both the IR and Raman spectra. Oscillator models are utilized to fit the spectrum and calculate the real and imaginary contributions of the permittivity.

Chapter 7 presents a summary of the dielectric response of pyrochlores previously studied along with that of the pyrochlores selected in this study to help elucidate the nature of dielectric relaxation. This Chapter presents what factors are required to be present in any pyrochlore in order to display the dielectric relaxation phenomena.

Chapter 8 covers correlations between dielectric properties and crystal structure of Bi_3NbO_7 . A detailed dielectric analysis as a function of frequency and temperature shows the transition from an insulating behavior to conduction. A comparison between

the structure of Bi_3NbO_7 and other Ln_3NbO_7 defect fluorites is performed using Bond Valence Sum (BVS) analysis and then compared to their dielectric responses.

Chapter 9 presents the structure of Gd_3NbO_7 in a new light by comparing its dielectric response to that of Gd_3TaO_7 . By using this dielectric comparison and other complimentary structural data, the low-temperature phase of Gd_3NbO_7 is presented.

Chapter 10 presents a summary of the dissertation and discusses the future work in the relevant research areas.

At the end of the thesis, there is an appendix section, appendix A on fitting the relaxation behavior of $\text{Bi}_2\text{Ti}_2\text{O}_7$ to an equivalent circuit.

1.4 Contributions to the Field

The structure and atomic positions of $\text{Bi}_2\text{Ti}_2\text{O}_7$ was reported for the first time using neutron diffraction and synchrotron x-ray diffraction. Atomic displacements in the A-site and O' are present without chemical substitution. An in depth study focusing on neutron HR-XRD and DFT simulations is in preparation for publication.²⁷

A thorough electrical characterization of $\text{Bi}_2\text{Ti}_2\text{O}_7$ was performed thorough electrical characterization (first time bulk values have been characterized). $\text{Bi}_2\text{Ti}_2\text{O}_7$ displays space charge relaxation near room temperatures at low frequency range. This work was also published in the Journal of the American Ceramics Society²⁸

$\text{Bi}_2\text{Ti}_2\text{O}_7$ does not display typical dipolar Bi-pyrochlore relaxation behavior and most importantly, that chemical substitution is a necessary condition for dielectric relaxation in bismuth based pyrochlores.

A Raman and infrared characterization of $\text{Bi}_2\text{Ti}_2\text{O}_7$ was characterized for the first time in the field. Evidence of Bi cation displacements was found by the overlap of infrared F_{1u} modes in the Raman spectra. Evidence of the displacement upon the Ti

cation as observed by analysis of phonon mode interactions. This work has been submitted to the Physical Review B journal.²⁹

By investigating the dielectric response of the $\text{Bi}_2\text{Ti}_2\text{O}_7$, $(\text{Sm}_x\text{Yb}_{1-x})_2\text{Ti}_2\text{O}_7$, and $\text{Sm}_2(\text{Sn}_x\text{Ti}_{1-x})_2\text{O}_7$ pyrochlore systems the impact of cation substitutions and atomic displacements on relaxation was targeted. The absence of dielectric relaxation in these systems prove that in order to display dielectric relaxation in pyrochlores it is necessary to have both atomic displacements and cation substitutions

The dielectric properties of Type-II Bi_3NbO_7 single crystal were studied for the first time. The real part of permittivity increases with an increase in Ln^{3+} ionic radius and an increased divergence from the Clausius-Mossotti Equation is observed when applied to the type-II Bi_3NbO_7 with large dipolar contributions. This work was submitted for publication in the Journal of Solid State Chemistry.³⁰

The author has also synthesized and characterized dielectric tests on Gd_3TaO_7 and the structural transition of Gd_3NbO_7 is $Cm2m$ at low temperatures.³¹ Along with the main works presented in this dissertation the author has been involved in the dielectric characterization of BaTiO_3 and BiNb_3O_9 which have been published in the Journal of Applied Physics³² and the Journal of Solid State Chemistry³³, respectively.

CHAPTER 2 BACKGROUND

The present Chapter briefly summarizes some of the theoretical background required for understanding the work covered in this dissertation.

2.1 Fluorite Related Superstructures

The fluorite structure serves as the building blocks for fluorite superstructures such as pyrochlores, weberites and defect fluorites. These superstructures are best described in relation to the fluorite crystal structure. In the cubic fluorite structure (MX_2), M^{2+} cations are located at the face centered sites and the X^{-1} anions are located at the tetrahedral sites as shown in Figure 2-1 for CaF_2 .

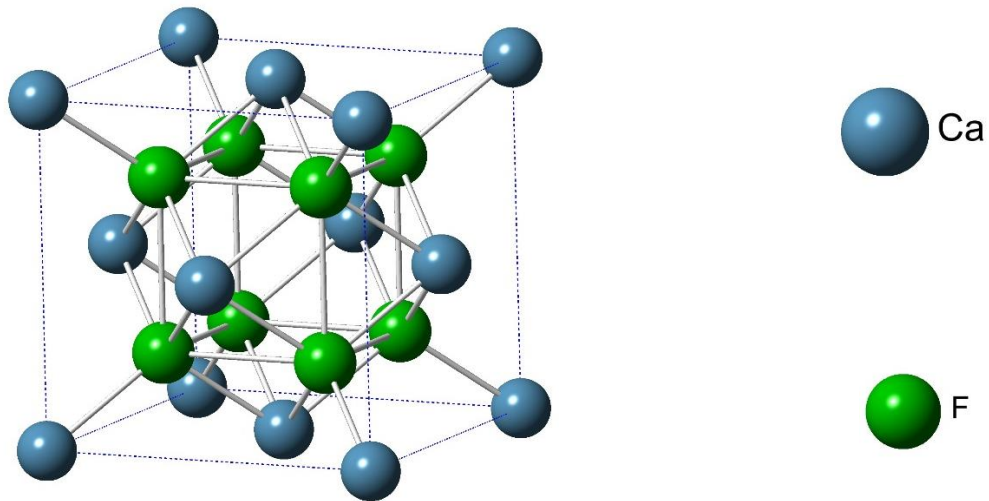


Figure 2-1. The fluorite structure of CaF_2 .

2.1.1 The pyrochlore structure

The oxide pyrochlore structure is presented as $A_2B_2O_6O'$ to represent the four distinct crystallographic atomic sites, where the A cations are typically +3 and the B cations are of +4 charge. Pyrochlores are assigned the space group $Fd\bar{3}m$ (space group 227) containing eight molecules per unit cell ($Z = 8$). The A cation ($\sim 1 \text{ \AA}$ ionic radius) and surrounding oxygen form an eight-fold coordinated distorted cube (scalenoedra),

composed of six equidistant anion atoms (O) and two anions (O') at a shorter distance. The B cations are typically smaller (~ 0.6 Å ionic radius) and are six-fold coordinated with O atoms, all at equal distances from the center B atom, to form trigonal antiprisms. The coordination states of the cations are often referred to as octahedral (A cation) and cubic (B cation).³⁴

If the A cation is located at the origin of the pyrochlore it is said to be origin choice 1, for a B cation at the origin it is origin choice 2. Typically, and for the purposes of this thesis all pyrochlores will be discussed based on origin choice 2, unless otherwise specified. The location of the atoms, site symmetry and atomic coordinates are given in Table 2-1.

Table 2-1. Pyrochlore (A₂B₂O₆O') structure (origin choice 2)³⁴

Atoms	Wyckoff Position	Site Symmetry	Atomic Position		
			x	y	z
A	16 <i>d</i>	$\bar{3}m$ (D _{3d})	0.5	0.5	0.5
B	16 <i>c</i>	$\bar{3}m$ (D _{3d})	0	0	0
O	48 <i>f</i>	mm (C _{2v})	<i>x</i>	1/8	1/8
O'	8 <i>b</i>	$\bar{4}3m$ (T _d)	3/8	3/8	3/8

Description of the Pyrochlore Structure. There are many different ways to describe the pyrochlore structure. One method is to base the pyrochlore structure off of the fluorite structure. Incorporating A³⁺ and B⁴⁺ cations to face centered sites of the fluorite structure will lead to an anion deficient fluorite unit cell (Figure 2-2B). One pyrochlore unit cell edge length is twice that of a unit cell of CaF₂, therefore allowing eight unit cells of the anion deficient fluorite structure to fit inside the pyrochlore unit cell (Figure 2-2C).

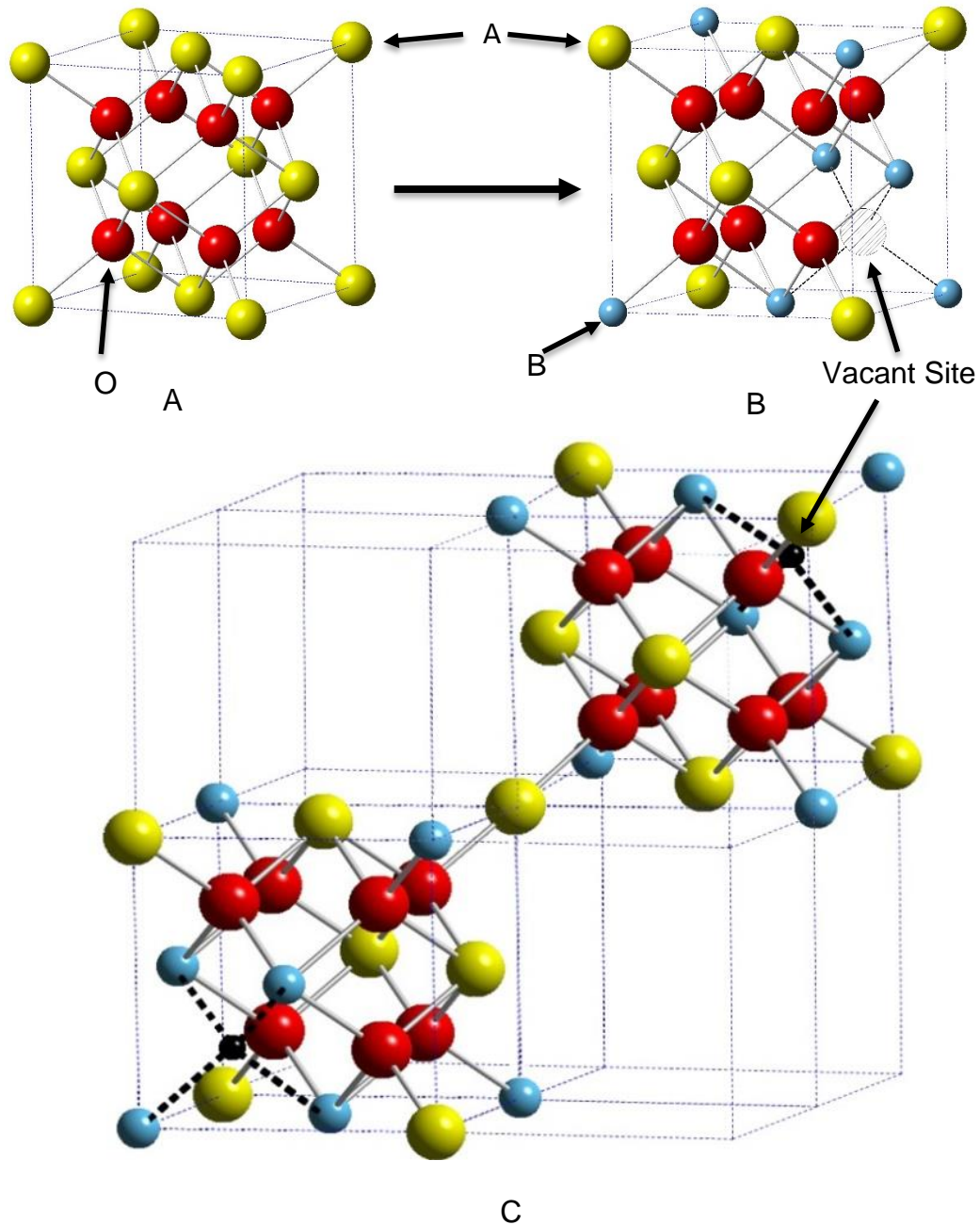


Figure 2-2. The pyrochlore structure visualization. A) the fluorite structure, B) an anion deficient fluorite, C) two of the eight anion deficient structures arranged in the pyrochlore unit cell.

The pyrochlore structure can also be described as two interpenetrating networks (Figure 2-3). The BO_6 octahedra form a corner shared octahedral network, while A_2O' tetrahedral substructures are found in the empty channels formed by the BO_6 octahedra.

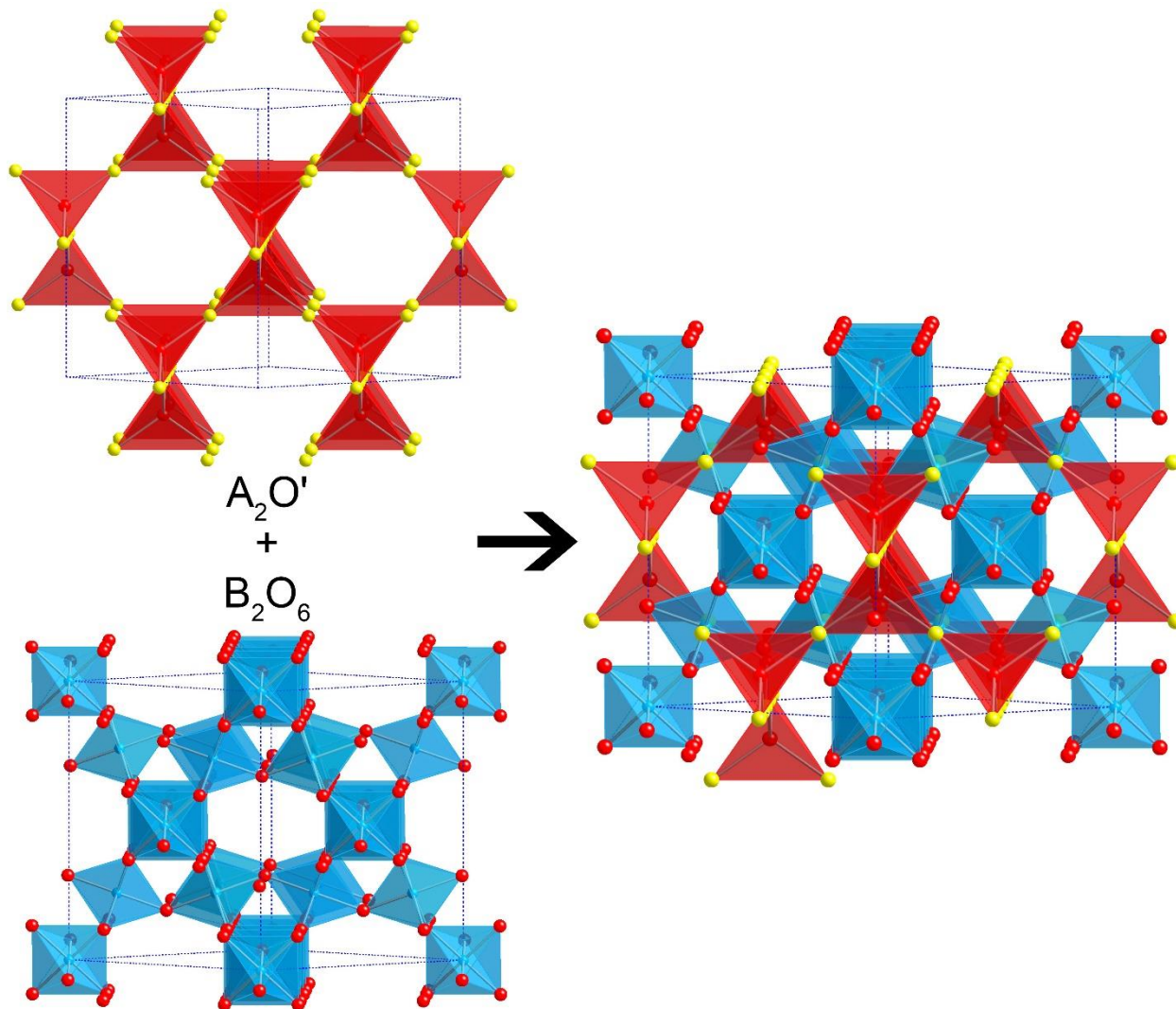


Figure 2-3. The A_2O' tetrahedral and B_2O_6 octahedral networks that make up the pyrochlore structure.

For an ideal pyrochlore, using origin choice 2, six of the seven oxygen ions is located at Wyckoff position $48f (x, 1/8, 1/8)$. The x parameter can vary from 0.3125, leading to perfect BO_6 octahedra and distorted AO_8 cubes, to an x of 0.375, leading to distorted BO_6 octahedra and regular AO_8 cubes (Figure 2-4).

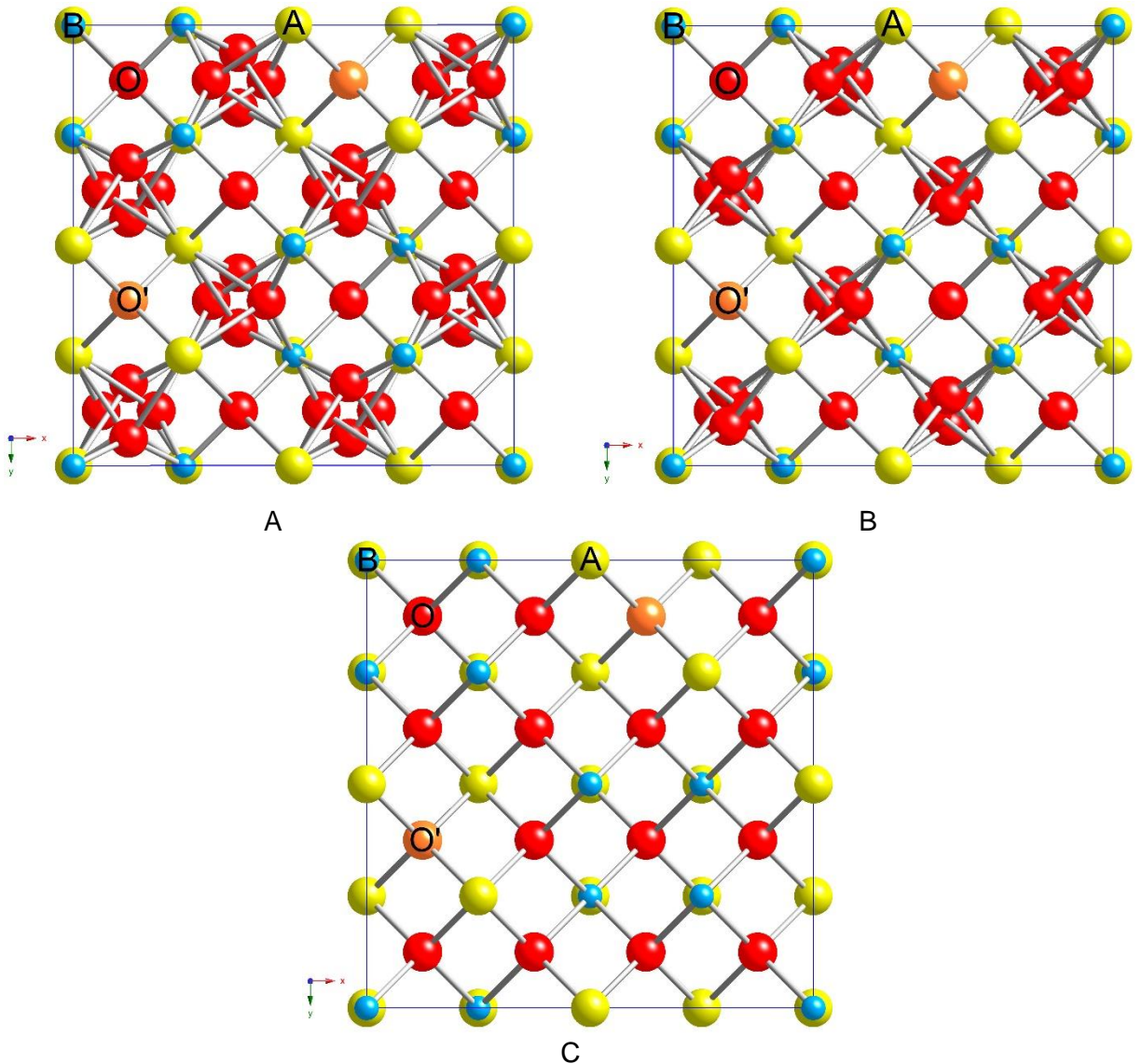


Figure 2-4. [001] view of pyrochlores. A) When $x = 0.3125$ (perfect BO_6 octahedra) B) x is between 0.3125 and 0.375 (both BO_6 octahedra and AO_8 cubes are distorted) C) $x = 0.375$ (perfect AO_8 cubes)

2.1.2 The defect-fluorite structure

The crystal structure of Ln_3NbO_7 , where Ln = a lanthanide series cation with a +3 charge, has been shown to shift from an orthorhombic weberite-type structure to a cubic defect fluorite with decreasing Ln^{3+} ionic radius.³⁵⁻³⁷

Cubic defect-fluorite structures occur in Ln_3NbO_7 when the ionic radius of the Ln^{3+} cation is less than or equal to that of Dy^{3+} (1.027 Å).³⁶ The defect fluorite structure has both disordered cations as well as disordered oxygen deficiency sites, unlike the pyrochlore in which the A , B cations, and the oxygen vacancy sites have an ordered arrangement.³⁸ Visually it can be regarded as a disordered anion deficient fluorite similar to what is shown in Figure 2-2B.

2.2 The Bond Valence Model

The bond valence sum (BVS) model³⁹⁻⁴¹ is a common technique used for analyzing coordination and bonding in solid state chemistry. A bond valence is assigned to each bond in a structure based on the bond distance and types of ions involved in the bond. The bond valence (S_{ij}) for all atoms is calculated as:

$$S_{ij} = \exp\left(\frac{R_o - R_{ij}}{b}\right) \quad (2-1)$$

where R_{ij} is the length of the bond between atoms i and j , R_o is the standard bond distance between atoms i and j , and b is an empirically derived constant, normally found close to 0.37.³⁹

The bond valence sum (BVS) for an ion is equal to the sum of all of the surrounding bond valences of the ion, with positive values for cations and negative values for anions:

$$|BVS_i| = \sum_j S_{ij} \quad (2-2)$$

A lower absolute value of BVS_i indicates that the ion is under-coordinated, while higher values indicate an over-coordination.

Lattice-induced strains can be identified by a large value of the bond strain index (BSI) defined as:

$$BSI = \langle (S-s)^2 \rangle^{1/2} \quad (2-3)$$

where S is the experimental bond valence calculated from the observed bond length and s is the theoretical bond valence. The angle brackets indicate an average taken over all bonds in the formula unit. A structure is typically considered strained when the BSI is greater than 0.05 valence units (vu).³⁹

A second and complimentary measure of lattice strain is the global instability index (GII), the root mean square of the deviation of the BVSs from their expected values for all the atoms in the unit cell, shown in Equation 2-4:

$$GII = \sqrt{\frac{\sum (BVS - BVS_o)^2}{N}} \quad (2-4)$$

where N is the number of atoms in the unit cell and BVS_o is the expected bond valence sum. Values of GII less than 0.05 vu suggest that little or no strain is present while values greater than 0.2 vu indicate that the structure is very strained.³⁹

2.3 Polarization Mechanisms

When a dielectric material is exposed to an electromagnetic field, the electric field will cause a displacement of negative and positive charges. This polarization of charge can happen through the displacement of charge in individual atoms or molecules, the orientation of existing dipoles toward the direction of the field, or the separation of mobile charge carriers at the interfaces of impurities or other defect boundaries.⁴² The polarization (P) can be determined by the dipole moments (μ):

$$P = N\mu = Nq\delta \quad (2-5)$$

where N is the number of dipoles per unit volume, q is the charge, and δ is the distance between the charges. One can relate the dielectric permittivity (ϵ_r') with polarization:

$$\epsilon_r' - 1 = \frac{P}{\epsilon_0 E_{loc}} \quad (2-6)$$

where ϵ_0 is the permittivity of free space, and E_{loc} is the local electric field to which the atom is subjected to. Equation 2-6 basically shows that the more polarizable a medium the greater its dielectric permittivity.

The polarizability (α) of an atom or ion is defined as:

$$\alpha = \frac{P}{NE_{loc}} \quad (2-7)$$

The microscopic polarization phenomena (α) can be linked to the macroscopic term ϵ_r' by using the Clausius-Mossotti Equation:

$$\epsilon_r' - 1 = \frac{N\alpha/\epsilon_0}{1 - N\alpha/3\epsilon_0} \quad (2-8)$$

There are four main types of polarization mechanisms (when only considering linear dielectric materials):

1. Electronic polarization
2. Ionic polarization
3. Dipolar polarization
4. Space charge or interfacial polarization

Each type of polarization (Figure 2-5) is present at different time domains; which is why the degree of the overall polarization depends on the time variation of the electric field.

2.3.1 Electronic polarization

Electronic polarization occurs when the electron cloud is displaced relative to its nucleus and its surroundings. It is active at most frequencies up to $\sim 10^{15}$ Hz, where it no longer responds to the electric field.

Polarization Mechanisms

Unpolarized State

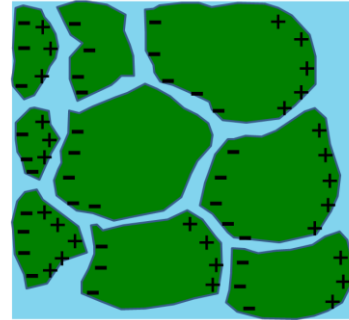
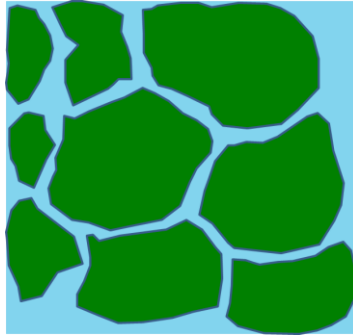
No Electric Field

Polarized State

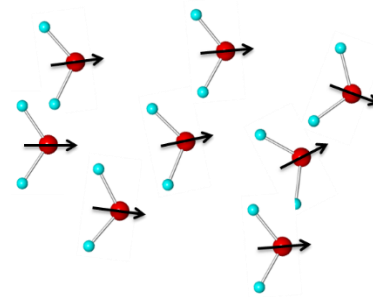
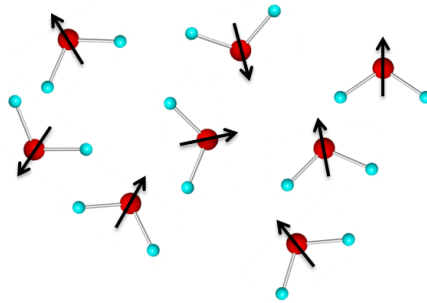
Electric Field



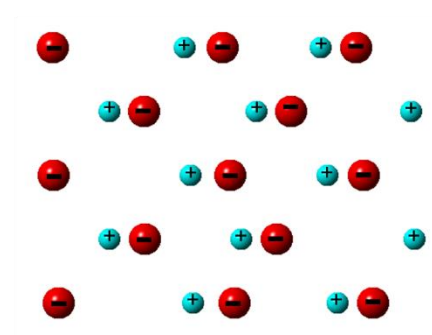
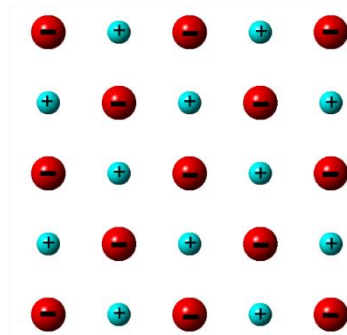
Space Charge



Dipolar



Ionic



Atomic

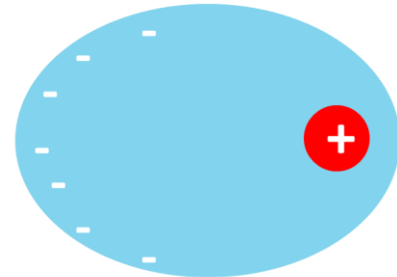
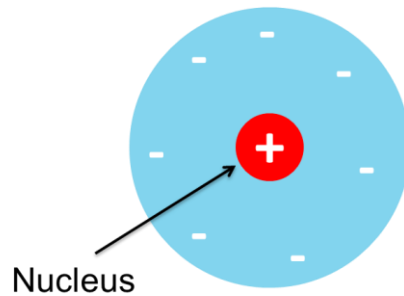


Figure 2-5. The four main polarization mechanisms. (Diagram from Moulson and Herbert⁴³)

Electronic polarization occurs in all materials and because it does not involve the hopping of ions or atoms it is temperature-insensitive. The contribution of electronic polarization to the real and imaginary components of the permittivity (assuming $E_{loc} = E_{ext}$) are:

$$\epsilon'_e(\omega) = 1 + \frac{Ze^2N(\omega_0^2 - \omega^2)}{\epsilon_0 m_e [(\omega_0^2 - \omega^2)^2 + \zeta^2 \omega^2]} \quad (2-9)$$

$$\epsilon''_e(\omega) = \frac{Ze^2N\omega\zeta}{\epsilon_0 m_e [(\omega_0^2 - \omega^2)^2 + \zeta^2 \omega^2]} \quad (2-10)$$

where Z is the atomic number, m_e is the mass of an electron, ω_0 is the natural frequency of vibration (resonant frequency), ω is the operating frequency, ϵ_0 is the permittivity of free space and ζ is a damping constant.

2.3.2 Ionic polarization

Under an electric field the positive and negative ions will displace according to the direction of the field. The contribution of ionic polarization is active up until the infrared frequency range ($\sim 10^{12} - 10^{13}$ Hz). The contribution to the real and imaginary components of the permittivity for ionic polarization are very similar to those shown in Equations 2-11 and 2-12:

$$\epsilon'_{ion}(\omega) = 1 + \frac{(Ze)^2 N_{ion} (\omega_{ion}^2 - \omega^2)}{\epsilon_0 M_r [(\omega_{ion}^2 - \omega^2)^2 + \zeta_{ion}^2 \omega^2]} \quad (2-11)$$

$$\epsilon''_{ion}(\omega) = 1 + \frac{(Ze)^2 N_{ion} \omega \zeta_{ion}}{\epsilon_0 M_r [(\omega_{ion}^2 - \omega^2)^2 + \zeta_{ion}^2 \omega^2]} \quad (2-12)$$

where N_{ion} is the number of ion pairs per cubic meter, ω_{ion} is the natural frequency of vibration of the ion pair, M_r is the reduced mass of the system. Similar to electronic

polarization, ionic polarization is temperature independent and stronger bonds with higher ω_{ion} values are less readily polarized.

2.3.3 Dipolar polarization

Unlike electronic and ionic polarization, which occur at very high frequencies ($\omega > 10^{12}$ Hz), dipolar relaxation occurs at lower frequencies ($10^4 < \omega < 10^{10}$ Hz) and plays an important role in determining the capacitive properties of materials to be used in low-frequency applications.

Dipolar polarization arises from the reorientation and alignment of permanent dipoles due to an external field. In solids, ions preferentially occupy equivalent or near equivalent lattice sites as a result of the applied field, shown schematically in Figure 2-6. An ion is localized in an energy well in one of the two equivalent sites (Figure 2-6A). These sites are separated by an energy barrier of ΔH_m and by a distance λ_s . Without the presence of an electric field (Figure 2-6A), each site has an equal probability of being occupied and there is no net polarization. When an electric field is applied (Figure 2-6 B) the two sites are no longer equivalent, resulting in a bias towards one of the sites and creating a net polarization, this phenomenon is called ion jump polarization.⁴³

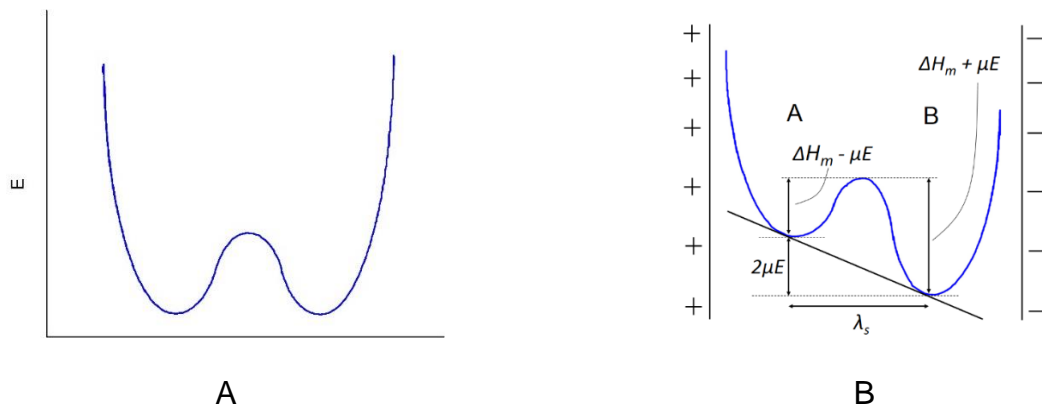


Figure 2-6. Dipolar polarization energy schematic. A) energy versus distance diagram under no applied field. B) under an applied field a bias occurs to one site relative to the other. (Diagram adapted from Moulson and Herbert⁴³)

The dipolar mechanism contributions to the permittivity, under static conditions, are given by:

$$\epsilon'_{dip} = \frac{(Ze)^2 N_{dip} \lambda_s^2}{4kT\epsilon_0} \quad (2-13)$$

where N_{dip} is the number of dipoles per cubic meter, λ_s is the separation distance of the two equivalent sites (Figure 2-5), k is Boltzmann's constant, and T is temperature (K). It is important to note that Equation 2-9 applies to the dipolar contributions under static (d.c.) conditions, also increasing the temperature will reduce the permittivity contributed by dipolar polarization due to thermal randomization.

In order to understand the behavior of dipolar polarization under dynamic (a.c.) conditions a mathematical model was created by Debye⁴⁴ to describe the properties of polar molecules and gases. Unlike ionic and electronic polarization, dipolar polarization does not occur instantaneously under the application of an electric field. A slower polarization mechanism occurs due to the dipolar reorientation (P) until it reaches its final static value (P_s). The rate at time t at which P increases is proportional to the difference between the static value and the present value, where $1/\tau$ is the proportionality constant. This is expressed in Equation 2-14:

$$P = P_s \left(1 - \exp \left[-\frac{t}{\tau} \right] \right) \quad (2-14)$$

where τ is the relaxation time of the dipole moment of the molecule. Another important assumption to describe dipolar relaxation under the Debye model is that the relative dielectric constant is given by $\epsilon(\omega) = \epsilon_\infty + f(\omega)$, where ϵ_∞ represents the contributions to the permittivity at frequencies much higher than dipolar (i.e. electronic and ionic

polarization). It is also required that as the frequency tends to zero $\epsilon(\omega) = \epsilon_s$, the static dielectric constant. From these assumptions it can be shown that:

$$\epsilon'(\omega) = \epsilon_\infty + \frac{\epsilon_s - \epsilon_\infty}{1 + \omega^2 \tau^2} \quad (2-15)$$

$$\epsilon''(\omega) = \frac{\omega \tau}{1 + \omega^2 \tau^2} (\epsilon_s - \epsilon_\infty) \quad (2-16)$$

These Equations are known as the Debye Equations and their variation with frequency for a material showing Debye relaxation is shown in Figure 2-7.

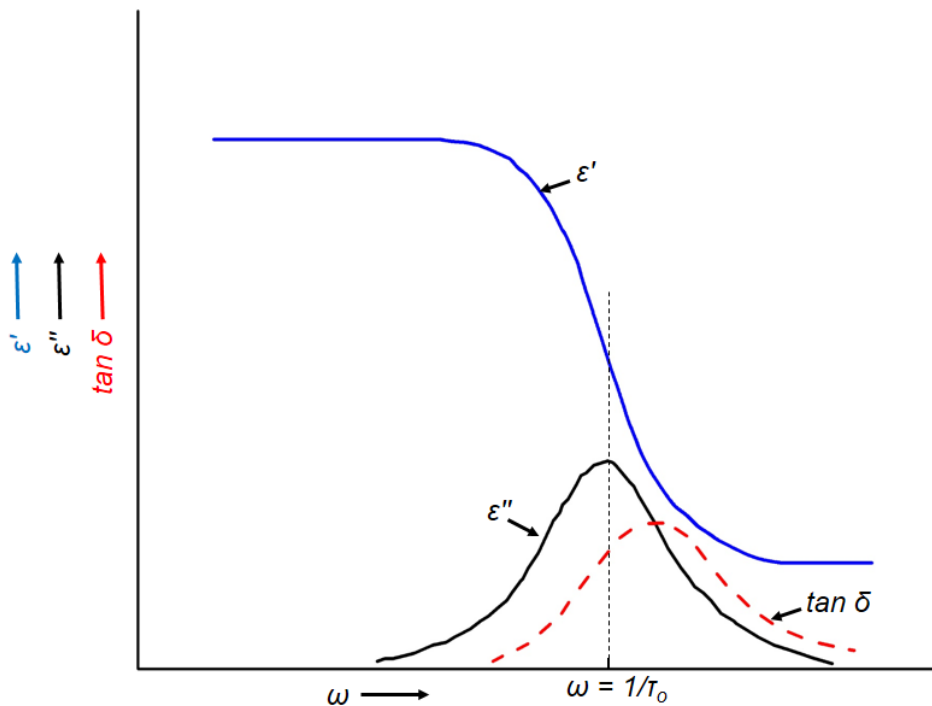


Figure 2-7. Frequency response of a dielectric material for dipolar polarization. (Diagram adapted from Kao⁴²)

The average residence time (τ) (or relaxation time) of an atom or ion at any given site is also temperature-dependent:

$$\tau = \frac{1}{\omega_0} \exp\left(\frac{E_a}{kT}\right) \quad (2-17)$$

where $1/\omega_0$ is the attempt jump frequency and E_a is the activation energy of relaxation, and k is Boltzmann's constant. This shows that as the temperature increases, the atoms vibrate faster and are capable of following the applied field to higher frequencies.⁴³

2.3.4 Space charge polarization

Space charge, or interfacial polarization, is produced by the separation of mobile positively and negatively charged particles under an applied field; space charge relaxation occurs at the lowest frequencies (up to 10^6 Hz). These charges can form in the bulk of the material or at the interface between two different materials. Like dipolar polarization, space charge polarization does not occur instantaneously under an electric field and undergoes a relaxation effect rather than a resonance.

2.3.5 The dielectric spectrum

For most materials there exists more than one active polarization mechanism and the total permittivity is given by $\epsilon_{\text{total}} = \epsilon_{\infty} + \epsilon_{\text{electronic}} + \epsilon_{\text{ionic}} + \epsilon_{\text{dipolar}} + \epsilon_{\text{space-charge}}$. As the frequency increases, various polarization mechanisms will be unable to keep up with the field and will drop off (Figure 2-8). Polarizations associated with vibrations of electrons (i.e. electronic polarization) or with vibrations of atoms (i.e. ionic polarization) belong to the resonance regime because a resonance will occur when the frequency of the applied field is close to the natural frequency of the vibration or oscillation of the system. Polarizations involving the movements of dipoles (i.e. dipolar relaxation) or through the migration of charge carriers (i.e. space charge polarization) belong to the relaxation regime as during their polarization/depolarization process, a relaxation phenomenon occurs.⁴²

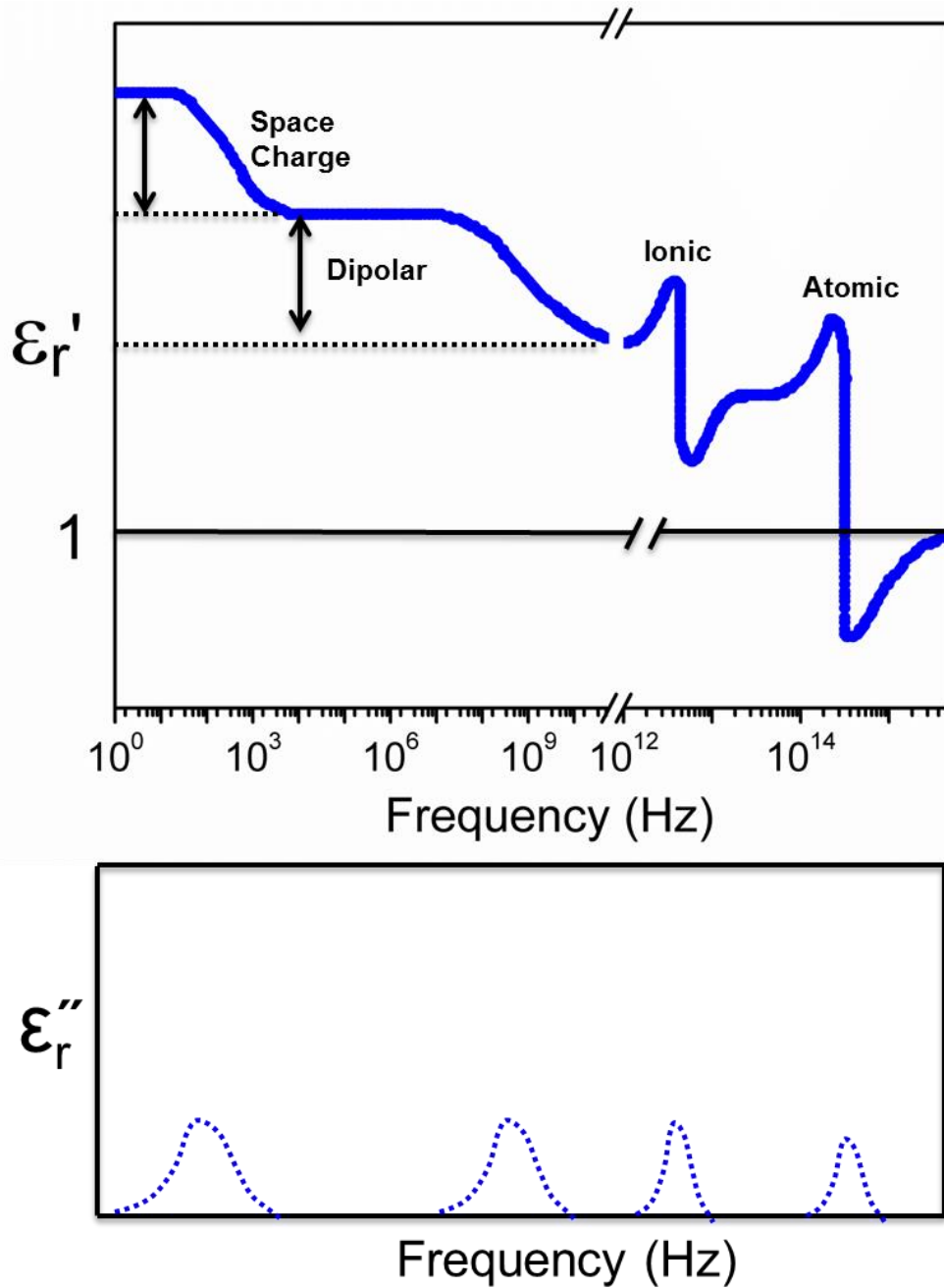


Figure 2-8. Real and imaginary parts of the permittivity as a function of frequency, showing the contribution from the four polarization mechanism. Space charge and dipolar mechanisms are relaxation process while ionic and electronic are resonance processes. (Diagram adapted from Moulson and Herbert⁴³)

2.4 Dielectric Relaxation in Pyrochlores

Bismuth based pyrochlores have been extensively studied due to their attractive composition dependent dielectric properties.^{12,20-24} A combination of high permittivity

values (usually above 100), low dielectric loss, and low sintering temperatures make them good materials for dielectric components. However, all Bi-pyrochlores and several non-Bi pyrochlores display a dielectric phenomenon where: on cooling below room temperature these materials exhibit a step-like decrease in the real part of the dielectric permittivity accompanied by a broad frequency dependent peak in the imaginary part (Figure 2-8). As a consequence of this relaxation, at microwave frequencies the temperature at which the dielectric peaks (T_m) displaces towards room temperature thus limiting GHz frequency applications.^{1,45}

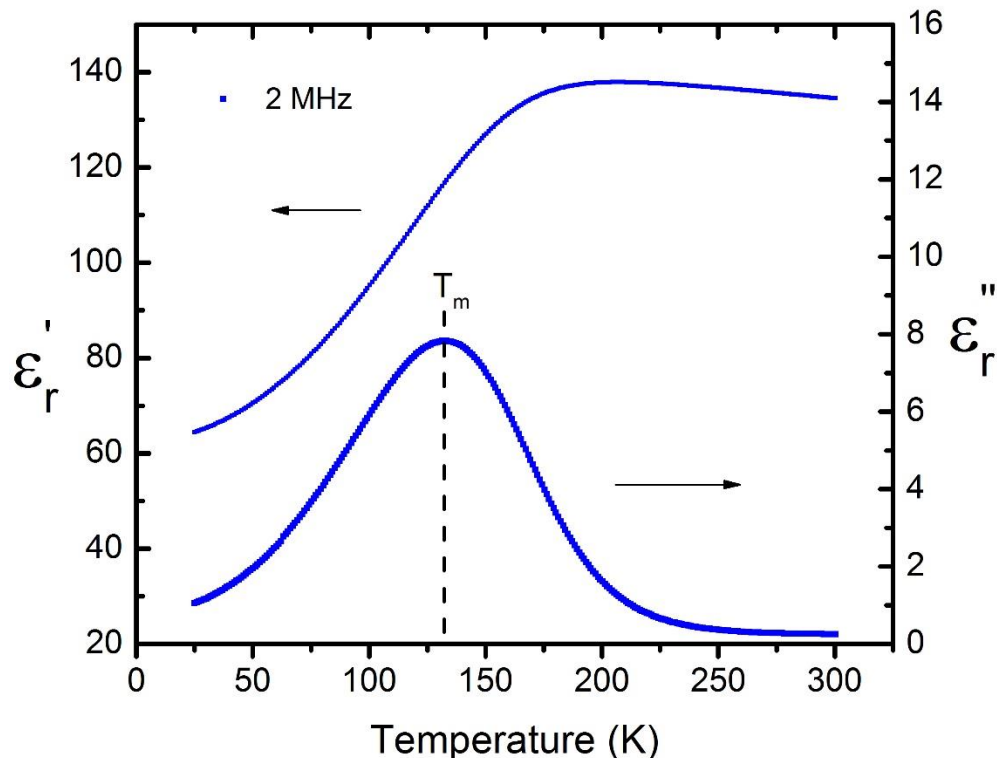


Figure 2-9. Dielectric relaxation for BZN shown at 2MHz vs temperature.

Arrhenius type Equations have been used to describe the dipolar glass systems that display similar relaxations and have been proven to successfully model the thermally activated processes underlying the phenomena.⁴⁶ By employing the Arrhenius Equation, the Debye model corresponding to a single relaxation time can be followed to

fit the data and obtain meaningful physical values for the activation energy (E_a) and attempt jump frequency (ν_0) of the relaxation phenomenon:

$$\nu_r = \nu_0 \exp\left(\frac{-E_a}{k_B T_m}\right) \quad (2-18)$$

where ν_r is the frequency of the relaxation peak in the imaginary part of the permittivity, and k_B is the Boltzmann constant.

All of the pyrochlores that exhibit dielectric relaxation are presented in Table 2-2, a review of these pyrochlores showed three main characteristics that have been proposed to induce relaxation:

1. A polarizable lone-pair cation occupies the A-site
2. There is cation substitution
3. Atomic displacement is present

An in depth discussion into which factors are necessary for dielectric relaxation to occur in pyrochlores is presented in Chapter 6.

Table 2-2. Pyrochlores and the conditions present for possible relaxation

Material	Polarizable Lone Pair A-site	A- and B- site substitution	A-site substitution	B-site substitution	Atomic Displacements	Relaxation
$\text{Bi}_2(\text{ScNb})\text{O}_7$ ²¹	Yes	--	No	Yes	Yes	Yes
$\text{Bi}_2(\text{ScTa})\text{O}_7$ ²¹	Yes	--	No	Yes	Yes	Yes
$(\text{Bi}_{1.5}\text{Zn}_{0.5})(\text{Zn}_{0.5}\text{Nb}_{1.5})\text{O}_7$ ¹³	Yes	Yes	--	--	Yes	Yes
$(\text{Bi}_{1.5}\text{Zn}_{1.5})(\text{Zn}_{0.5}\text{Ta}_{1.5})\text{O}_7$ ²⁵	Yes	Yes	--	--	Yes	Yes
$\text{Bi}_{1.657}\text{Fe}_{1.092}\text{Nb}_{1.150}\text{O}_7$ ²⁴	Yes	Yes	--	--	Yes	Yes
$\text{Bi}_{1.67}\text{Mg}_{0.64}\text{Nb}_{1.53}\text{O}_7$ ⁴⁷	Yes	Yes	--	--	Yes	Yes
$\text{Bi}_{1.68}\text{Ni}_{0.747}\text{Nb}_{1.493}\text{O}_7$ ⁴⁷	Yes	Yes	--	--	Yes	Yes
$\text{Bi}_{1.657}(\text{Fe}_{0.983}\text{Al}_{0.109})\text{Nb}_{1.150}\text{O}_7$ ⁴⁸	Yes	Yes	--	--	Yes	Yes
$\text{Bi}_2(\text{InNb})\text{O}_7$ ²³	Yes	--	No	Yes	Yes	Yes
$(\text{Bi}_{1.93}\text{Fe}_{0.07})(\text{Fe}_{1.42}\text{Te}_{0.58})\text{O}_7$ ⁴⁹	Yes	Yes	--	--	Yes	Yes
$\text{Ca}_{1.46}\text{Ti}_{1.38}\text{Nb}_{1.11}\text{O}_7$ ⁵⁰	No	Yes	--	--	Yes	Yes

The relaxation in Bi-pyrochlores has been ascribed to the random hopping of disordered A and O' ions among equivalent sites.⁴⁵ For most Bi-pyrochlores the A-site cation is usually displaced from its ideal position to the 96g, when this occurs there are 6 equivalent positions where the cation can reside in the structure. The hopping mechanism is shown in Figure 2-9, the Bi cation must overcome an energy barrier before transitioning into the lower energy equivalent 96g site.

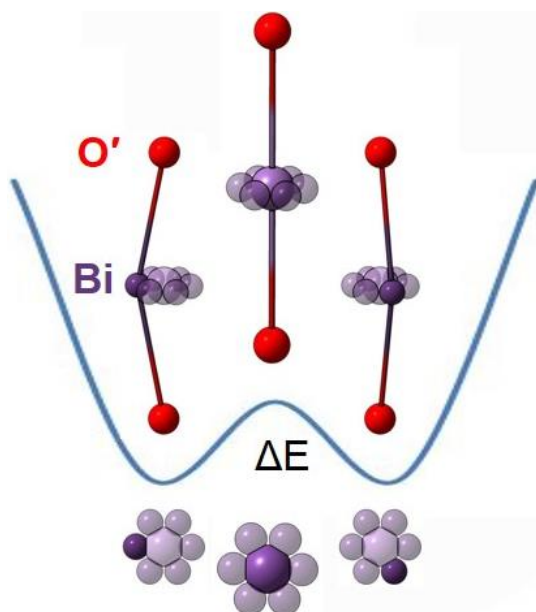


Figure 2-9. A schematic showing a Bi cation pathway hopping between 96g site

2.5 Vibrational Spectroscopy

2.5.1 Normal mode determination

Nuclear site group analysis allows for the determination of the infrared (IR) and Raman active modes in solids without the need of a detailed analysis of the symmetry elements of the unit cell. Using Tables A, B, and E provided by Rousseau *et al.*⁵¹ along with the space group and Wyckoff positions of each atom of the unit cell one has sufficient information to determine the selection rules. Table A provides the site symmetries depending on the space group and Wyckoff positions. Table B specifies the

lattice mode for each symmetry and Table E presents whether the modes are Raman active, IR active, silent, or both Raman and IR active. The irreducible representation (Γ) is calculated by the sum of the Raman and IR active modes minus the acoustic modes.

2.5.2 Raman scattering

Raman spectroscopy involves the inelastic scattering of light by a molecule/material. An electric field is generated by an intense light beam that polarizes the electron clouds that make up chemical bonds. By reversing the field the energy stored in the distorted electron cloud is released, and creates a spontaneous emission of photons. The re-emitted light is usually of the same frequency as the incident light (Rayleigh scattering), however a small amount of the energy (1 in 10^6 photons) is transferred to the material and sets it into vibration. This results in the emission of light with a frequency shifted lower than the incident light by an amount equal to the vibrational frequency of the target material. In order for a material to be Raman active, the vibration of the crystal must be accompanied with a change in the polarizability of the molecule.⁵²

2.5.3 Infrared absorption

There are two important conditions that are critical to the infrared (IR) absorption process: these are the radiation frequency and the molecular dipole moment. Resonance between the radiation and material occurs when the specific oscillating radiation frequency matches the natural frequency of a particular normal mode of vibration. However in order for energy to be transferred from the IR photon to the material via absorption the dipole moment of the molecule must change due to this vibration.⁵³

Raman and Infrared spectroscopy are complementary techniques and although some vibrations may be active in both Raman and IR, these two forms of spectroscopy arise from different processes and different selection rules.

CHAPTER 3 EXPERIMENTAL PROCEDURES AND PROCESSING

3.1 Bi₂Ti₂O₇ Synthesis

3.1.1 Powder synthesis

To prepare 0.01 mol of Bi₂Ti₂O₇, nitric acid (Ricca Chemical Company, 35% v/v), bismuth subnitrate (Fisher USP, 0.05/5 mol), ammonium hydroxide (Acros Organics, 28-30% solution of NH₃ in water), and titanium (IV) isopropoxide (Acros Organics, 98+%) were used as starting materials. Bismuth subnitrate (0.02 mol) was dissolved in nitric acid (40mL) after approximately 20 min of stirring. The ammonium hydroxide (40 mL) was kept in a freezer below 0°C, while the bismuth nitrate was dissolved. Titanium isopropoxide (0.02 mol plus a 23% excess⁵⁴) was added to the bismuth nitrate solution followed by 5 min of stirring. The ammonium hydroxide was then poured into this mixture and after vigorous stirring a white precipitate was formed. The precipitate was filtered, rinsed with abundant DI water, and dried overnight. After the drying process off yellow powder aggregates were ground with a mortar and pestle until a homogenous white fine powder was observed.

A calcination step was carried out at 550°C for 16 h with a heating and cooling rate of 200°C/h in a zirconium oxide crucible.

3.1.2 Pellet formation

After the powder was calcined the powder was mortar and pestle and sieved through a 212 μm mesh sieve. The powders were uniaxially pressed at 150 MPa into cylindrical pellets with a diameter of 13mm, 7mm, or 3mm with a thickness of approximately 1 mm. The samples were then isostatically pressed at 250 MPa to further increase the density of the green body. The pellets were microwaved sintered in a

ThermWAVE 1.3 furnace using silicon nitride susceptors to attain a heating rate of 80°C/min and a holding temperature of 1200°C for 45 min. The samples were ambient cooled to room temperature inside the microwave furnace.

For dielectric measurements the sintered pellets were polished to a 1200 grit (SiC) finish, sonicated in water for 10 min and then electroded with gold (sputter coated) and silver paste. They were then dried overnight at 120°C.

For IR measurements the circular pellet was polished to form a 'wedge' circular pellet, where one edge was ~ 1 mm in thickness which tapered to a point on the other end of the pellet (~ 0.1 mm thickness). The slanted face of the pellet was then polished to 0.05 µm alumina slurry to obtain a mirror finish.

3.2 Solid State Synthesis

3.2.1 Powder synthesis

All other polycrystalline pyrochlores and Ln_3NbO_7 were prepared by solid state processing. The starting materials were Dy_2O_3 (Alfa, 99.99%), Yb_2O_3 (Alfa, 99.9%) Sm_2O_3 , Sn_2O_3 , Nb_2O_5 (Alfa, 99.9985%), Gd_2O_3 (Alfa, 99.99%), TiO_2 and Ta_2O_5 (Alfa, 99.99%). The powders were mixed in their desired molar ratios and were mixed with 70 ml of deionized water and 2 ml of ammonium polyacrylate dispersant (Darvan 821 A). The milling media contained 60 g of yttria stabilized zirconia spheres with diameters of 10mm and 3 mm, respectively. The slurry was ball-milled for 24 hours at 85 rpm. The slurry was then poured onto a Teflon sheet, covered with aluminum foil, and subsequently dried in the oven at 120°C for 16 hours followed by grinding with a corundum mortar and sieving through a 212 µm mesh. The powders were then placed in an alumina crucible and calcined in air with a 200°C/h heating and cooling rate. The

calcination temperatures and times for the synthesized compositions are presented in Table 3-1.

3.2.2 Pellet formation

After the phase pure phase was formed, 1wt%-3wt% of PVA binder (Celvol 103) was added to assist in pellet formation. The binder contained 20vol% PVA and 80vol% deionized water. The binder and the powders were mixed with mortar and pestle and sieved through a 212 μm mesh. The mixed powders were then dried in the oven at 120°C for 5 min to evaporate water. The powders were then uniaxially pressed at 150 MPa into cylindrical pellets with a diameter of 13 mm or 7 mm and a thickness of approximately 1 mm. The pellets were then isostatically pressed at 250 MPa, they were then sintered in a conventional furnace with a heating and cooling rate of 200°C. The sintering temperatures and times for the synthesized compositions are shown in Table 3-1.

Table 3-1. The calcination and sintering times and temperatures for the solid state synthesized oxides.

Compound	Calcination Temperature	Calcination Time	Sintering Temperature	Sintering Time
Gd_3TaO_7	1400°C	8 h	1650°C	6 h
Gd_3NbO_7	1400°C	4 h	1600°C	4 h
$\text{Sm}_2\text{Ti}_2\text{O}_7$	1250°C	9h	1300°C	2h
$\text{Yb}_2\text{Ti}_2\text{O}_7$	1250°C	8h	1250°C	10h
$(\text{Sm}_{0.75}\text{Yb}_{0.25})_2\text{Ti}_2\text{O}_7$	1250°C	8h	1250°C	10h
$(\text{Sm}_{0.50}\text{Yb}_{0.50})_2\text{Ti}_2\text{O}_7$	1250°C	8h	1250°C	10h
$(\text{Sm}_{0.25}\text{Yb}_{0.75})_2\text{Ti}_2\text{O}_7$	1250°C	8h	1250°C	10h
$\text{Dy}_2\text{Ti}_2\text{O}_7$	1250°C	10h	1300°C	3h
$(\text{Sm}_{0.50}\text{Dy}_{0.50})_2\text{Ti}_2\text{O}_7$	1250°C	10h	1300°C	2h
$\text{Sm}_2\text{Sn}_2\text{O}_7$	1100°C	8h	1150°C	2h
$\text{Sm}_2(\text{Sn}_{0.5}\text{Ti}_{0.5})_2\text{O}_7$	1150°C	6h	1200°C	8h

3.3 Characterization

3.3.1 Structural characterization

Philips APD 3720 and PANalytical X'Pert Powder diffractometers were used for structural characterization. The XRD was conducted using $\text{CuK}\alpha$ radiation with operational conditions of 40kV and 20mA for the APD and 40kV and 40mA for the X'pert. After every calcination process, XRD was used to check the phase purity after the calcined powders were ground by mortar and pestle. After the pellets were sintered, XRD was used again to check the phase purity and to ensure no secondary phases were present in the sintered samples.

In addition to the above, high resolution synchrotron powder diffraction data were collected for $\text{Bi}_2\text{Ti}_2\text{O}_7$ using the diffractometer at 11-BM at the Advanced Photon Source (APS),⁵⁵ Argonne National Laboratory using an average wavelength of 0.413 Å. Discrete detectors covering an angular range from -6 to $16^\circ 2\theta$ are scanned over a $44^\circ 2\theta$ range, with data points collected every $0.002^\circ 2\theta$ and scan speed of $0.15^\circ/\text{s}$. The temperature was controlled by an Oxford closed helium cryostat from 5 K to 298 K, the temperatures between 300 K and 400 K were controlled by an Oxford cryostream 700+ N_2 gas blower. The powdered sample was mixed with 'GE' Varnish to increase the thermal transport between the small diameter kapton capillary and the helium exchange gas. The kapton capillaries were rotated normal to the beam direction all the time during the X-ray exposure to avoid sample preferred orientation.

Neutron diffraction for $\text{Bi}_2\text{Ti}_2\text{O}_7$ was measured by Professor Brendan J. Kennedy at the University of Sydney. Approximately 7 g of $\text{Bi}_2\text{Ti}_2\text{O}_7$ was used in the high-resolution powder diffractometer (Echidna) at the OPAL reactor neutron facility,

Australian Nuclear Science and Technology Organization. The powdered sample was lightly packed into a vanadium can that was mounted in closed cycle refrigerator with 60–80 mbars of He exchange gas. All diffraction patterns were recorded over the angular range 10 to 160 degrees at a wavelength of 1.494 Å. A pattern was recorded at 3, 25 and 50 K, then in 15 K steps to 150 K, at 200 K, then in 50 K steps to 400, at 425 then 25 K steps to 550 K, and finally at 565 and 580 K. During all measurements the temperature variation was less than ± 2 K.

3.3.2 Infrared and Raman characterization

The IR spectra was measured by Evan Thatcher in Professor David Tanner's group. Temperature-dependent reflectivity was obtained using a Fourier transform spectrometer (Bruker IFS 113v) in conjunction with a liquid helium cooled Si bolometer (over 30 – 700 cm^{-1}) and a room temperature DTGS detector (over 650-3300 cm^{-1}). The reflection stage provided an angle of incidence of about 15° for the light. Temperatures between 20 and 300 K were obtained in a Hanson flow cryostat with polyethylene (far infrared) or KBr windows (midinfrared).

Raman measurements were performed on a Thermo Scientific DXR Raman microscope system. The Raman shift was measured from 50 to 3500 cm^{-1} by exciting the sample with a 532 nm photon beam from a 1 mW laser. The spectrometer was equipped with a 900 line/mm filter grating and a 50 μm spectrograph aperture. The measurement data was compiled over 10 exposures with 512 background exposures, each taken at room temperature with an exposure time of 2 seconds.

3.3.3 Dielectric characterization

To prepare parallel plate capacitors, gold electrodes were sputtered on both sides of the polished pellets followed by a painted coat of air dried silver paste.

The dielectric measurements as a function of temperature were collected with an Agilent E4980A Precision LCR Meter using a computer controlled closed cycle cryogenic workstation (CTI- Cryogenics, model 22) and a Delta 9023 oven. The measurements were carried out from 20 to 300 K in the former, and from 300 to 500 K in the later in the frequency range between 40 Hz and 2 MHz. Data at higher temperatures (373-723 K) was obtained placing the samples in a quartz tube reactor located inside a tube furnace. The thermocouple was placed in close proximity to the pellets in order to have accurate temperature control. Measurements in the frequency range from 1 kHz to 1 MHz were carried out using the Agilent E4980A Precision LCR Meter.

Impedance measurements as a function of frequency were collected using a solartron SI 1260 impedance analyser for measurements from 298 K – 473 K over the frequency range 0.1 Hz – 32 MHz. Pt wires with a diameter of 127 μm were attached to the electrodes using conductive silver paste (SPI Supplies) which was allowed to dry before the samples were installed in a glass reactor for measuring. For impedance measurements from 20 K – 300K using a computer controlled closed cycle cryogenic workstation (CTI- Cryogenics, model 22) and an Agilent 4294A Precision Impedance Analyzer with measurements obtained at 10 K intervals at frequency ranges of 40 Hz to 1 MHz.

3.4 Computational Methods

The computational calculations discussed in Chapter 6 were performed by Dr. Beverly Hinojosa. First-principles calculations were performed with Vienna *ab-initio* Simulation Package (VASP),⁵⁶⁻⁵⁹ a plane-wave density functional theory (DFT) code, using the projector augmented wave (PAW) pseudopotentials provided in the VASP

database.^{60,61} The Bi(5*d*, 6*s*, 6*p*), Ti(3*s*, 3*p*, 3*d*, 4*s*), and O(2*s*, 2*p*) orbitals were included as the valence electrons. The calculations were performed within the local density approximation (LDA)⁶² since it has been found to be more accurate than the GGA functionals for many pyrochlores.^{63,64} Electronic relaxation was performed with the conjugate gradient (CG) method accelerated using Methfessel-Paxton Fermi-level smearing with a Gaussian width of 0.1 eV.⁶⁵

CHAPTER 4 CRYSTALLOGRAPHY OF $\text{Bi}_2\text{Ti}_2\text{O}_7$ AND OTHER PYROCHLORES

4.1 Introduction

The crystallography of regular pyrochlores ($\text{A}_2\text{B}_2\text{O}_7$) is well understood. A summary of the different descriptions of the pyrochlore structure was presented in Chapter 2. This Chapter will investigate the structure of the $(\text{Sm}_x\text{Yb}_{1-x})_2\text{Ti}_2\text{O}_7$, $\text{Sm}_2(\text{Sn}_x\text{Ti}_{1-x})_2\text{O}_7$ and in particular establish whether or not the structures are displaced or ideal pyrochlores.

An in-depth structural study of $\text{Bi}_2\text{Ti}_2\text{O}_7$ will be performed as function of temperature using both neutron and synchrotron x-ray diffraction sources. For the first time the structure of $\text{Bi}_2\text{Ti}_2\text{O}_7$ will be refined experimentally and compared to previous density functional (DFT) theory calculations.

According to Esquivel-Elizondo *et al.*,²⁶ DFT calculations indicate that the atoms within the $\text{Bi}_2\text{Ti}_2\text{O}_7$ crystal do not reside in ideal pyrochlore positions. In $\text{Bi}_2\text{Ti}_2\text{O}_7$, the A cation (bismuth) is displaced from its ideal 16c (0,0,0) position to the 96g (0.015, 0.015, 0.964) site. The O(2) atom is also displaced; instead of residing in the 8a site (1/8, 1/8, 1/8) it is displaced to the 48f (x, 1/8, 1/8) position. Furthermore, previous DFT calculations have ascribed a large isotropic thermal parameter to the Ti cation.²⁶ This is caused by the bismuth displacement to the 96g site, which leads to distortion in the Bi-O bonding and this loss of symmetry results in an underbonded Ti atom. In an effort to satisfy this O underbonding the Ti cation is predicted by DFT calculations to displace to the 96g position; however, it is important to recall that DFT calculations do not take into account thermal considerations. The previous DFT calculations assumed stoichiometric bismuth titanate (*i.e.* full occupancy of the Bi and O(2) sites). Given the improved

quality of fit of the neutron diffraction found here with Bi vacancies considered, the DFT calculations of bismuth titanate were repeated with Bi and O(2) vacancies.

The proposed atomic displacements of the Bi and O' atoms in $\text{Bi}_2\text{Ti}_2\text{O}_7$ are similar to that observed in another bismuth pyrochlore, $\text{Bi}_{1.5}\text{Zn}_{0.92}\text{Nb}_{1.5}\text{O}_{6.92}$ (BZN).¹⁻³ Nonetheless, what is striking is that displacement would occur without atomic substitutions and multiple site occupancy like in BZN and related pyrochlores.

4.2 Crystal Structure of $(\text{Sm}_x\text{Yb}_{1-x})_2\text{Ti}_2\text{O}_7$ ($x = 0.25, 0.5, 0.75$)

Pure pyrochlore phase of $(\text{Sm}_x\text{Yb}_{1-x})_2\text{Ti}_2\text{O}_7$ ($x = 0.25, 0.5, 0.75$) was formed when calcined at 1250°C and sintered at the same temperature (Figure 4-1). The XRD pattern shows no reflections associated with any impurities of any other related superstructures.

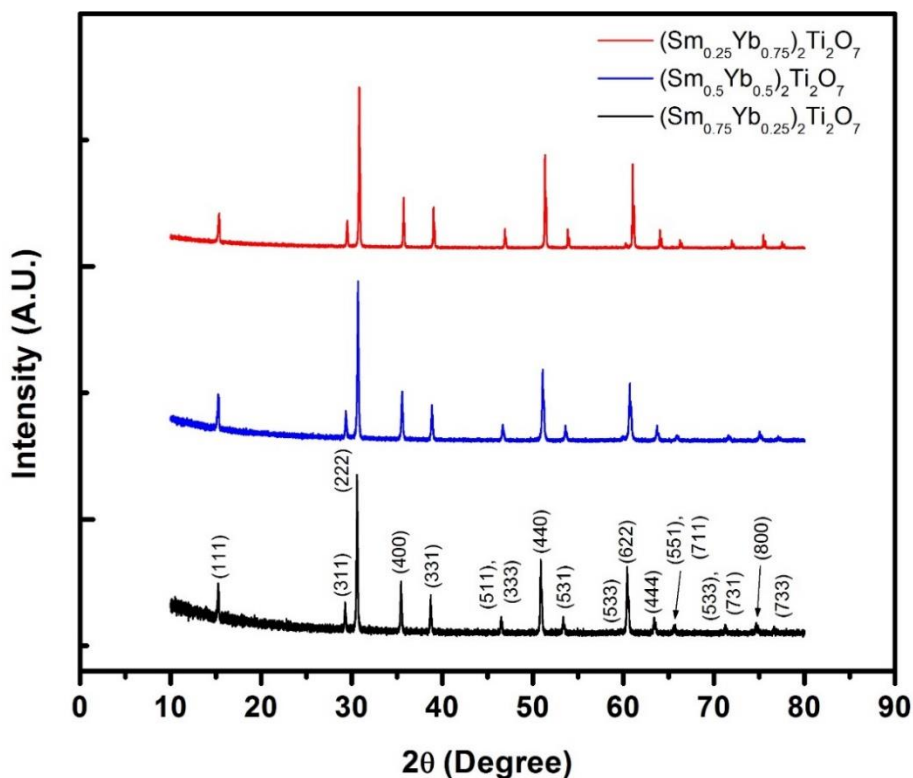


Figure 4-1. XRD patterns of $(\text{Sm}_{0.25}\text{Yb}_{0.75})_2\text{Ti}_2\text{O}_7$, $(\text{Sm}_{0.50}\text{Yb}_{0.50})_2\text{Ti}_2\text{O}_7$, and $(\text{Sm}_{0.75}\text{Yb}_{0.25})_2\text{Ti}_2\text{O}_7$.

As expected, there are shifts in 2θ , indicating changes in the lattice parameters.

The lattice parameters were calculated by the Nelson-Riley function:

$$a = a_0 - a_0 k \left(\frac{\cos^2 \theta}{\sin \theta} + \frac{\cos^2 \theta}{\theta} \right) \quad (4-1)$$

where a is the apparent lattice parameter, a_0 is the lattice parameter, and k is a constant. The Nelson-riley function is used to correct for the sample displacement error. Table 4-1 lists an example of the $\cos^2 \theta / \sin \theta + \cos^2 \theta / \theta$ parameter and the apparent lattice based on a single reflection.

Table 4-1. The 2θ positions, the corresponding (hkl), the $\cos^2 \theta / \sin \theta + \cos^2 \theta / \theta$ parameter, and the apparent lattice parameter of $(\text{Sm}_{0.25}\text{Yb}_{0.75})_2\text{Ti}_2\text{O}_7$.

2θ (degrees)	hkl	$\cos^2 \theta / \sin \theta + \cos^2 \theta / \theta$	a (Å)
15.259	111	7.59520	10.0453
29.268	311	3.98171	10.1083
30.585	222	3.81232	10.1133
35.434	400	3.29666	10.1211
38.711	331	3.02061	10.1269
50.869	440	2.99371	10.1420
53.362	531	2.18986	10.1451
60.416	622	1.92359	10.15144

Figure 4-2 indicates the apparent lattice parameter a vs. $\cos^2 \theta / \sin \theta + \cos^2 \theta / \theta$ and the resulting a_0 . The lattice parameters, shown in Table 4-2 decrease as the Sm content is decreased, this is expected as Sm has a larger ionic radius than Yb.

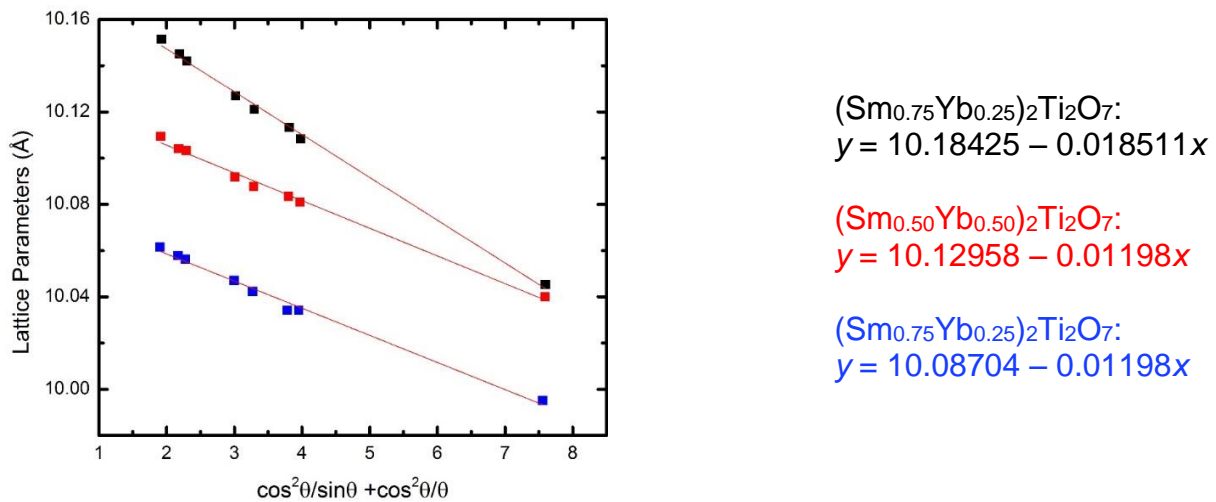


Figure 4-2. Nelson-Riley function for the lattice parameter calculations of $(\text{Sm}_{0.25}\text{Yb}_{0.75})_2\text{Ti}_2\text{O}_7$, $(\text{Sm}_{0.50}\text{Yb}_{0.50})_2\text{Ti}_2\text{O}_7$, and $(\text{Sm}_{0.75}\text{Yb}_{0.25})_2\text{Ti}_2\text{O}_7$.

Table 4-2. Lattice Parameters of $(\text{Sm}_{0.25}\text{Yb}_{0.75})_2\text{Ti}_2\text{O}_7$,
 $(\text{Sm}_{0.50}\text{Yb}_{0.50})_2\text{Ti}_2\text{O}_7$, and $(\text{Sm}_{0.75}\text{Yb}_{0.25})_2\text{Ti}_2\text{O}_7$

Compound	Lattice Parameter (Å)
$(\text{Sm}_{0.25}\text{Yb}_{0.75})_2\text{Ti}_2\text{O}_7$	10.08704
$(\text{Sm}_{0.50}\text{Yb}_{0.50})_2\text{Ti}_2\text{O}_7$	10.12958
$(\text{Sm}_{0.75}\text{Yb}_{0.25})_2\text{Ti}_2\text{O}_7$	10.18425

Structural studies on BZN, a pyrochlore that has atomic displacements, have shown that an extra peak (corresponding to a 442 hkl) not indexed by the ideal pyrochlore structure will be present in the XRD. This peak is absent in both the powder and the sintered pellets which shows that these compounds do not have atomic displacements, only chemical substitution.

4.3 Crystal Structure of $\text{Sm}_2(\text{Sn}_{0.5}\text{Ti}_{0.5})_2\text{O}_7$

Pure pyrochlore phase of $\text{Sm}_2(\text{Sn}_x\text{Ti}_{1-x})_2\text{Ti}_2\text{O}_7$ ($x = 0.25, 0.5, 0.75$) was formed when calcined at 1100°C (Figure 4-3). The XRD pattern show no reflections associated with any impurities of any other related superstructures. As the Sn content increases in the material some reflections increased decreased in intensity, in particular the (111), (113), and (133) peaks at 15° , 29° , and 38° respectively. These changes in intensities are consistent with the patterns of $\text{Sm}_2\text{Sn}_2\text{O}_7$ and $\text{Sm}_2\text{Ti}_2\text{O}_7$ in both theoretical patterns and those reported in literature.⁶⁶

The $\text{Sm}_2(\text{Sn}_x\text{Ti}_{1-x})_2\text{O}_7$ powders were then sintered at 1300°C , however both $\text{Sm}_2(\text{Sn}_{0.25}\text{Ti}_{0.75})_2\text{O}_7$ and $\text{Sm}_2(\text{Sn}_{0.75}\text{Ti}_{0.25})_2\text{O}_7$ showed the presence of impurity peaks, while $\text{Sm}_2(\text{Sn}_{0.5}\text{Ti}_{0.5})_2\text{O}_7$ sintered at the same temperature resulted in a phase pure pyrochlore.

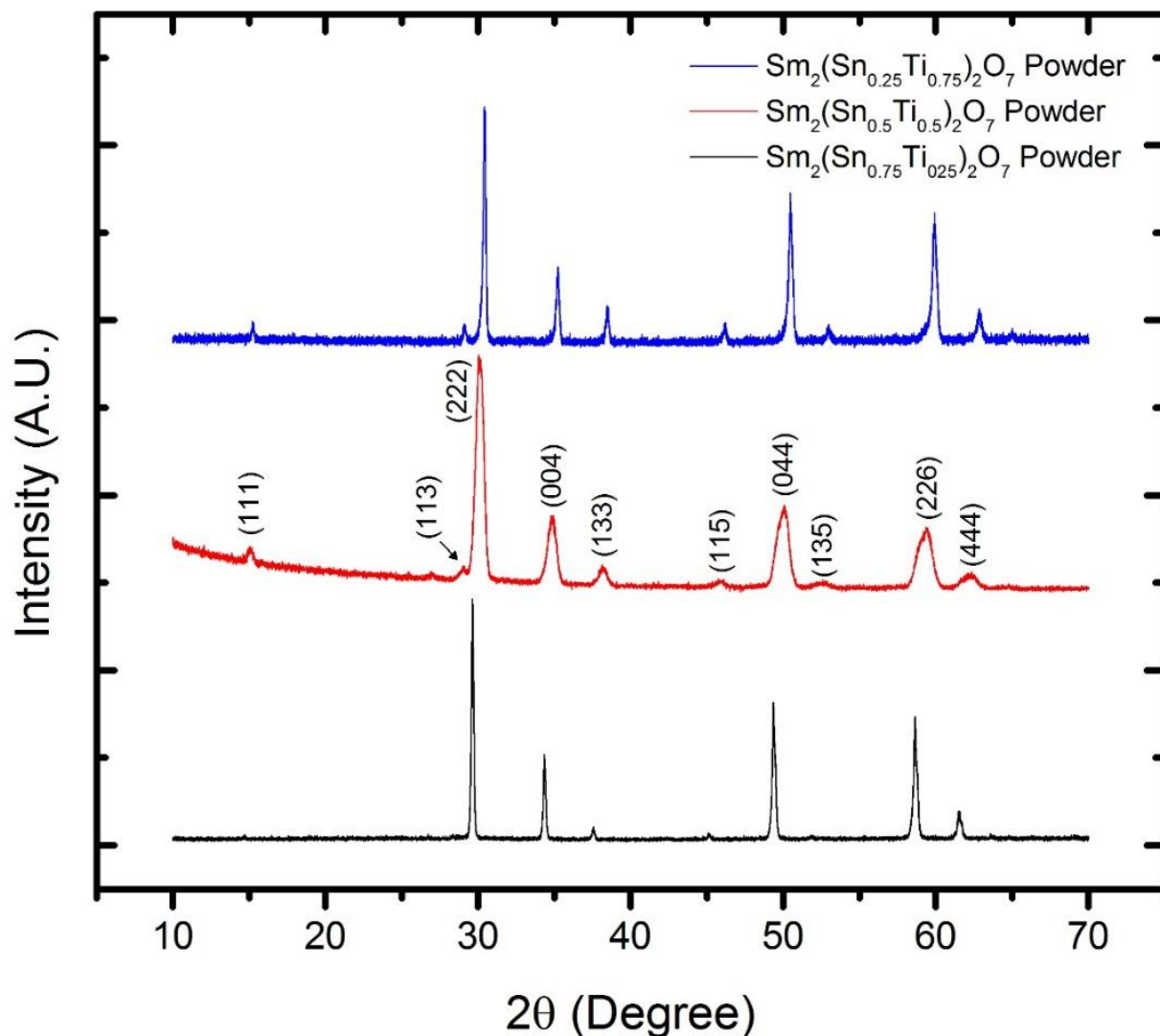


Figure 4-3. XRD patterns of $\text{Sm}_2(\text{Sn}_{0.25}\text{Ti}_{0.75})_2\text{O}_7$, $\text{Sm}_2(\text{Sn}_{0.5}\text{Ti}_{0.5})_2\text{O}_7$, and $\text{Sm}_2(\text{Sn}_{0.75}\text{Ti}_{0.25})_2\text{O}_7$.

Similar to the $(\text{Sm}_x\text{Yb}_{1-x})_2\text{Ti}_2\text{O}_7$ system, the $\text{Sm}_2(\text{Sn}_x\text{Ti}_{1-x})_2\text{O}_7$ system does not have the presence of the (442) peak which indicates that there is no evidence of atomic displacement in the material.

4.4 Structural Study of $\text{Bi}_2\text{Ti}_2\text{O}_7$

Table 4-1 shows the refined positions and parameters of the neutron, HR-XRD, and DFT calculations performed in the following subsections.

Table 4-3. Refined positions and parameters of Bi₂Ti₂O₇ at 3 K through neutron diffraction (a), high resolution XRD (b), non-stoichiometric Bi_{1.8125}Ti₂O_{6.75} DFT calculations (c), stoichiometric DFT calculations (d)

a (Å)		10.3310 ^a				
		10.346				
		10.335 ± 0.005 ^c				
		10.335 ± 0.005 ^d				
Atom		x	y	z	B _{iso} (Å ²)	Occupancy
Bi	96g	0.0166 ^a	0.0166 ^a	0.9707 ^a	1.11 ^a	0.075 ^a
		0.0181	0.0181	0.971	0.011	0.1694
		0.015 ^c	0.015 ^c	0.964 ^c	1.88 ^c	0.0755 ^c
		0.015 ^d	0.015 ^d	0.964 ^d	0.079 ^d	1/6 ^d
		0.5 ^a	0.5 ^a	0.5 ^a	0.60 ^a	0.083 ^a
Ti	16d	0.5	0.5	0.5	0.008	1
		0.5 ^c	0.5 ^c	0.5 ^c	2.41 ^c	0.0833 ^c
		0.5 ^d	0.5 ^d	0.5 ^d	1.82 ^d	1 ^d
O(1)	48f	0.4312 ^a	0.125 ^a	0.125 ^a	0.92 ^a	0.25 ^a
		0.433	0.125	0.124	0.018	1
		0.431 ^c	0.125 ^c	0.125 ^c	2.21 ^c	0.25 ^c
		0.431 ^d	0.125 ^d	0.125 ^d	0.800 ^d	1 ^d
O(2)	8a	0.125 ^a	0.125 ^a	0.125 ^a	2.66 ^a	0.031 ^a
		0.145	0.125	0.125	0.003	0.1688
		0.431 ^c	0.125 ^c	0.125 ^c	2.21 ^c	0.25 ^c
		0.136 ^d	0.125 ^d	0.125 ^d	0.237 ^d	1/6 ^d

4.4.1 Synchrotron X-ray diffraction

The synchrotron powder X-ray diffraction pattern (SXRD) recorded for the sample of Bi₂Ti₂O₇ is illustrated in Figure 4-1 and the refinement is shown in Figure 4-2, together with the best Rietveld fit. Attempts to model the data with the Bi at the 16c site (0 0 0) resulted in an unacceptably high χ^2 value of 8.24 and Bi displacement parameter $U_{iso}(\text{Bi}) = 0.0694(3) \text{ \AA}^2$. High displacement parameters are commonly associated with vacancies. Refinements where the Bi occupancy was also varied resulted in a small improvement in χ^2 to 7.37 but did not significantly reduce the value of $U_{iso}(\text{Bi}) = 0.0667(3) \text{ \AA}^2$ with the Bi stoichiometry being reduced from 2.00 to 1.64(5). Examination of the Rietveld difference profile revealed a number of discrepancies therefore disorder of the Bi cation was considered. The final fit illustrated in Figure 4-2 allows the Bi to displace to the 96g sites and yielded χ^2 to 2.15 with $U_{iso}(\text{Bi}) = 0.0117(3) \text{ \AA}^2$. The Bi

stoichiometry was estimated to be 1.70(1). Note that no absorption correction was applied to the SXRD data.

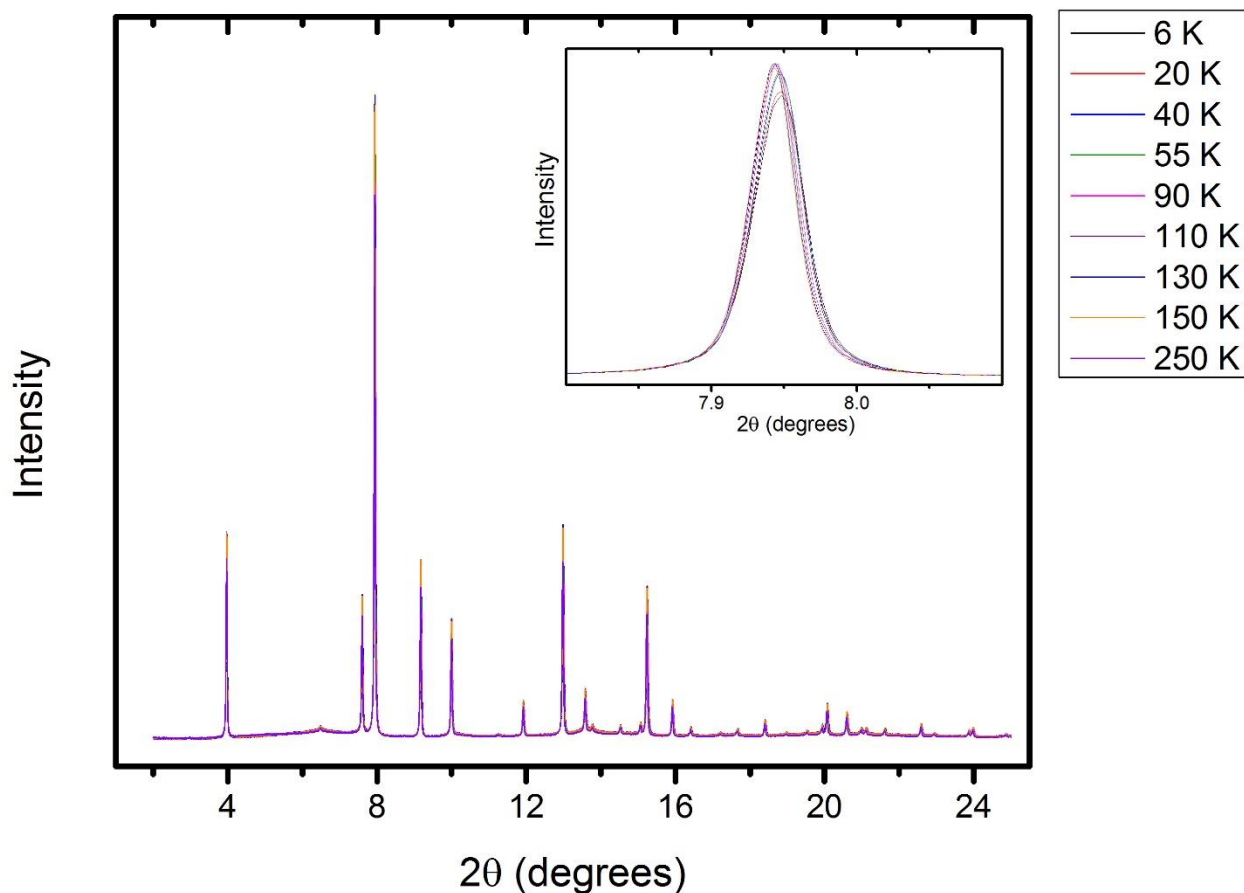


Figure 4-4. High resolution XRD at temperatures from 6 k to 250 K. Inset is the (111) peak at 8°.

The possibility that the Bi was displaced to the 96*h* sites was also investigated. This resulted in a comparable quality fit to the data but it was not possible to distinguish between these by diffraction methods alone. Whilst disorder onto the 96*h* and 96*g* sites are not crystallographic equivalent descriptions they both describe displacement of the Bi cation away from the center of the O(1) to a 6-site puckered hexagon.

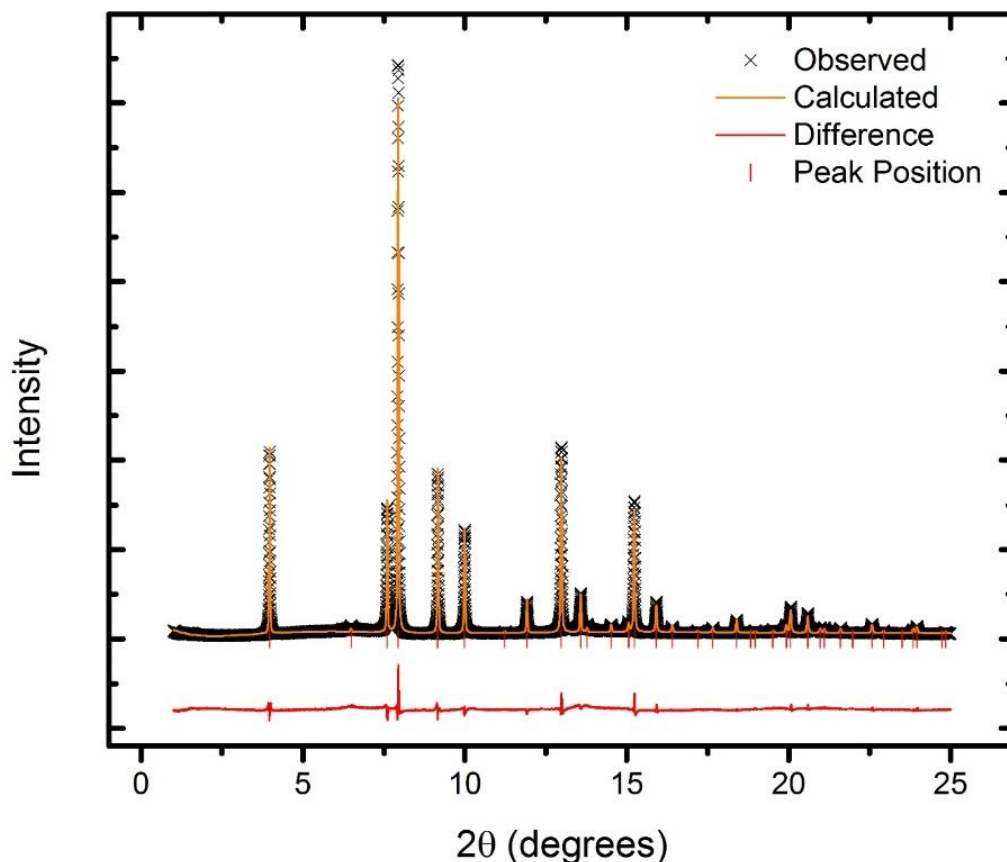


Figure 4-5. Rietveld fit of the room temperature x-ray diffraction pattern. Only peaks ascribed to the cubic pyrochlore phase were detected.

Unlike the neutron diffraction, the high-resolution XRD did not display a low temperature saturation in the lattice parameter below 150 K (Figure 4-3).

In summary the SXRD data clearly demonstrates there to be appreciable non correlated atomic displacements of the Bi cation, and suggest the Bi moves around 0.4 Å away from the position it would occupy in the ideal pyrochlore structure. Given the large X-ray scattering power of the heavy Bi cations the refinements were insensitive to either disorder of the other ions or the possibility of vacancies on the O(2) sites. Such vacancies are required to charge balance.

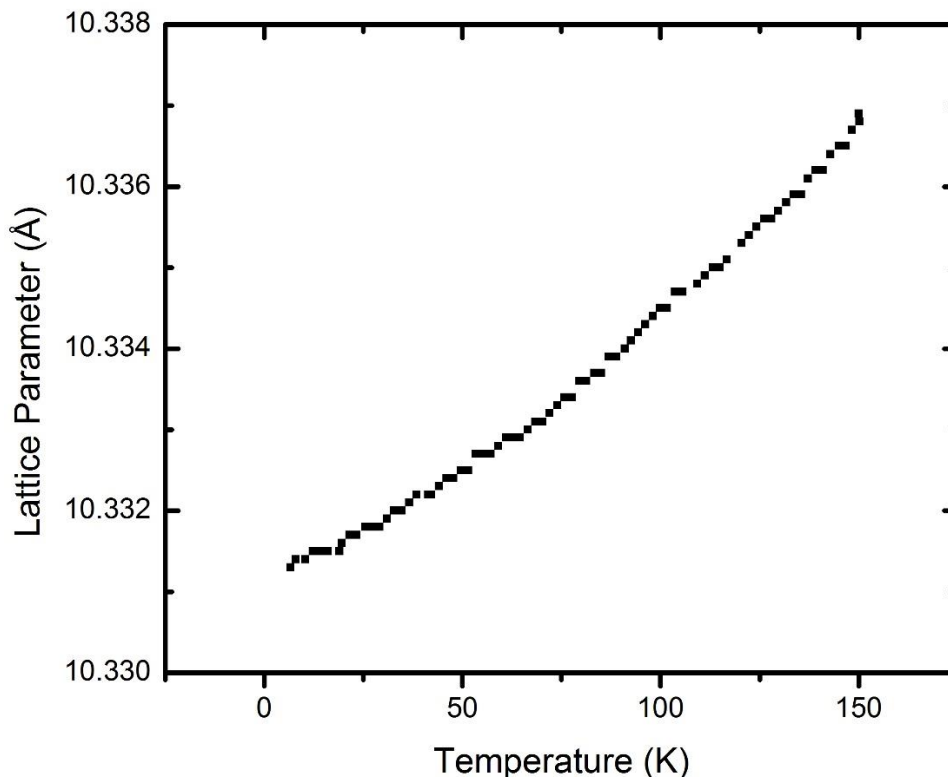


Figure 4-6. The lattice parameter between 6 K and 150 K, unlike in neutron diffraction a low temperature saturation is not observed.

4.4.2 Neutron diffraction

All the reflections observed in a powder neutron diffraction pattern collected for $\text{Bi}_2\text{Ti}_2\text{O}_7$ at room temperature using 1.622 Å neutrons could be indexed to a cubic cell in $\text{Fd}\bar{3}\text{m}$ with $a = 10.3410(2)$ Å. No evidence was found for any spurious peaks in the pattern and it was concluded that the material was single phase. Data were then collected between 3 and 580 K using 1.494 Å neutrons. These patterns showed some weak reflections due to parasitic scatter from the cryostat and these were treated as excluded regions in the subsequent structural refinements (Figure 4-4). A second feature of the patterns was the presence of some structure in the background. This additional diffuse scattering is indicative of some short range disorder in the structure, possibly associated with the anion sub-lattice. Examination of the SXRD data also

revealed some very weak diffuse character, this behavior was weaker in the SXRD pattern than in the ND is consistent with this being caused by anion disorder.

As described above fitting the room temperature neutron diffraction pattern to the ideal pyrochlore structure yielded unusually large displacement parameters for the Bi cations, 5.3(1), suggesting the possibility of substantial non-correlated atomic displacements.

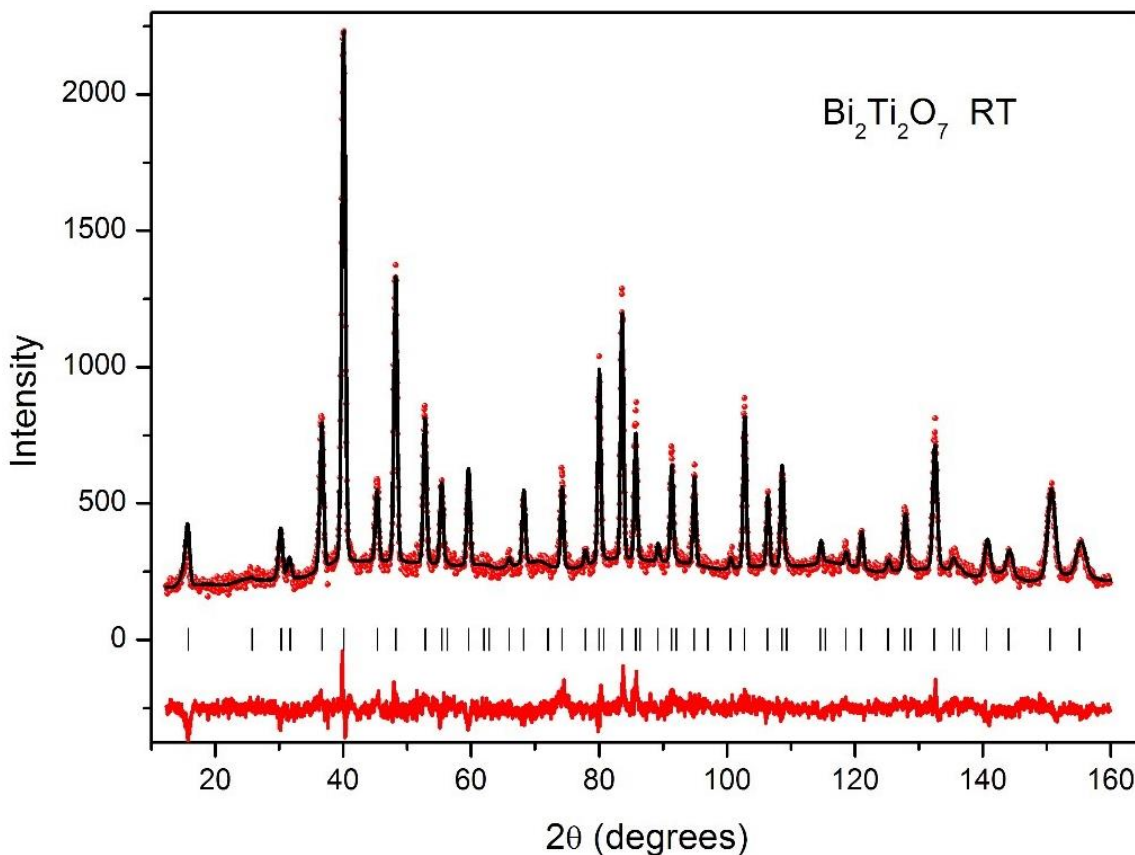


Figure 4-7. Rietveld fit of the room temperature neutron diffraction pattern. Only peaks ascribed to the cubic pyrochlore phase were detected.

It is well established that the Bi cations, located at the center of a distorted scalenohedron of 8 anions are susceptible to disorder. Recent crystallographic studies of $\text{Bi}_{2-x}\text{Yb}_x\text{Ru}_2\text{O}_{7-\delta}$ and $\text{Bi}_2\text{CrTaO}_7$ have demonstrated the static non-correlated atomic displacements of the Bi cations from the $16c(0\ 0\ 0)$ site to a $96h(0\ y\ -y)$ site occurs in

Bi pyrochlores. Allowing for disorder of the Bi cation lead to a significant improvement in the fit and a noticeably reduction in the magnitudes of the refined displacement parameters for the Bi cations, although it did not substantially change the refined value of the unknown x parameter of O(1) (from 0.4330(2) to 0.4310(1)).

The possibility of vacancies at the Bi site was investigated and the addition of this parameter led to a significant improvement in the quality of the fit. Bi vacancies have been observed in a number of other pyrochlores including $\text{Bi}_{1.89}\text{Ru}_2\text{O}_{6.92}$, $\text{Bi}_{1.89}\text{GaSbO}_{6.84}$ and $\text{Bi}_{1.95}\text{Rh}_2\text{O}_{6.83}$. Refinement of the occupancy of the O(2) site demonstrated this was not fully occupied; and in the final refinement cycles the occupancies of the Bi and O(2) sites were constrained to maintain charge neutrality. As noted by Avdeev et al.,⁶⁷ displacement of the Bi away from the 16c sites is expected to force the O(2) atoms away from the 8a (1/8 1/8 1/8) sites to a disordered 32e (x x x) site. Attempts to verify this were inconclusive using the neutron results but are taken into consideration for the DFT work.

Finally the possibility of disorder of the Ti cations was considered. Although stable refinements could be obtained if the Ti was disordered to (x x y) these invariably resulted in physically unrealistic displacement parameters for the Ti cations and we conclude that any such disorder must be localized.

The temperature dependence of the lattice parameter, is illustrated in Figure 4-5, shows normal thermal expansion behavior at high temperatures and saturation effects as the temperature approaches 0 K. The behavior was well modelled by fitting to a function of the form:

$$V_o = V_1 + V_2\Theta \coth\left(\frac{\Theta}{T}\right) \quad 6-1$$

The temperature, Θ included to account for the low temperature saturation of thermal expansion was estimated to be ~ 210 K. This is somewhat higher than the value typically seen for thermal expansion of oxides such as perovskites.

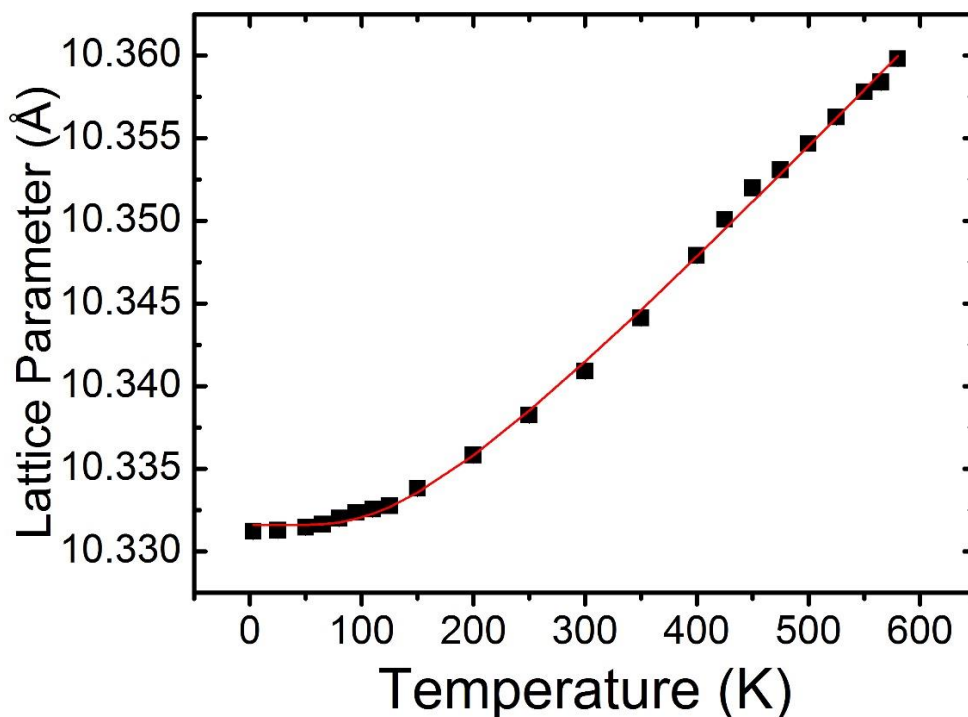


Figure 4-8. Temperature dependence of the lattice parameters of $\text{Bi}_2\text{Ti}_2\text{O}_7$. Where not apparent the effective standard deviations are smaller than the symbols. The solid lines is a fit to Equation 6-1 where $\Theta = 210$ K.

4.4.3 DFT calculations

The Bi displacements and the resulting change in the positional parameter for O(1) observed from neutron diffraction (summarized in Table 4-1) are in excellent agreement with the recent predictions for stoichiometric bismuth titanate from DFT.²⁶

As previously stated, the O(2) atoms are located at the ideal 8a position with a large isotropic thermal parameter of 2.66 according to the neutron work. In stoichiometric DFT calculations, O(2) was found to displace to the $48f(0.136, 1/8, 1/8)$ position, which corresponded to a displacement of approximately 0.11 Å towards the

edges of the Bi_4O tetrahedra. The large isotropic parameter reported here for O(2) by neutron diffraction corresponds to an average thermal displacement of 0.18 Å which is greater than the displacement magnitude predicted by stoichiometric DFT calculations .

The stoichiometric DFT calculations also predicted a displacement of Ti from the high symmetry site in order to satisfy the bond valence for O after Bi displacement. However, with the lack of experimental evidence the Ti displacement was explained as Ti centered at the high symmetry site with an isotropic thermal parameter $B_{\text{iso}}=1.82$. In comparison with the isotropic thermal parameter from neutron diffraction reported in Table 4-1, the ellipsoid of the Ti in the stoichiometric bismuth titanate predicted by DFT is more than double the size based on the neutron diffraction reported here.

The A 1x1x2 supercell was created to provide more flexibility in the possible stoichiometry configurations. Following optimizations, the resulting atomic positions are also included in Table 4-1. There are two major differences between the previously reported structure and that found here by DFT the nonstoichiometric calculations.

First, the isotropic displacement parameters are considerably larger for the nonstoichiometric calculations. This is because there were significant local effects due to the vacancies. Specifically, the Bi and O(2) displacements were substantially larger isolated near a vacancy. It was found that near a vacancy the atomic displacement magnitude could be nearly double that away from a vacancy. Since neutron diffraction averages over a sample containing many unit cells, the atomic positions from the DFT calculations were averaged as well. This averaging results in larger isotropic thermal parameters than those reported for the stoichiometric structure and those determined from neutron diffraction. This is not unexpected given that the Bi and O(2) atoms will

displace to help compensate for the loss of bonding due to the inclusion of vacancies. Specifically, a Bi cation located at an O(2) vacancy will need to bond more strongly with the remaining O(2) anion as well as the six O(1) forming the puckered ring perpendicular to the O(2)-Bi-O(2) bonding axis. This will result in an increased displacement of the Bi and the O(2) atoms. Also, through a secondary effect, the Ti and O(1) atoms will also be affected by the vacancies as seen by the large isotropic thermal parameters for both in Table 4-1.

Secondly, and for the same reasons, the displacement of the O(2) atom was larger here. Again the displacement magnitude was considerably larger near vacancies and this led to a larger x parameter identified here versus the stoichiometric DFT simulation. Additionally, given the large isotropic parameter for O(2) even after displacement, attempts were made to center the O(2) at the 32e position but the resulting isotropic parameter was larger at 3.67 and the actual displacement of the O(2) atoms was not accurately captured.

The change in Gibbs free energy for the non-stoichiometric and stoichiometric $\text{Bi}_2\text{Ti}_2\text{O}_7$ structure was defined as the vacancy formation energy in electron volts (eV). The total energy change due to atomic displacements at room temperature is -1.925 eV, while the vacancy formation entropy is 3.13 eV at room temperature. The inclusion of oxygen vacancies costs considerable energy when compared with the favourable energy change due to atomic displacements. Other oxides, such as SrTiO_3 and BaTiO_3 have a vacancy formation energy of 6.88 eV⁶⁸ and 2.0 eV⁶⁹, respectively. By comparing the vacancy formation energy, an oxygen vacancy is more favorable in $\text{Bi}_2\text{Ti}_2\text{O}_7$ than in SrTiO_3 but less favorable than in BaTiO_3 .

4.5 Conclusion

The structural characterization of $(\text{Sm}_x\text{Yb}_{1-x})_2\text{Ti}_2\text{O}_7$ and $\text{Sm}_2(\text{Sn}_x\text{Ti}_{1-x})_2\text{O}_7$ ($x = 0.25, 0.5, 0.75$) was presented here. It was found that both systems formed a phase pure pyrochlore phase and the presence of the (442) diffraction peak was not detected. Therefore, both of the Sm systems only have the presence of substitution and do not have atomic displacements found in most Bi-pyrochlores.

A more in-depth structural study of $\text{Bi}_2\text{Ti}_2\text{O}_7$ was performed using neutron diffraction, synchrotron x-ray diffraction (SXR), and DFT. Both the neutron and SXR revealed displacements of the Bi cation to the 96g site and the displacement of the O' oxygen. The neutron and SXR both showed a better fit when vacancies were considered on the Bi and O(1) site, the energy of formation of non-stoichiometric $\text{Bi}_2\text{Ti}_2\text{O}_7$ was found to be 3.13 eV at room temperature.

The proposed atomic displacements of the Bi and O' atoms in $\text{Bi}_2\text{Ti}_2\text{O}_7$ are similar to that observed in another bismuth pyrochlore, $\text{Bi}_{1.5}\text{Zn}_{0.92}\text{Nb}_{1.5}\text{O}_{6.92}$ (BZN).¹⁻³ Nonetheless, what is striking is that displacement would occur without atomic substitutions and multiple site occupancy like in BZN and related pyrochlores.

CHAPTER 5 DIELECTRIC PROPERTIES OF $\text{Bi}_2\text{Ti}_2\text{O}_7$ AND OTHER PYROCHLORES¹

5.1 Introduction

Over the last decades, extensive research has been done in order to explain a phenomenon that is common to several pyrochlores and all Bi-pyrochlores: a temperature and frequency-dependent dielectric relaxation consistent with glass-like dipolar mechanisms.^{12,22,23,45,70,71} On cooling below room temperature, these materials exhibit a step-like decrease in the real part of the dielectric permittivity accompanied by a broad frequency-dependent peak in the imaginary part. As a consequence of this relaxation, at microwave frequencies the temperature at which the dielectric loss peaks (T_m), move towards room temperature with increasing frequency as observed in $\text{Bi}_{1.5}\text{Zn}_{0.92}\text{Nb}_{1.5}\text{O}_{6.92}$, thus limiting GHz frequency applications.² [It is important to note that this pyrochlore is not fully stoichiometric as previously demonstrated, but it is usually reported with nominal composition $\text{Bi}_{1.5}\text{Zn}_{1.0}\text{Nb}_{1.5}\text{O}_7$ (BZN).^{12,45}]

Several potential explanations for the observed relaxation in Bi-pyrochlores have been proposed including the hopping of the disordered cations at the A equivalent sites,¹² reorientation of unstable dipoles due to interactions in the A_2O' sub-structure,⁷² and chain rotation modes.²³ Furthermore, until recently, it was considered that chemical disorder (more than one cation species sharing the A or B sites), highly polarizable lone pair cations such as Bi^{3+} , and atomic displacements are responsible for the relaxation behavior. However, our work on calcium titanium niobate⁷³ proved that pyrochlores can exhibit dielectric relaxation even in the absence of a highly polarizable A-site cation or a

¹ Adapted from Christopher Turner *et. al.* Dielectric properties and relaxation of $\text{Bi}_2\text{Ti}_2\text{O}_7$. *Journal of the American Ceramic Society*, doi:10.1111/jace.12803 (2014).

lone-pair element. As such, the measurement of the dielectric properties of $\text{Bi}_2\text{Ti}_2\text{O}_7$, a cubic pyrochlore without substitutions on both the A and B site, is extremely desirable because this compound could help isolate the possible causes and aid in determining the necessary and sufficient conditions for the observed dielectric relaxation.

Bismuth titanate is expected to have dielectric relaxation as calculations employing density functional theory (DFT) have demonstrated the possibility of atomic (ionic) jumps among equivalent crystallographic positions associated with a low activation energy.⁷⁴ If this prediction is confirmed, this would mean that non-correlated atomic displacements are a necessary condition for relaxation. Even if there is no typical dielectric relaxation observed the absence of relaxation can prove that substitutional cations would be a required condition for dielectric relaxation in pyrochlores.

In order to isolate the effect of substitutional cations on dielectric relaxation $(\text{Sm}_x\text{Yb}_{1-x})_2\text{Ti}_2\text{O}_7$ and $\text{Sm}_2(\text{Sn}_x\text{Ti}_{1-x})_2\text{O}_7$ ($x = 0.25, 0.5, 0.75$) were synthesized. The appearance of relaxation in these compounds would prove that substitutional cations are sufficient for dielectric relaxation

In this Chapter, the dielectric properties of $\text{Bi}_2\text{Ti}_2\text{O}_7$, $(\text{Sm}_x\text{Yb}_{1-x})_2\text{Ti}_2\text{O}_7$ ($x = 0.25, 0.5, 0.75$), and $\text{Sm}_2(\text{Sn}_{0.5}\text{Ti}_{0.5})_2\text{O}_7$ are comprehensively studied as a function of temperature and frequency in order to clarify the presence of relaxation in this material, and in turn, better understand the nature of the dielectric relaxation phenomenon observed in pyrochlores.

5.2 Dielectric Analysis of $\text{Bi}_2\text{Ti}_2\text{O}_7$

5.2.1 Dielectric analysis as a function of temperature

The measured relative permittivity at 100 kHz and 298 K was 115 while $\tan \delta$ (dielectric loss) was 0.0064. The obtained dielectric permittivity is in agreement with similar bismuth pyrochlores such as BZN that has a permittivity of 150 and $\tan \delta$ of <0.008 .

The values for the real and the imaginary parts of the dielectric permittivity as a function of temperature and fixed frequency are illustrated in Figure 5-1A for BZN (the result of re-measuring a sample from previous work),³ and in Figure 5-1B for $\text{Bi}_2\text{Ti}_2\text{O}_7$. The dielectric behavior of BZN is characteristic of Bi-pyrochlores, i.e., a low temperature frequency dispersive dielectric relaxation is observed where T_m , the temperature where the ϵ'' is at a maximum value for a specific frequency range, shifts to higher temperatures with increasing measuring frequency. Also, the loss value at T_m and the width and magnitude of the loss peak increases with increasing frequency. In addition, above T_m , the dielectric permittivity of BZN at different frequencies seems to converge to the same value as temperature is increased. However, bismuth titanate, despite being a Bi-pyrochlore, does not have the same behavior. Even though it is clear that near room temperature the relative permittivity of $\text{Bi}_2\text{Ti}_2\text{O}_7$ appears to reach a broad plateau or maximum (except at low frequency as seen at 10 kHz), it is not accompanied by a response in the imaginary part as in the case of BZN. This points to the possibility of a phase transition being responsible for the permittivity change in $\text{Bi}_2\text{Ti}_2\text{O}_7$.

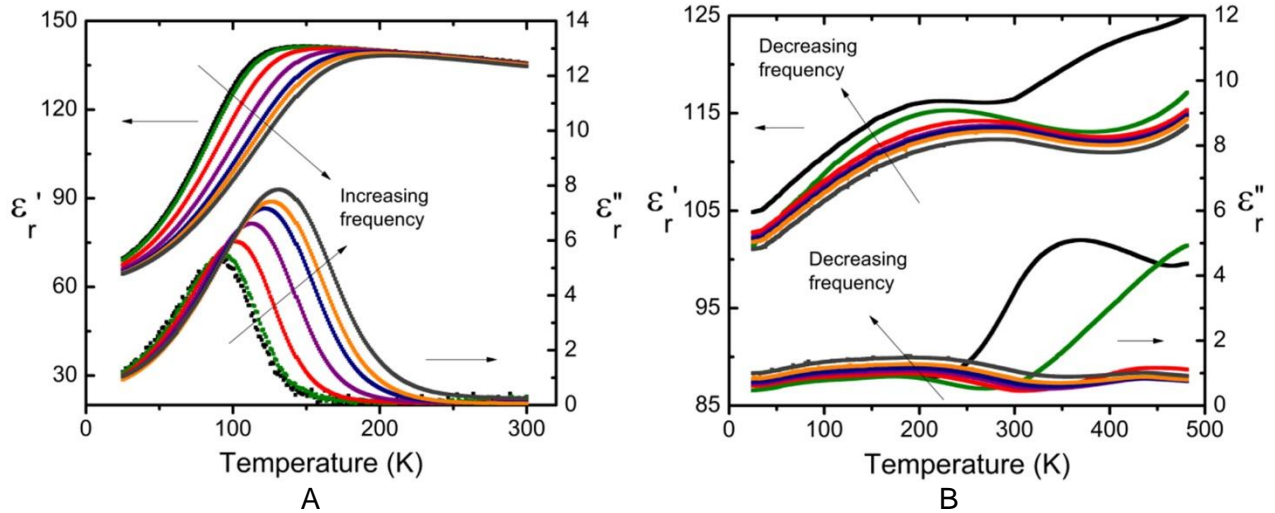


Figure 5-1. The real and imaginary part of the dielectric permittivity as a function of temperature from 10 kHz of A) BZN and B) $\text{Bi}_2\text{Ti}_2\text{O}_7$.

A similar phenomenon is observed in Gd_3NbO_7 , a dielectric with a weberite-type structure, an anion deficient fluorite superstructure, similar to the pyrochlore structure.⁷⁵ The measurement was extended up to 483 K looking for indications of dielectric relaxation but was not observed. From Figure 5-1B it is evident that the dielectric permittivity of $\text{Bi}_2\text{Ti}_2\text{O}_7$ at different frequencies does not converge to a common value as in BZN. At 10 kHz (the lowest frequency in Figure 5-1B) the onset of a peak in the imaginary part is observed but the increasing conductivity prevents further analysis. Therefore, another measurement was carried out including frequencies as low as 80 Hz. The resulting plot is depicted in Figure 5-2. From this plot it is evident that at low frequencies (<10 kHz) a type of dielectric relaxation is taking place. Nonetheless, the shape of the loss curves does not follow the observed pattern in BZN, specifically, in Bi-pyrochlores the loss peaks appear at the same low temperature, which is not the case for $\text{Bi}_2\text{Ti}_2\text{O}_7$, suggesting a different origin for the relaxation. Furthermore, given the low frequency driving the phenomenon, it is most likely indicative of space charge polarization.

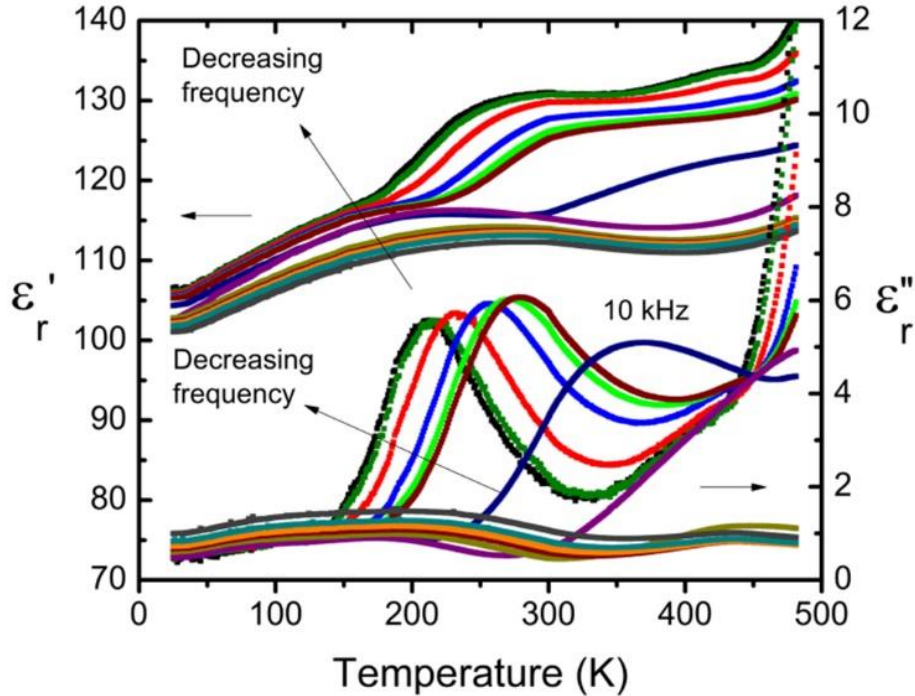


Figure 5-2. Imaginary and real part of the dielectric permittivity as a function of temperature from 80 Hz to 2 MHz.

To explore the possibility of phase transition as the reason for the dielectric response, differential scanning calorimetry (DSC) was performed on a $\text{Bi}_2\text{Ti}_2\text{O}_7$ sample from 2 to 200 K. The low temperature DSC did not reveal a phase transition. It is important to note that detailed structural studies of BZN have not revealed any phase transition² and therefore the lack of a transition for $\text{Bi}_2\text{Ti}_2\text{O}_7$ is not surprising.

Back on the dielectric response presented in Figure 5-2, it is worth mentioning that despite the diffuseness in T_m , the relaxation in $\text{Bi}_2\text{Ti}_2\text{O}_7$, where the dielectric permittivity begins to decrease, occurs at relatively higher temperatures than in BZN (and many other Bi-pyrochlores studied so far).

Employing the Arrhenius Equation, the Debye model corresponding to a single relaxation time was followed to fit the data and determine the activation energy (E_a) and the attempt jump frequency or characteristic frequency (ν_0) of the relaxation phenomenon in $\text{Bi}_2\text{Ti}_2\text{O}_7$:

$$v_r = v_0 \exp\left(\frac{-E_a}{k_B T_m}\right) \quad (5-1)$$

where v_r is the frequency of the relaxation peak in the imaginary part of the permittivity, and k_B is the Boltzmann constant. The relaxation behavior was found to follow the Arrhenius Equation quite well (Figure 5-3). The calculated activation energy was 0.162 eV (equivalent to 1881.3 K). It is simply anecdotal to note that this value is in agreement with calculated values from DFT (0.11-0.21⁷⁴) and is similar to that of BZN (0.136 eV,¹³ 0.202 eV¹²). However, the attempt jump frequency (9.91×10^5 Hz = ~1 MHz) is several orders of magnitude lower (10^{12} Hz), which makes the comparison of activation energies pointless since different relaxation mechanisms are likely taking place.

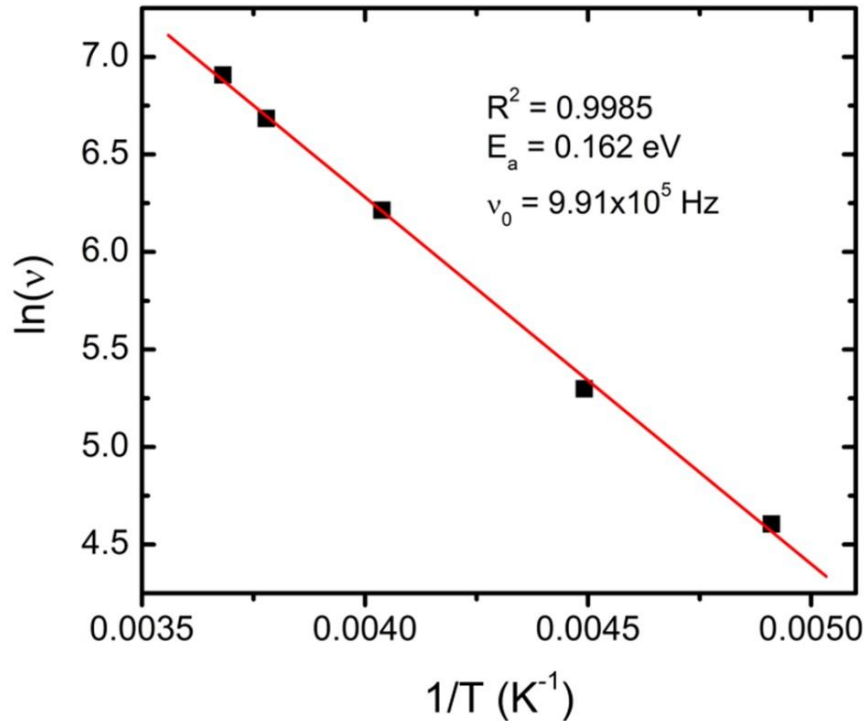


Figure 5-3. Arrhenius plot of $Bi_2Ti_2O_7$ dielectric relaxation using Equation 5-1.

As previously stated, the low attempt jump frequency suggests the presence of space charge polarization within the grain boundaries or an interaction between the

surface of the sample and the electrode. Nonetheless, and for the sake of argument, if one were to assume that the observed phenomenon is a typical dipolar (ionic) dielectric relaxation; such low frequency would imply the involvement of a large vibrating mass or a cooperative displacement in the form of rigid unit modes.^{76,77} Recalling, in BZN the characteristic frequency in the order of 10^{12} Hz is normally attributed to the attempt jump frequency of the hopping of A ions within the A_2O' substructure that is governed by the O'-A'-O' phonon vibration.⁴⁵ If a rough calculation is used considering harmonic oscillators ($m_2/m_1 = v_1^2/v_2^2$), a mass difference of 12 orders of magnitude is obtained between BZN and $Bi_2Ti_2O_7$. In that case, the low frequency dielectric relaxation in $Bi_2Ti_2O_7$ requires a vibrating mass in the order of $\sim 5 \times 10^{10}$ unit cells, which means that cooperative displacement would be occurring. Given this unlikely event, space charge polarization in the form of hopping or interfacial polarization is clearly more reasonable and it is thus the mechanism here proposed for the observed phenomenon in $Bi_2Ti_2O_7$.

It is well known that the electrode-dielectric interface can also lead to electrode polarization relaxation processes. Therefore, in order to verify this possibility (i.e. interaction between the electrodes and the sample), three different electrodes were used for the dielectric analysis, silver paste, platinum ink and gold (sputter coated). In all three cases the same dielectric response was obtained (Figure 5-1B). In addition, current-voltage tests revealed similar curves with a near linear behavior of positive slope with increasing voltage that rules out the possibility of Schottky barriers.^{78,79}

A high temperature (400-600K) analysis of the dielectric permittivity and loss was carried out to investigate the possibility of a high temperature dielectric relaxation event with the results shown in Figure 5-4. X-ray diffraction was performed before and after

the high temperature tests and verified that $\text{Bi}_2\text{Ti}_2\text{O}_7$ did not undergo a phase change during testing.

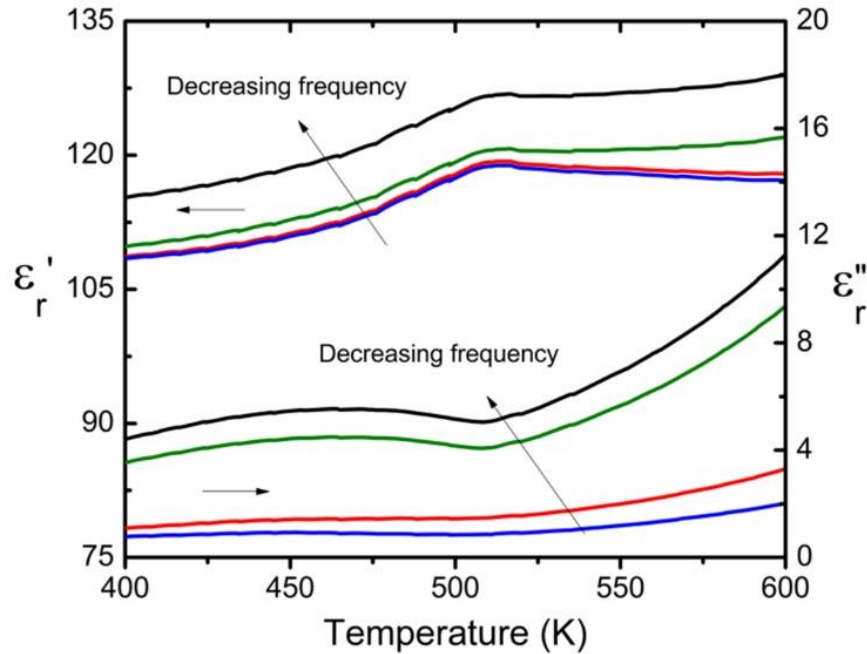


Figure 5-4. Imaginary and real part of the dielectric permittivity as a function of temperature at 80, 100, 500 and 1000 kHz.

No sign of relaxation was found in the imaginary part; however, there is a clear change in the relative permittivity around 512 K (as mentioned before, there are no noticeable features in the calorimetry data at this temperature). It is noteworthy that at 1 MHz the loss tangent ($\tan \delta$) goes from 0.0053 at room temperature to only 0.0097 at 546 K, and finally to 0.0317 at 646 K where conductivity is evident. Furthermore, the dielectric permittivity ranges from 113.59 at room temperature to 122.85 at 646 K.

5.2.2 Dielectric analysis as a function of frequency

Frequency dependent properties of materials are commonly described using 4 main form factors: the complex permittivity (ϵ), complex impedance (Z), complex admittance (Y), and complex modulus function (M). These functions are related as follows:

$$\varepsilon^* = \varepsilon' + j\varepsilon'' \quad (5-2)$$

$$M^* = M' + jM'' = \varepsilon^{-1} \quad (5-3)$$

$$Z^* = Z' + jZ'' = \mu^{-1} \varepsilon^{-1} \quad (5-4)$$

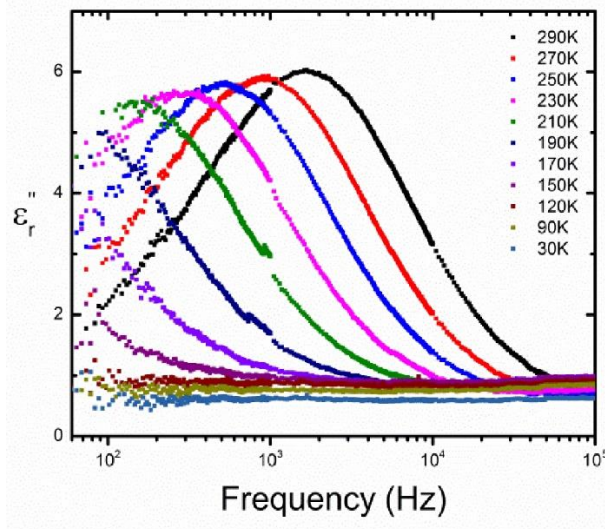
$$Y^* = Y' + jY'' = \mu\varepsilon \quad (5-5)$$

where $\mu = j\omega C_c$, ω is the angular frequency ($\omega = 2\pi f$), C_c is the geometric capacitance and $j = \sqrt{-1}$.⁸⁰ When a single relaxation process is occurring the dielectric response can be modeled by various relaxation models including the Debye relaxation,⁴⁴ the Cole-Cole relaxation,⁸¹ the Davidson-Cole relaxation,⁸² and the Havriliak-Negami relaxation.⁸³

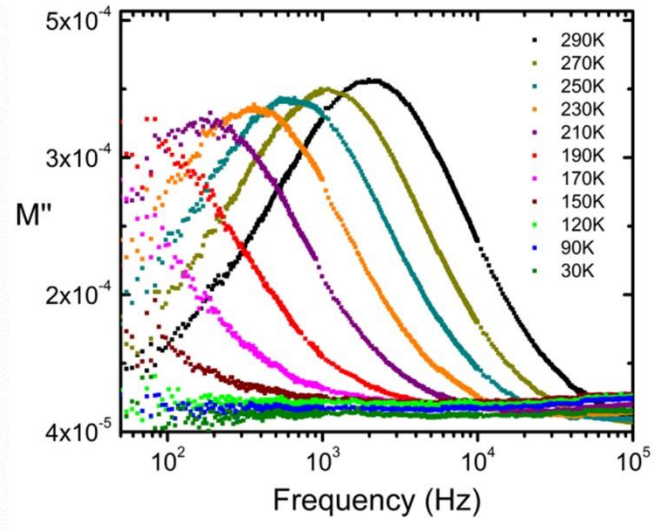
Using the relationships in Equations 5-2 – 5-5 and the relaxation model relationships, all of the dielectric functions will result in semicircles when plotted in the complex plane. However, depending on the strength of the relaxation not all of these features are experimentally observed.⁸⁴

As shown in the work by Cao and Gerhardt⁸⁵ conductivity will result in $\tau_M = \tau_Z$, where τ is the relaxation time of the specific dielectric function, therefore both the M'' and the Z'' peaks will overlap throughout the entire frequency range, thereby giving a clear indication that conductivity is occurring, $\text{Bi}_2\text{Ti}_2\text{O}_7$ does not exhibit this behavior. In Figure 5-5 the M'' displays a clear peak at 290K while Z'' does not over the same frequency range.

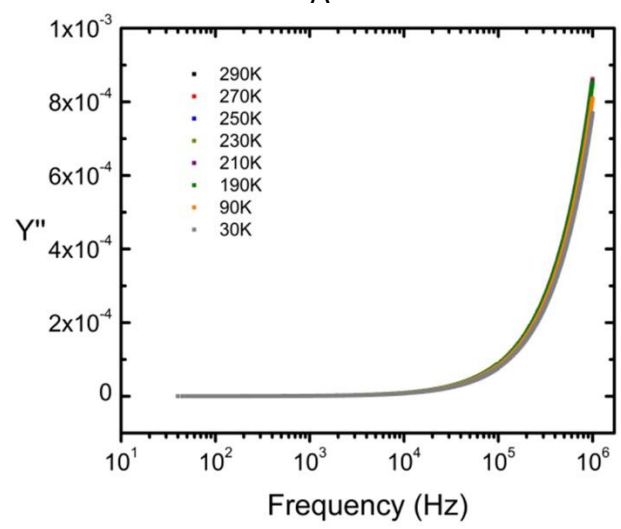
Due to the unusual nature of the dielectric response of $\text{Bi}_2\text{Ti}_2\text{O}_7$ one can attempt to differentiate conduction and relaxation using frequency dependent plots of the electric modulus, impedance, admittance, and dissipation factor ($\tan \delta$) shown in Figure 5-5.



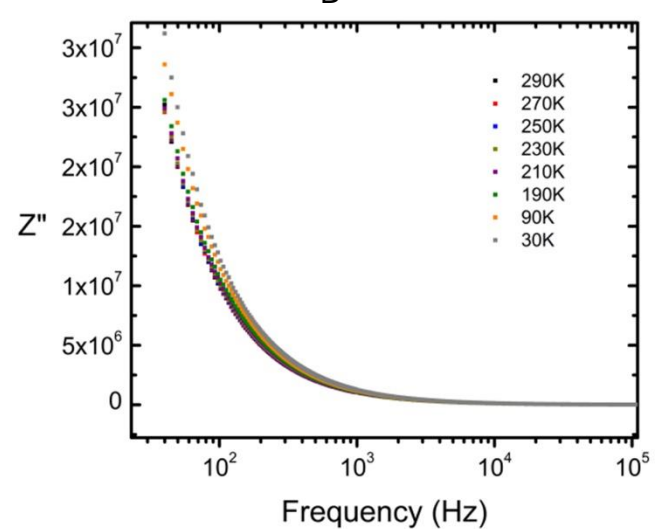
A



B



C



D

Figure 5-5. Frequency plots at varying temperatures of A) ϵ'' , B) M'' , C) Y'' , and D) Z''

The imaginary part of the permittivity is plotted (Figure 5-5A) as a function of frequency where it is evident that at temperatures below 150 K no clear dielectric loss peak is observed. Above 150 K, a peak in the dielectric loss becomes clearer, and by 290 K the ϵ'' plot displays the typical peak shape for relaxation fully contained in the frequency range plotted (Figure 5-6).

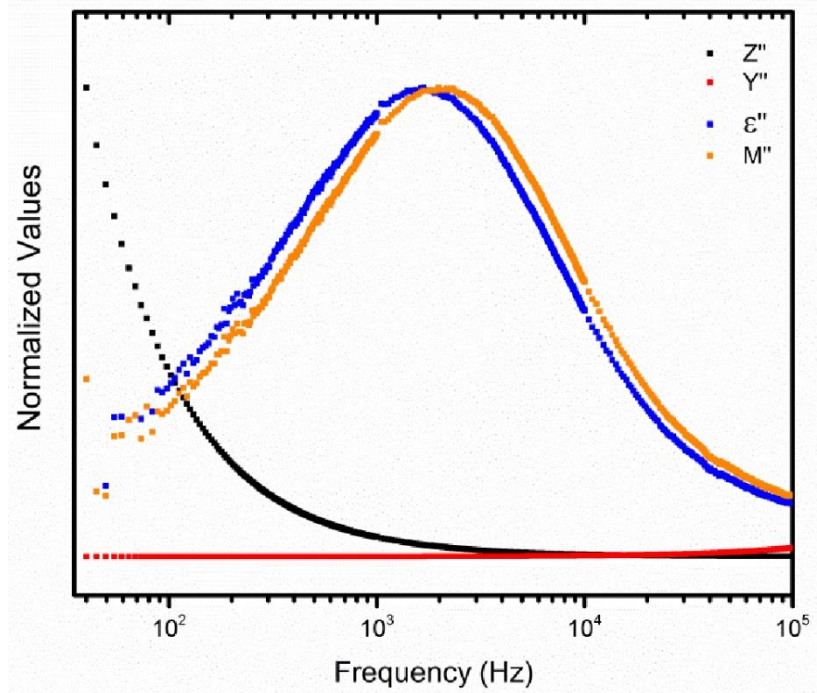


Figure 5-6. Normalized functions of Z'' , Y'' , M'' , and ϵ'' at 290 K.

Materials with small relaxation ratios ($r=\epsilon_s/\epsilon_\infty$) also exhibit two plateaus visible in the real part of the dielectric permittivity (ϵ_r') versus frequency plot as depicted in Figure 5-7 for $\text{Bi}_2\text{Ti}_2\text{O}_7$.

By analyzing the dielectric functions as a function of frequency it is clearly evident that a relaxation event is occurring in $\text{Bi}_2\text{Ti}_2\text{O}_7$. Both $\tan \delta$ and M'' display peaks at similar frequencies, while Y'' and Z'' do not. The real component of the dielectric permittivity also displays an increase in permittivity with two visible plateaus at temperatures greater than 200 K. This step-like increase in permittivity (ϵ_r') along with the peak behavior of ϵ'' prove that relaxation is occurring.⁸⁴ However, what makes $\text{Bi}_2\text{Ti}_2\text{O}_7$ different from a typical relaxor dielectric ceramic, such as BZN, is that the relaxation occurs at frequencies below 10^4 Hz which is generally ascribed to the space charge polarization mechanism.⁸⁶

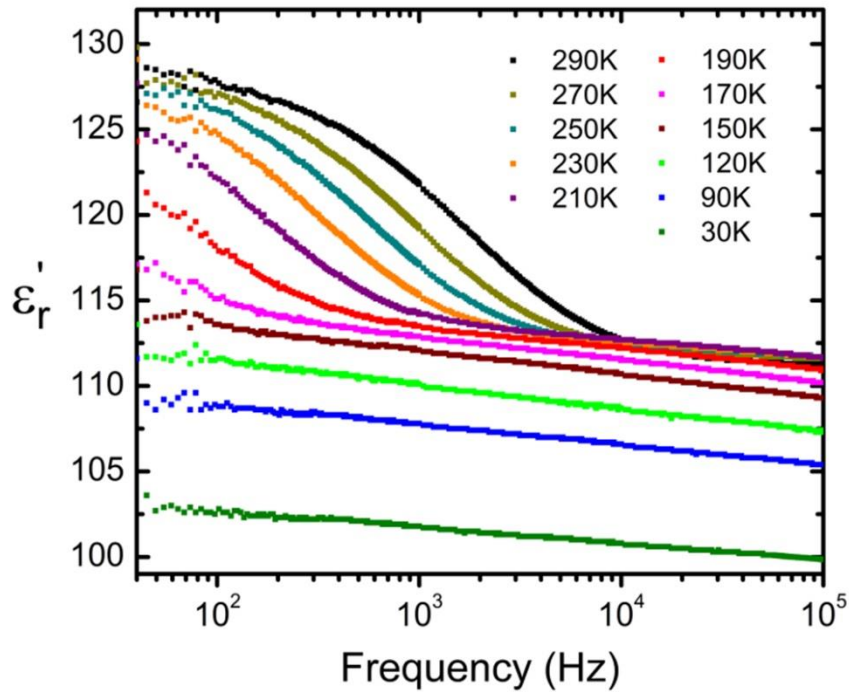


Figure 5-7. Frequency dependent plot of the real part of the dielectric permittivity.

So far it seems that the phenomenon is related to space charge polarization rather than dipolar or ionic as seen in BZN. As such, the dielectric study of $\text{Bi}_2\text{Ti}_2\text{O}_7$ makes it evident that chemical substitution affects the relaxation mechanisms of Bi-pyrochlores. For those with substitution on both sites (A and B) similar activation energies and characteristic frequencies have been calculated from the Arrhenius Equation (0.112-0.259 eV and 10^{12} - 10^{15} Hz^{22,45,72,87,88}); nevertheless, pyrochlores with substitution only on the B site show different values than the previous group (0.319-0.559 eV and 10^{16} - 10^{20} Hz^{21,23}). The values for the attempt jump frequencies for these compounds are clearly unrealistic and thus the authors had to use fitting models with less or no physical meaning to describe the dielectric behavior.

By contrast, bismuth titanate, a compound without chemical substitution (substitutional disorder), has an activation energy that fits well in the first group,

nonetheless, ν_0 differs orders of magnitude than any other Bi-pyrochlore and thus it cannot be considered an equivalent (dipolar) dielectric relaxation.

Further, as stated before, the recent observation of dielectric relaxation in the Ca-Ti-(Nb,Ta)-O pyrochlores⁸⁹ discards the presence of lone pair electrons or highly polarizable cations such as Bi^{3+} as necessary conditions for the emergence of the phenomenon. Nevertheless, atomic displacements and substitutional cations are present in those Ca-pyrochlores. Remarkably, in this work the dielectric analysis of $\text{Bi}_2\text{Ti}_2\text{O}_7$ has revealed that combined atomic displacements and high polarizability of the A-site are not enough to lead to the onset of dielectric relaxation, consistent with dipolar or ionic mechanism as seen in Bi-pyrochlores. This result in combination with the observations in Ca-pyrochlores suggests that substitutional cations play an essential role in the emergence of relaxation behavior in these compounds.

5.3 Dielectric properties of the $(\text{Sm}_x\text{Yb}_{1-x})_2\text{Ti}_2\text{O}_7$ and $\text{Sm}_2(\text{Sn}_x\text{Ti}_{1-x})_2\text{O}_7$ system

Dielectric characterization of $\text{Bi}_2\text{Ti}_2\text{O}_7$ showed that substitutional cations play an essential role in the emergence of dielectric relaxation in pyrochlores. In order to isolate the effect of substitutional cations on dielectric relaxation $(\text{Sm}_x\text{Yb}_{1-x})_2\text{Ti}_2\text{O}_7$ and $\text{Sm}_2(\text{Sn}_x\text{Ti}_{1-x})_2\text{O}_7$ ($x = 0.25, 0.5, 0.75$) were synthesized. Chapter 4 showed that both systems do not have atomic displacements, therefore only the effects of A-site and B-site substitution will be studied in order to better understand the nature of the dielectric phenomenon observed in pyrochlores.

5.3.1 Dielectric analysis of $(\text{Sm}_x\text{Yb}_{1-x})_2\text{Ti}_2\text{O}_7$ ($x = 0.25, 0.5, 0.75$)

Dielectric measurements were performed on the $(\text{Sm}_x\text{Yb}_{1-x})_2\text{Ti}_2\text{O}_7$ ($x = 0.25, 0.5, 0.75$) system in order to investigate the effect of substitution on the A-site without atomic displacements. The measured relative permittivity at 1MHz and 25°C ranges from 54.3-

59.8, with increasing x , while $\tan\delta$ (dielectric loss) ranged from 0.00045-0.00018. The obtained dielectric permittivity is lower than the value of $\text{Bi}_2\text{Ti}_2\text{O}_7$ but this can be attributed to the lack of a highly polarizable A-cation such as Bi^{3+} . As the Yb content decreased the permittivity increased, due to the higher polarizability of Sm, while the loss values stayed constant throughout ~ 0.1 . The values for the real and the imaginary parts of the dielectric permittivity as a function of temperature and fixed frequency of $(\text{Sm}_x\text{Yb}_{1-x})_2\text{Ti}_2\text{O}_7$ ($x = 0.25, 0.5, 0.75$) are illustrated in Figure 5-7A-C.

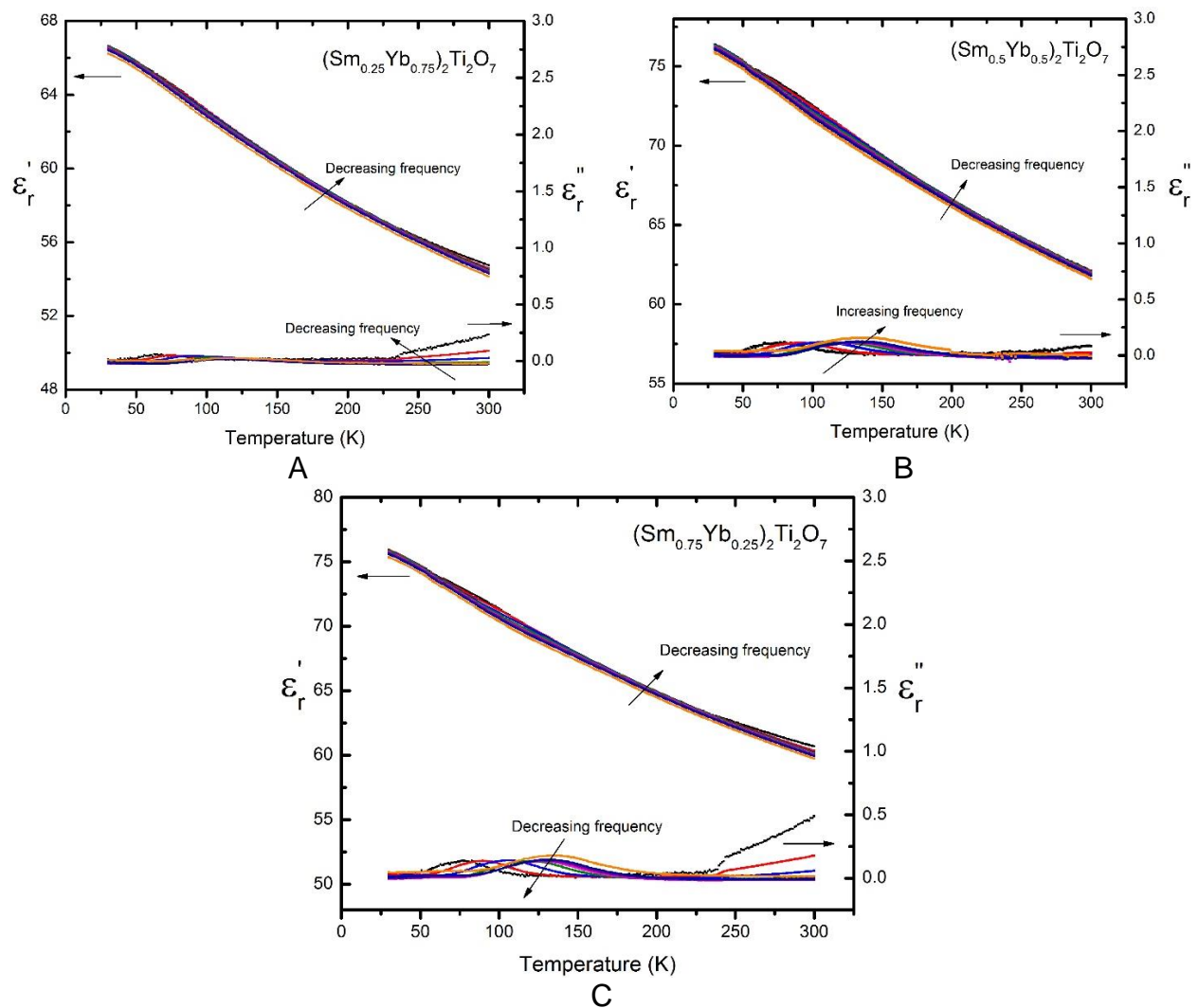


Figure 5-8. Imaginary and real part of the dielectric permittivity as a function of temperature from 10kHz to 2 Mhz of A) $(\text{Sm}_{0.25}\text{Yb}_{0.75})_2\text{Ti}_2\text{O}_7$ B) $(\text{Sm}_{0.50}\text{Yb}_{0.50})_2\text{Ti}_2\text{O}_7$ and C) $(\text{Sm}_{0.75}\text{Yb}_{0.25})_2\text{Ti}_2\text{O}_7$

The $(\text{Sm}_x\text{Yb}_{1-x})_2\text{Ti}_2\text{O}_7$ compounds all have a similar dielectric response; the permittivity increases as temperature decreases and the loss remains relatively constant throughout the whole temperature range. $(\text{Sm}_x\text{Yb}_{1-x})_2\text{Ti}_2\text{O}_7$ compounds do not exhibit the typical Bi-relaxation behavior seen in BZN and other Bi-pyrochlores. Therefore atomic substitution on the A-site without atomic displacements is not sufficient for dielectric relaxation in pyrochlores.

5.3.2 Dielectric analysis of $\text{Sm}_2(\text{Sn}_{0.5}\text{Ti}_{0.5})_2\text{O}_7$

Dielectric measurements were performed on $\text{Sm}_2(\text{Sn}_{0.5}\text{Ti}_{0.5})_2\text{O}_7$ in order to investigate the effect of substitution on the B-site without atomic displacements. The measured relative permittivity at 1MHz and 25°C was 36.73 while $\tan\delta$ (dielectric loss) was 0.00249. The obtained dielectric permittivity is lower than the value of $\text{Bi}_2\text{Ti}_2\text{O}_7$ but this can be attributed to the lack of a highly polarizable A-cation such as Bi^{3+} . The values for the real and imaginary parts of the dielectric permittivity as a function of temperature and fixed frequency are shown in Figure 5-8.

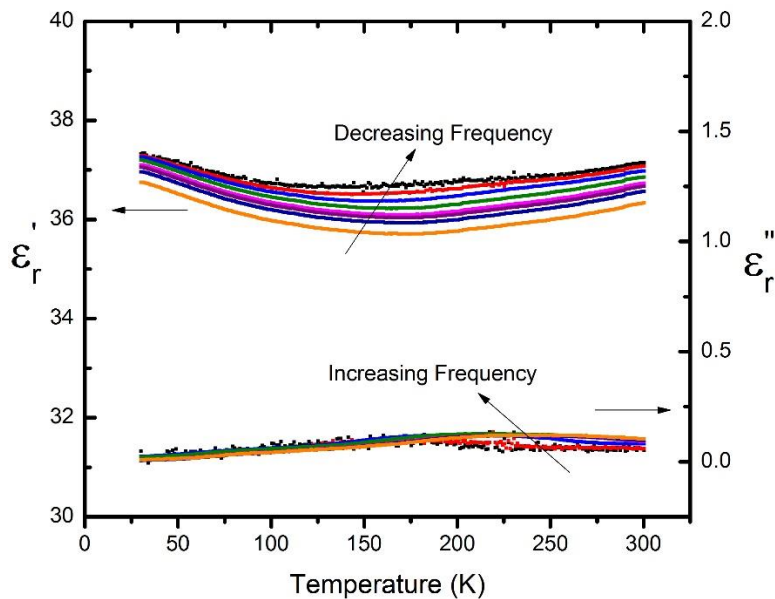


Figure 5-9. Imaginary and real part of the dielectric permittivity as a function of temperature from 10 kHz to 2MHz of $\text{Sm}_2(\text{Sn}_{0.5}\text{Ti}_{0.5})\text{O}_7$.

$\text{Sm}_2(\text{Sn}_{0.5}\text{Ti}_{0.5})_2\text{O}_7$ does not exhibit the typical pyrochlore dielectric relaxation response. Instead, $\text{Sm}_2(\text{Sn}_{0.5}\text{Ti}_{0.5})_2\text{O}_7$ the permittivity remains relatively constant as temperature decreases and the loss remains relatively constant throughout the whole temperature range. Therefore atomic substitution on the B-site without atomic displacements is not sufficient for dielectric relaxation in pyrochlores.

5.4 Conclusion

A dielectric analysis of $\text{Bi}_2\text{Ti}_2\text{O}_7$ ceramic, a bismuth pyrochlore without substitutional disorder, revealed considerable differences with respect to the common dielectric behavior exhibited by this family of compounds. The dielectric relaxation observed in BZN is absent in $\text{Bi}_2\text{Ti}_2\text{O}_7$; however, a relaxation of a different nature was found at low frequencies (<10 kHz) and at relatively high temperature (125 K) in $\text{Bi}_2\text{Ti}_2\text{O}_7$. The calculated activation energy and characteristic frequency of this behavior using the Arrhenius model were 0.162 eV and ~1 MHz, respectively. The low attempt jump frequency is consistent with space charge polarization and not the result of dipolar or ionic disorder. The relaxation behavior at low frequency was confirmed with a study of the electrical modulus, $\tan \delta$, admittance, and impedance as a function of frequency. The atypical dielectric response of $\text{Bi}_2\text{Ti}_2\text{O}_7$ suggests that substitutional cations (rather than ionic displacements, or lone pair electrons), play a major role in the origin of the dielectric relaxation in pyrochlores.

A dielectric analysis of the $(\text{Sm}_x\text{Yb}_{1-x})_2\text{Ti}_2\text{O}_7$ and $\text{Sm}_2(\text{Sn}_x\text{Ti}_{1-x})_2\text{O}_7$ ($x = 0.25, 0.5, 0.75$) systems, pyrochlores without atomic displacements, revealed no evidence of dielectric relaxation to that observed in BZN. These responses suggest that substitutional cations on their own are not sufficient to induce dielectric relaxation in pyrochlores.

CHAPTER 6
RAMAN AND IR PROPERTIES OF $\text{Bi}_2\text{Ti}_2\text{O}_7$

6.1 Introduction

Recall from Chapter 2 that in the ideal pyrochlore structure ($\text{A}_2\text{B}_2\text{O}_7$, $Fd\bar{3}m$ space group, origin 1), the A cation resides at the 16c site, the B cation at the 16d site, O at the 48f site, and the seventh oxygen, typically denoted as O', at the 8a position. However, density-functional theory (DFT) calculations by Esquivel-Elizondo *et al.*²⁶ indicate that the atoms within the $\text{Bi}_2\text{Ti}_2\text{O}_7$ crystal do not reside at the ideal pyrochlore positions. Rather, in $\text{Bi}_2\text{Ti}_2\text{O}_7$, the A cation (bismuth) is not located in its ideal 16c (0,0,0) but is in the 96g (0.015, 0.015, 0.964) site. The O' atom is also not in the ideal pyrochlore position: instead of residing in the 8a site (1/8, 1/8, 1/8), it is displaced to the 48f (x , 1/8, 1/8) position.

Furthermore, a noteworthy feature of the theoretical (DFT) study is a large isotropic thermal parameter ascribed to the Ti cation in the 16d position.²⁶ This was reported to be the result of the displacement of the bismuth atom towards the 96g site which in turn causes a separation between the regularly symmetric Bi and O atoms, thus resulting in an under-coordinated Ti atom. In an effort to satisfy this O under-coordination the Ti cation is predicted by DFT calculations to displace to the 96g position.

To reconcile this rather unprecedented prediction, it is important to recognize that DFT calculations do not take into account thermal considerations (since calculations are performed at 0 K) and that experimental diffraction (X-ray and neutron⁹⁰) experiments to date have not yielded evidence of Ti shifting from the 16d position to the 96g.

Therefore, in the past, a large thermal isotropic parameter has been ascribed to the Ti cation instead of reporting a displacement towards 96g positions.

Table 6-1. Optical modes for Bi₂Ti₂O₇

O_7^h	Distribution of Degrees of Freedom				Acoustic Modes	Optical Modes	Selection Rules
	Bi	Ti	O	O'			
	C_s	D_{3d}	C_{2v}	C_{2v}			
	96g	16d	48f	48f			
A _{1g}	2	0	1	1	0	4	Raman
A _{1u}	1	0	0	0	0	1	Silent
A _{2g}	1	0	0	0	0	1	Silent
A _{2u}	2	1	1	1	0	5	Silent
E _u	3	1	1	1	0	6	Silent
E _g	3	0	1	1	0	5	Raman
F _{1g}	4	0	2	2	0	8	Silent
F _{2g}	5	0	3	3	0	11	Raman
F _{1u}	5	2	3	3	1	12	Infrared
F _{2u}	4	1	2	2	0	9	Silent

4A_{1g}(R)+A_u(-)+A_{2g}(-)+5A_{2u}(-)+6E_u(-)+5E_g(R)+8F_{1g}(-)+12F_{1u}(IR)+11F_{2g}(R)+9F_{2u}(-)

The proposed atomic displacements of the Bi and O' atoms in Bi₂Ti₂O₇ are similar to those observed in another bismuth pyrochlore, Bi_{1.5}Zn_{0.92}Nb_{1.5}O_{6.92} (BZN).¹⁻³ Nonetheless, what is striking is that this displacement would occur without atomic substitutional atoms (e.g. Bi, and Zn in the A-site) and multiple site occupancy (e.g. Zn in both A- and B-sites, both of which are always present in BZN and related pyrochlores).

To understand further the implication of the atomic displacements on the local atomic structure and predicted phonons, Table 6-1 displays the factor group analysis for

Bi₂Ti₂O₇ following the DFT positions by Esquivel-Elizondo *et al.*²⁶ The irreducible representation (Γ) was derived using the normal mode determination tables.⁵¹ Using Schönflies notation, the space group for Bi₂Ti₂O₇ is O_7^h ; bismuth has a C_s point group symmetry representing a cyclic point group with a two-fold rotation, while titanium has a dihedral D_{3d} point group symmetry with a three-fold rotation and 3 two-fold axes perpendicular to the three-fold axis and a horizontal mirror plane. Both O and O' are represented by the point group symmetry C_{2v} which is a cyclic group with a two-fold rotation and 2 vertical planes.

Recalling that in the ideal pyrochlore structure the factor group analysis yields⁹¹:

$$3A_{2u}+3E_u+A_{1g}(\mathbf{R})+E_g(\mathbf{R})+4F_{2g}(\mathbf{R})+8F_{1u}(\mathbf{IR})+4F_{2u}+2F_{1g}. \quad (6-1)$$

In the proposed Bi₂Ti₂O₇ structure the anticipated modes, following normal coordinate analysis methods, are:

$$4A_{1g}(\mathbf{R})+A_u+A_{2g}+5A_{2u}+6E_u+5E_g(\mathbf{R})+8F_{1g}+12F_{1u}(\mathbf{IR})+11F_{2g}(\mathbf{R})+9F_{2u}. \quad (6-2)$$

When compared to the ideal pyrochlore structure, one can expect more F_{1u} infrared-active (IR) modes to appear in the spectra. It is also important to note that in both Equation 5-1 and Equation 5-2 the acoustic mode has been subtracted from the total number of vibrational modes. Furthermore, it has also been proposed by Chen *et al.*⁹² that disorder in the A site leads to a break in the selection rules and, therefore, the normally IR active low frequency modes, such as F_{1u} , may also appear in the Raman spectra.

Atomic (valence) force field analysis allows for the identification of the type of interactions that contribute to each phonon mode. It also provides an insight into the structure of a cell by comparison with similar crystals, such that atomic disorder can be discerned. This has been previously demonstrated for pyrochlores by Vandenborre *et*

*al.*⁹³ and applied to perform a detailed comparison across a series of titanate and stannate pyrochlores.

Based on this, Raman and IR spectroscopy techniques are used to gain insight into the nature and characteristics of the local structure of $\text{Bi}_2\text{Ti}_2\text{O}_7$ and corroborate the crystallographic and computational studies performed in Chapter 4 on the crystal structure of $\text{Bi}_2\text{Ti}_2\text{O}_7$ in particular as it relates to its non-correlated atomic displacements.⁹⁴

6.2 Raman Spectroscopy

As discussed at length by Esquivel-Elizondo *et al.*²⁶ $\text{Bi}_2\text{Ti}_2\text{O}_7$ can be considered a metastable compound, with dissociation into $\text{Bi}_4\text{Ti}_3\text{O}_{12}$ and $\text{Bi}_2\text{Ti}_4\text{O}_{11}$ commonly occurring. This crystal chemistry had previously prevented the synthesis of $\text{Bi}_2\text{Ti}_2\text{O}_7$ sintered ceramics until fast firing technique like microwave sintering were used. Because Raman spectroscopy provides the capability to measure the spectra of samples that are sintered solids, powders, or even particulates suspended in a fluid, it is an excellent tool for characterizing whether a material undergoes a structural transformation when sintered or processed. Therefore, spectra of $\text{Bi}_2\text{Ti}_2\text{O}_7$ were taken in both powder and solid pellet form. These spectra, shown in Figure 6-1, were identical for the powder and pellet samples, further confirming that sintering of $\text{Bi}_2\text{Ti}_2\text{O}_7$ powder does not induce a structural change, in agreement with X-ray diffraction results.²⁶ This lends further evidence in favor of the modified phase diagram,²⁶ which establishes the appearance of the pyrochlore phase in the $\text{Bi}_2\text{O}_3\text{-TiO}_2$ system.

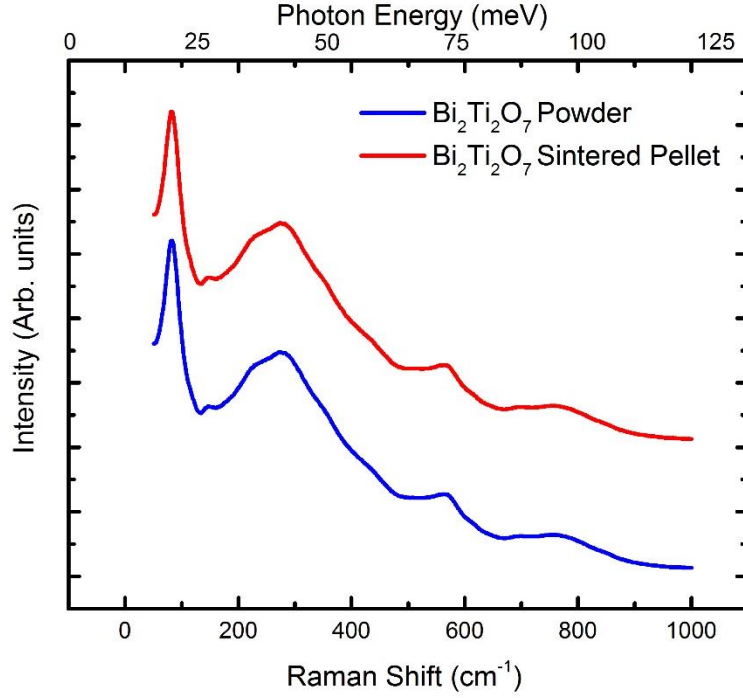


Figure 6-1. Room temperature Raman spectra of Bi₂Ti₂O₇ powder and sintered pellet.

The Bi₂Ti₂O₇ Raman spectrum was analyzed by solving for the imaginary part of the Raman susceptibility in order to observe and fit the individual vibrational modes. This was accomplished through the transformation of the measured data to find the imaginary part of the Raman susceptibility, $\chi''(\omega)$.⁹⁵ The susceptibility is a function of the Raman scattering cross section and the Bose scattering factor. This was resolved by treating the collected data with the Bose-Einstein distribution, $n(\omega)$.

$$n(\omega) = \frac{1}{e^{\hbar\omega/k_B T} - 1} \quad (6-3)$$

The transformed Raman susceptibility was modeled using a sum of Lorentzian functions used to assign the Raman modes, as shown in Figure 5-2.

$$\chi''(\omega) = \sum_j^n \frac{A_j}{1 + \frac{4(\omega - \omega_{oj})^2}{\gamma_j^2}} \quad (6-4)$$

where each fitted peak is characterized by a center frequency ω_o , a local maximum A_j , and a width γ_j .

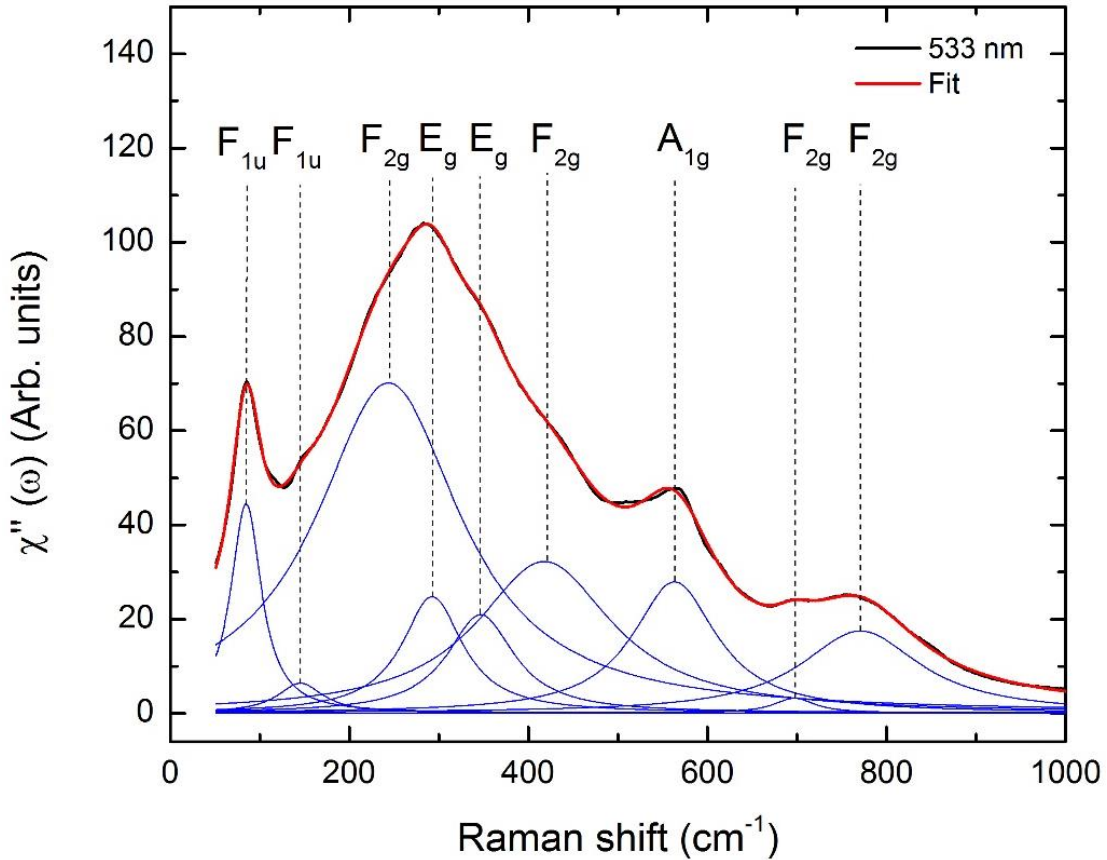


Figure 6-2. Raman spectra transformed by the Bose-Einstein factor. The obtained imaginary part of the Raman susceptibility was fitted to a sum of Lorentzian functions. The figure shows the data (black), the fit (red), and the individual contributions to the fit (blue).

This functional form is attributed to samples with homogenous broadening, where the width of the Raman band is related to the damping coefficient γ_j . The other functional form is that of Gaussians:

$$\chi''(\omega) = C + \sum_j^n I_{0j} e^{-(\omega - \omega_{0j})^2 / \sigma_j^2} \quad (6-5)$$

where I_o , ω_{oj} , and σ_j are the height, center frequency, and the statistical width of each band, and C is a constant. The Gaussian functional form is used for inhomogeneous broadening where the width of each band is due to a statistical distribution of the resonant frequency ω_{oj} . The results of the Gaussian fit are shown in Figure 6-3.

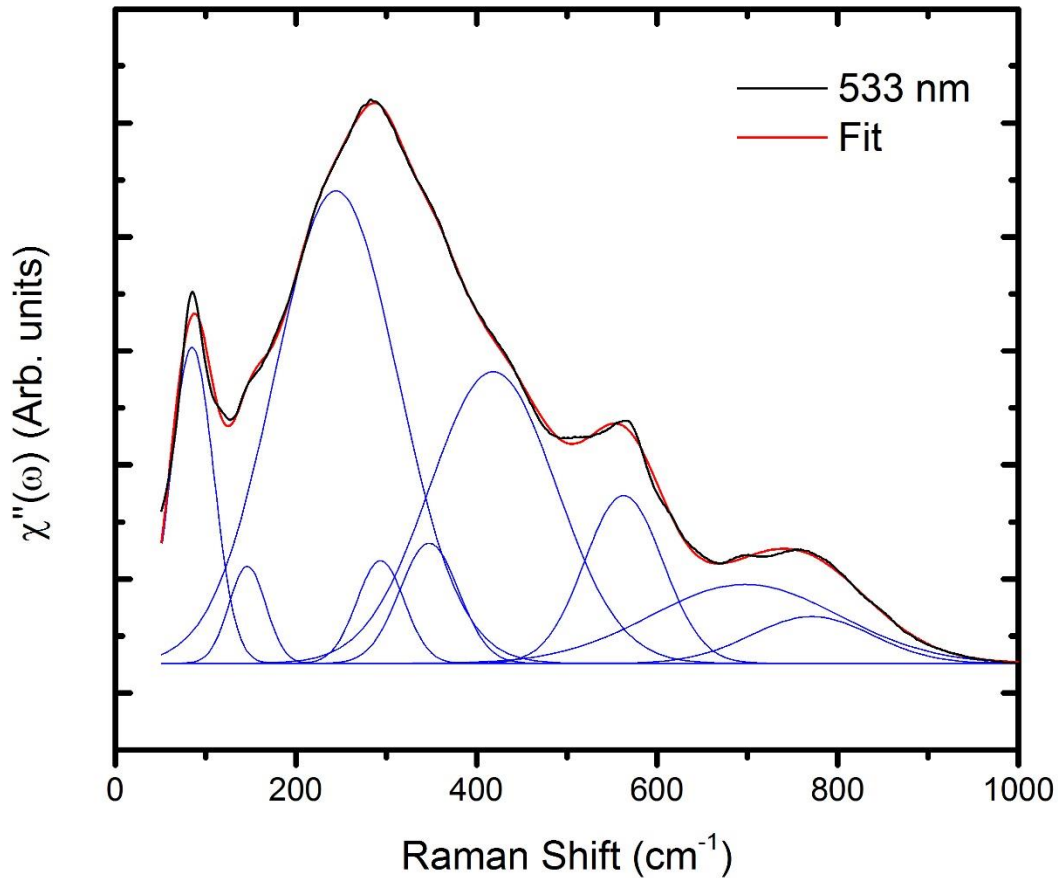


Figure 6-3. Raman spectra transformed by the Bose-Einstein factor. The obtained imaginary part of the Raman susceptibility was fitted to a sum of Gaussian functions. The figure shows the data (black), the fit (red), and the individual contributions to the fit (blue).

Table 6-2 shows parameters obtained from the Lorentzian fitting. The $\text{Bi}_2\text{Ti}_2\text{O}_7$ modes were assigned by comparing to typical bismuth and titanate pyrochlores⁹⁵⁻⁹⁷ as shown in Table 6-2, but with the addition of normally infrared active F_{1u} . Because the area of each fitted mode is an arbitrary value (hence the representation by integrated

intensity), the error presented is the calculated standard error of each mode represented as the fraction of each peak's total area.

Table 6-2. Parameters for Bi₂Ti₂O₇ in the Lorentzian fitting of the Raman spectra.

Integrated intensity (arb. u.)	ω_{oj} (cm ⁻¹)	γ_j (cm ⁻¹)	Assignment	Type	Error
13	85	41	F _{1u}	O-A-O bend &	2%
3	146	62	F _{1u}	O-A-O' bend	15%
100	244	197	F _{2g}	Bi-O stretch & O-Bi-O' bend	6%
15	293	83	E _g		20%
14	347	92	E _g	Ti-O stretch	2%
43	418	185	F _{2g}		17%
23	563	114	A _{1g}	O-Ti-O bend	3%
1	697	55	F _{2g}		8%
21	771	163	F _{2g}	Ti-O stretch	17%

Through the automated Lorentzian fit algorithm, nine optically active Raman vibrational modes were identified. These nine peaks each represent an interaction (bend, stretch, breathing, etc.) within the local bonding environment between oxygen atoms and Bi or Ti atoms. The Raman-mode properties are a function of the force field emitted by each atom and each corresponding bond's interaction with the Raman photon.

While each peak is assigned to a main photon mode and motion in Figure 6-2 and Table 6-2 it is also true that that when one bond is set into vibration, this motion has an effect on the rest of the lattice; *i.e.*, when a bending occurs between one bond species, the other atomic bonds in the structure will bend and stretch in reaction. This combined set of phonon motions have been clearly shown for the pyrochlore structure, by Vandenberg *et al.* It has been observed that palatinates and stannates display sharp peaks in the spectra, much more than the zirconates, hafnates and titanates. This difference is explained by a greater deviation from ideal pyrochlore symmetry (D_{3d}) in the latter compounds.⁹¹ As such, materials with high degree of non-correlated atomic

displacements will typically exhibit broad peaks within the Raman spectra. Therefore, here we propose that the relatively broadening of the Raman peaks observed is the result of the atomic position displacement causing local asymmetry within the crystal that produces a stronger force field reaction from a single phonon interaction.

In previous studies of pyrochlore titanates¹⁸, valence force field constants for stretch, bend, and combination bend-stretch interactions have been calculated for a variety of compounds. The potential energy of each mode is dependent on the sum of the strength of each contributing interaction, namely how the strength of the valence force and the incoming photon cause a series of singular or multiple elastic interaction throughout the lattice. Low frequency Raman modes found in pyrochlores are generally found to be a combination of several bends and stretches, as photon interactions on the lattice due to single bends/stretchers induce elastic effects at other sites. Calculation of individual interaction valence force fields in $\text{Bi}_2\text{Ti}_2\text{O}_7$ is beyond the scope of this work; however, based on the trends observed in other pyrochlores, we postulate that modes fitted to large and wide Lorentzian indicate that the interaction causing the vibration arises from a combination of several motions, each contributing an additional amount of energy into the vibration. For example, the F_{2g} mode centered at 244 cm^{-1} has a width of 197 cm^{-1} which is attributed to the combination of the Bi-O stretch and the O-Bi-O' bend motions. Likewise, sharper peaks indicate that a vibrational mode is primarily influenced by a single interaction.

It is important to note that previous work on the theoretical $\text{Bi}_2\text{Ti}_2\text{O}_7$ structure and vibrational spectra was performed by Patterson through DFT.⁹⁸ The DFT calculations performed by Patterson were performed for $\text{Bi}_2\text{Ti}_2\text{O}_7$ in both the $Pna2_1$ and $Fd\bar{3}m$ crystal

structures. However, both structural studies and the data presented in this paper confirm that $\text{Bi}_2\text{Ti}_2\text{O}_7$ has a cubic $Fd\bar{3}m$ structure. Although the Bi ion displacement was included in these DFT calculations, the theoretical Raman spectra did not predict the Raman active F_{1u} modes observed in this work.

To reconcile this, it is worth mentioning that in general, pyrochlores have their A-O atom interactions dominant at low frequencies and their B-O atom interactions prevalent and at high frequencies. The low-frequency range of the Raman spectrum (from 70–180 cm^{-1}) has been proposed to be composed of typically IR-active F_{1u} vibrational modes due to the non-correlated atomic displacements of the A site observed in Bi pyrochlores.⁹⁵ In a study of Sm, Gd, Yb, and Y titanate pyrochlores by Vandenberg¹⁸, Raman spectra comparison of low frequency modes were determined to not be fundamental frequencies, and were attributed to TiO_6 octahedra distortion and/or displacement in the A-site cation. The F_{1u} modes activated primarily due to the O-A-O and O-A-O' bending, assigned at 85 and 145 cm^{-1} , similarly occur in the Raman spectra of $\text{Bi}_2\text{Ti}_2\text{O}_7$ due to the displacement of the Bi atom from a high-symmetry position in the crystal lattice.⁹⁵

As stated before, the Bi atom in $\text{Bi}_2\text{Ti}_2\text{O}_7$ differs from the ideal pyrochlore structure by occupying the 96g Wyckoff position instead of the 16c. This non-correlated atomic displacements in $\text{Bi}_2\text{Ti}_2\text{O}_7$ further supports the idea proposed by Arenas *et al.*⁹⁵ of a relaxation in the selection rules allowing for the F_{1u} mode to be seen in the Raman spectra.

Following this, the 180–500 cm^{-1} bands are composed of F_{2g} and E_g modes.⁹⁵ The first F_{2g} mode is generally assigned between 200–240 cm^{-1} for titanates,⁹⁶ and in

the case of $\text{Bi}_2\text{Ti}_2\text{O}_7$ the lowest F_{2g} is assigned to the mode observed at 242 cm^{-1} . This vibrational mode is attributed to a combination of a stretching interaction between the Bi-O bonds, which induces an additional bending in the O-Bi-O' bond. The E_g modes assigned to 294 and 347 cm^{-1} and the F_{2g} mode assigned at 419 cm^{-1} are mainly due to a stretching of the Ti-O bond which cause a reaction from other O-Ti-O bonds.

The higher frequencies consist of A_{1g} and F_{2g} vibrational modes, which are purely due to the Ti-O modes.⁹⁷ The lower A_{1g} mode, assigned at 564 cm^{-1} , is due to O-Ti-O bond bending. The two highest modes are designated as F_{2g} and are assigned at 697 and 771 cm^{-1} , and are entirely due to the stretching of the Ti-O bond.

Table 6-3 presents the vibrational modes of several pyrochlore titanates with their corresponding frequencies.

Table 6-3. The observed Raman vibrational mode frequencies of bismuth and titanate pyrochlores

		F_{2g} / E_g		F_{2g}	A_{1g}	F_{2g}	F_{2g}	
$\text{Y}_2\text{Ti}_2\text{O}_7$ ⁹³	225	--	318	333	--	527	531	586
$\text{Gd}_2\text{Ti}_2\text{O}_7$ ⁹⁹	205	260	310	325	450	517	554	677
$\text{Dy}_2\text{Ti}_2\text{O}_7$ ⁹⁹	212	269	308	328	451	519	550	693
$\text{Ho}_2\text{Ti}_2\text{O}_7$ ⁹⁹	214	297	311	329	452	522	562	701
$\text{Lu}_2\text{Ti}_2\text{O}_7$ ¹⁰⁰	188	--	313	336	458	520	609	712
Experimental $\text{Bi}_2\text{Ti}_2\text{O}_7$	--	244	293	347	418	563	697	771
Theoretical $\text{Bi}_2\text{Ti}_2\text{O}_7$ ⁹⁸	--	262	281	--	395	535	537	711
$\text{Bi}_{3/2}\text{MgNb}_{3/2}\text{O}_7$ ⁹⁵	--	230	346	--	419	511	599	786
$\text{Bi}_{3/2}\text{MgNb}_{3/2}\text{O}_7$ ⁹⁵	--	216	297	--	430	529	620	758
$\text{Bi}_{3/2}\text{Zn}_{0.92}\text{Nb}_{3/2}\text{O}_{6.92}$ ⁹⁵	--	256	342	--	420	526	610	766
$\text{Bi}_{3/2}\text{ZnTa}_{3/2}\text{O}_7$ ⁹⁵	--	208	281	--	434	540	624	744

The $\text{Bi}_2\text{Ti}_2\text{O}_7$ Raman modes follow the general behavior of the titanate pyrochlores up until the 500 cm^{-1} range, at which point the A_{1g} and F_{2g} modes are observed at notably higher frequencies, in disagreement with the theoretically calculated modes.⁹⁸ This can be explained by a possible disorder in the titanium position in the $\text{Bi}_2\text{Ti}_2\text{O}_7$ crystal structure, which would affect the Ti-O bond interactions,

and accordingly the A_{1g} and F_{2g} modes. Recalling the large isotropic parameter assigned to the Ti atom, the observed Raman spectra provide additional evidence suggesting that the Ti atom may in fact be locally displaced,²⁶ which would in turn affect Raman interactions.

6.3 Infrared Spectroscopy

6.3.1 Reflectance spectra

The temperature dependent reflectance of a sintered $\text{Bi}_2\text{Ti}_2\text{O}_7$ pellet over 30 and 37000 cm^{-1} is shown Figure 6-4. The high reflectance value seen at low frequencies is consistent with the large static permittivity values of $\text{Bi}_2\text{Ti}_2\text{O}_7$. As temperature changes, the spectra change only slightly, with a few percent increase at lower temperatures. We conclude that there is no phase transition present in this temperature range.

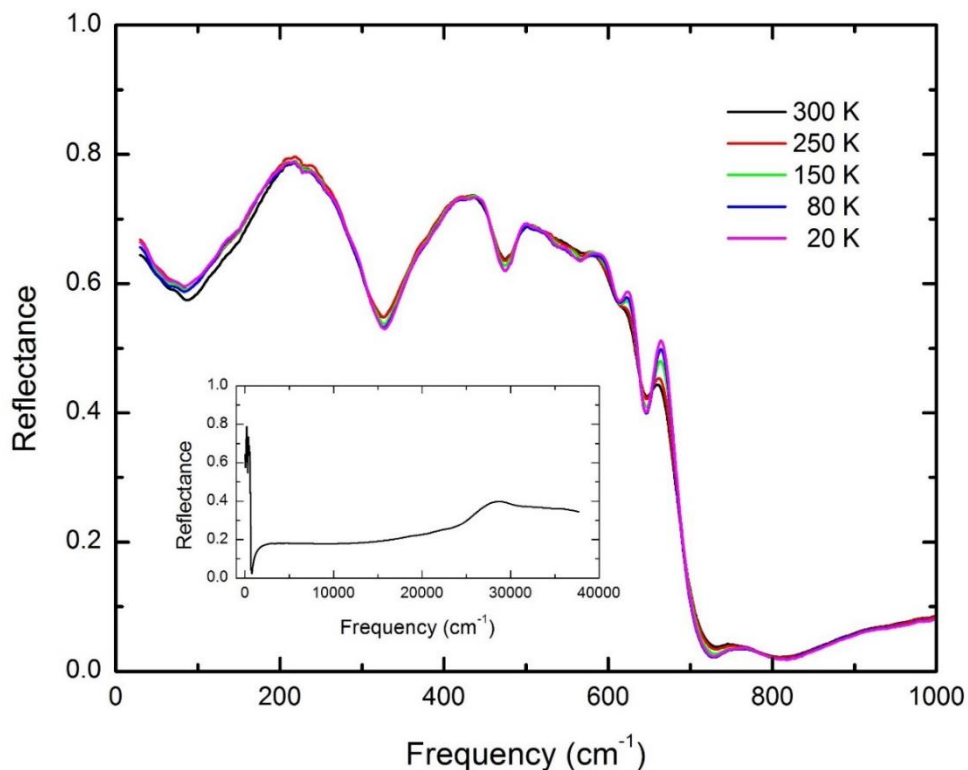


Figure 6-4. The reflectance of $\text{Bi}_2\text{Ti}_2\text{O}_7$ at temperatures between 20 and 300 K

6.2.2 Kramers-Kronig analysis

The frequency-dependent phase shift upon reflection can be calculated from the measured single bounce reflectivity via the Kramers-Kronig integral.¹⁰¹ The high frequency behavior of $\text{Bi}_2\text{Ti}_2\text{O}_7$ from 80,000 to 242,000,000 cm^{-1} (10–30,000 eV) is determined using scattering functions from Henke,¹⁰² and is based on the density and cubic structure of the pyrochlore. The behavior above this range is taken to follow free electron behavior, $R \sim \omega^{-4}$. The gap between the 37,000 cm^{-1} end to the measured reflectance and the start of the calculated X-ray data is bridged with a power law to the third degree in $1/\omega$. The low frequency extrapolation, covering 0 to 30 cm^{-1} uses the reflectance calculated from the oscillator model fit described in the next section. With the phase shift calculated from measured data using Kramers-Kronig methods, other optical constants, including the real and imaginary parts of the dielectric constant (Figures 6-5 and 6-6) and the optical conductivity (Figure 6-7), can be easily found.¹⁰¹

We note that the optical conductivity and permittivity plots show the widths of the phonons to be quite substantial. This, however, is not in disagreement with Chen *et al.*, who also found broad phonon spectra in Bismuth based pyrochlores.⁹² We can also see from the real part of the permittivity, that there is a weakening of the mode at 160 cm^{-1} with decreasing temperature. There is a corresponding softening of this peak in Figures 6-6 and 6-7. The interband electronic contribution to the optical conductivity can be clearly seen in the inset of Figure 6-6.

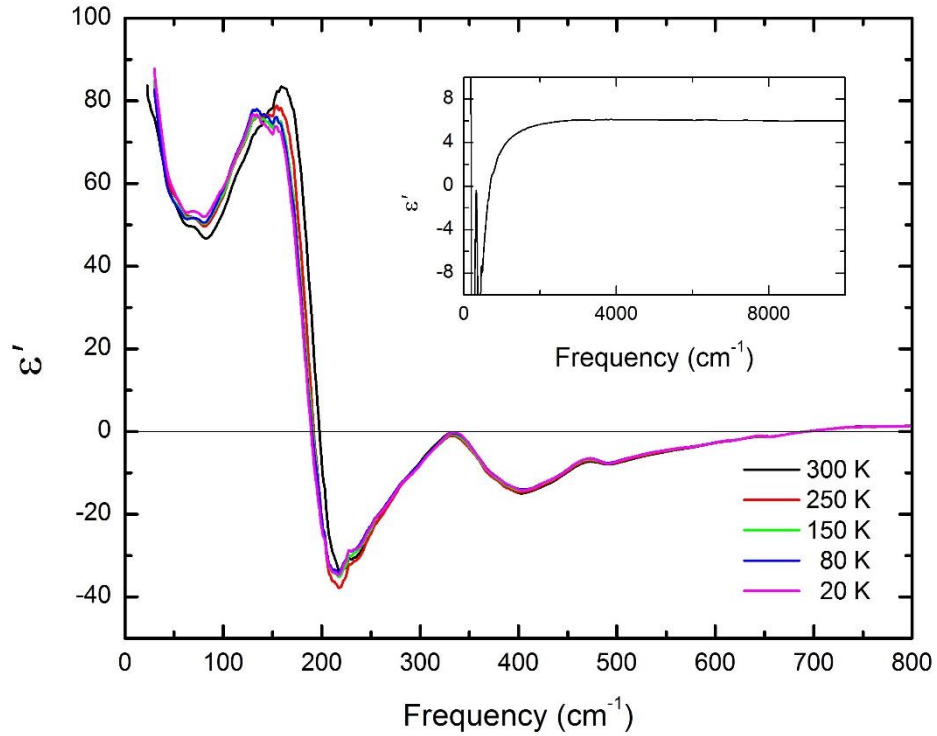


Figure 6-5. The real part of the dielectric function (ϵ') of $\text{Bi}_2\text{Ti}_2\text{O}_7$ at temperatures between 20 and 300K

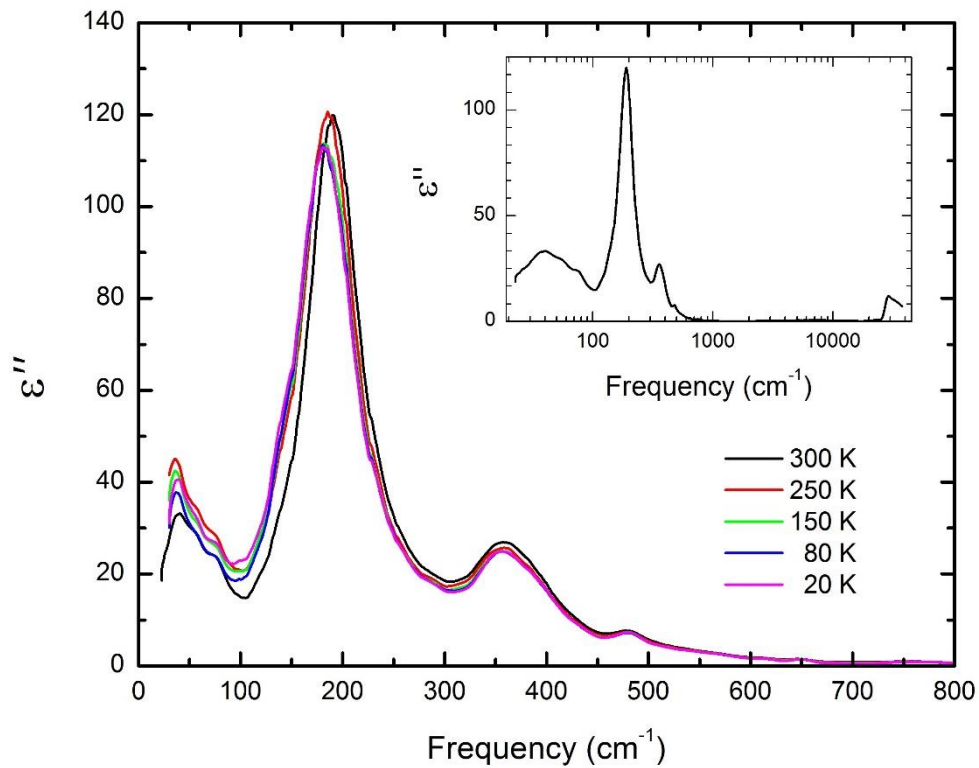


Figure 6-6. The imaginary part of the dielectric function (ϵ'') of $\text{Bi}_2\text{Ti}_2\text{O}_7$ at temperatures between 20 and 300 K.

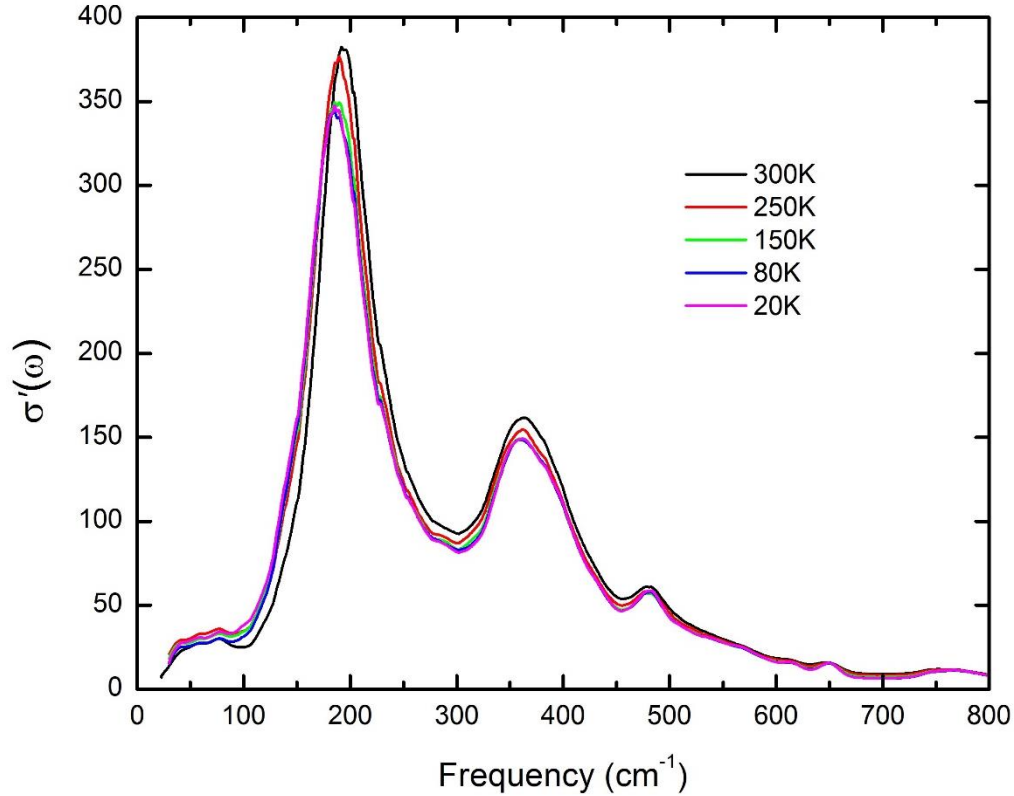


Figure 6-7. The real part of the optical conductivity (σ') of $\text{Bi}_2\text{Ti}_2\text{O}_7$ at temperatures between 20 and 300 K.

6.2.3 Oscillator-model analysis

To complement the Kramers-Kronig analysis and in order to assign the contribution to the permittivity from each mode, oscillator model fits were conducted on the measured reflectance. Oscillator fits of the experimental measurements are obtained by the dispersion analysis (DA) method, which solves for each oscillator based on its strength, width, and frequency. The DA method requires the crystal's reflectivity to be in agreement with the oscillators. To solve for the reflectance the Fresnel formula is employed.

$$R(\omega) = \frac{(n-1)^2 + k^2}{(n+1)^2 + k^2} \quad (6-4)$$

with $R(\omega)$ the reflectance, n the refractive index, and k the extinction coefficient of the material. In turn, n and k are related to the dielectric function ϵ via:

$$n + ik = \sqrt{\epsilon' + i\epsilon''} \quad (6-5)$$

with ϵ' and ϵ'' the real and imaginary parts of the dielectric function given as:

$$\epsilon' = n^2 - k^2 = \epsilon_\infty + \sum_j \frac{4\pi\rho_j\omega_j^2(\omega_j^2 - \omega^2)}{(\omega_j^2 - \omega^2)^2 + (\gamma_j\omega)^2} \quad (6-6)$$

$$\epsilon'' = 2nk = \sum_j \frac{4\pi\rho_j\omega_j^2(\gamma_j\omega)}{(\omega_j^2 - \omega^2)^2 + (\gamma_j\omega)^2} \quad (6-7)$$

Each oscillator is described by its strength ρ_j , width γ_j , and frequency ω_j .

As previously discussed, a factor group analysis that uses the displaced coordinates (albeit without Ti displacement, as shown in Table 6-1) yields a total of 12 allowable IR active modes. Here, 13 oscillators are required to fit the infrared reflectivity spectra for $\text{Bi}_2\text{Ti}_2\text{O}_7$. The parameters for these oscillators are presented in Table 6-4. The longitudinal optic (LO) modes occur at the zeroes of the undamped dielectric function. We estimate the LO mode frequencies here by temporarily setting the damping of the fit to 0.1 cm^{-1} and observing the zero crossings of the real part of the permittivity.

The low frequency section of the ϵ'' and σ' plots above suggest the presence of a mode below 30 cm^{-1} . Without this mode, the static dielectric constant, obtained by summing the lattice and electronic contributions from the fit, is ~ 85 , lower than the dielectric constant shown in Chapter 5, $\epsilon_{\text{sum}} = 115$. The additional low frequency mode may account for this difference.

Table 6-4. Parameters for the phonon modes in the 20 K infrared spectrum of $\text{Bi}_2\text{Ti}_2\text{O}_7$. An asterisk (*) indicates mode splitting. A double asterisk (**) indicates a split A-O' mode. A dagger (†) indicates modes that are observed but not included in the fit as described in present work.

Mode	$\text{Bi}_2\text{Ti}_2\text{O}_7$	20 K			
	Mode assignment	Resonant frequency ω (cm^{-1})	Oscillator strength $\Delta\epsilon$	Damping coefficient γ (cm^{-1})	LO Mode ω (cm^{-1})
$\omega_{7\dagger}$	(O'-A-O') Bend	~10	--	--	--
ω_{7^*}	(O'-A-O') Bend	39	20.6	27	44
ω_{7^*}	(O'-A-O') Bend	56	4.70	24	59
ω_7	(O'-A-O') Bend	77	4.81	35	80
ω_6	(O-A-O) Bend	186	42.9	68	265
ω_5	(A-BO ₆) Stretch	273	1.40	77	319
ω_{4^*}	(O-B-O) Bend	357	3.05	58	386
ω_4	(O-B-O) Bend	398	1.36	57	474
ω_3	(A-O) Stretch	483	0.365	41	528
ω_2	(A-O') Stretch	532	0.103	43	566
ω_{1^*}	(B-O) Stretch*	569	0.0653	38	612
ω_{1^*}	(B-O) Stretch*	613	0.0123	18	647
ω_1	(A-O') Stretch	650	0.0147	12	700
ω_n^{**}		764	0.0301	35	774
ϵ_∞			3.05		
$\epsilon(\text{Sum})$			85.3		

Because of the large mass of Bi, the resonance frequencies of low-frequency oscillators in conventional pyrochlores are pushed down to even lower frequency

values. A comparison of titanate pyrochlores performed by Kumar *et al.* shows the trend of decreasing low frequency oscillators as the mass of the A site atom increases.¹⁰³ Bismuth is the heaviest atom crystallizing a titanate in the pyrochlore structure, and thus the O'-A-O' bend and O-A-O bend modes are expected to be pushed down to lower frequencies when compared with previously reported pyrochlore titanates. The O-A-O bend mode is observed at 186 cm⁻¹ and the O'-A-O' bending mode is observed at the lower wavenumbers (<77cm⁻¹) and through extrapolation could possibly be pushed further down near 10 cm⁻¹, which would explain the increase in reflectivity in the low frequency region. Although outside of the scope of this work, it would be ideal to complement this data with terahertz spectroscopy investigations to further corroborate this interpretation.

Finally, the data show that bismuth titanate exhibits a phonon mode at around 764 cm⁻¹, identified as ω_n^{**} in Table 6-4. This feature is also observed in BZN and related pyrochlores has been attributed to disorder of A and static displacements of the O',⁹² this A-O' disorder is also found in Bi₂Ti₂O₇.

Taken as a whole, the Raman and IR spectra are strong evidence of non-correlated atomic displacements of both the A and B site of Bi₂Ti₂O₇. Bismuth non-correlated atomic displacements are shown by the presence of an IR assigned mode in the Raman spectra. The atypical behavior of the Ti-O modes in the higher range of the Raman spectra provide evidence of displacement of the Ti atomic position. The IR spectra further reveals disorder in the A and O' sites due to the splitting of the appearance of the ω_n^{**} mode.

6.4 Conclusion

The Raman spectra of the pyrochlore $\text{Bi}_2\text{Ti}_2\text{O}_7$ was measured on both calcined powder and sintered ceramic, showing that both spectra were identical. This provides evidence that no major structural change occurs during sintering. Raman modes were assigned by comparison to other bismuth and titanate pyrochlores found in literature, $\text{Bi}_2\text{Ti}_2\text{O}_7$ displays evidence of non-correlated atomic displacements in both the *A* and *B* site. A low frequency F_{1u} mode (normally IR-active) is assigned in the Raman spectra, due to the relaxation of the selection rules resulting from the displacement of the Bi atom from its ideal crystallographic position. Additionally, evidence of displacement in the Ti atomic position is provided by the atypical spectroscopic behavior of the Ti-O modes at the higher range of the Raman spectra. The IR spectra were fit to an oscillator model from which the real and imaginary parts of the dielectric function were obtained. The low frequency O-A-O and O'-A-O' phonon modes are pushed to lower frequencies due to the large mass of the Bi ion. The appearance of the ω_n^{**} also indicates a disorder of the A site and O' displacement.

CHAPTER 7 ORIGIN OF DIELECTRIC RELAXATION IN PYROCHLORES

7.1 Introduction

In this Chapter, an overview of all pyrochlores exhibiting dielectric relaxation will be performed and, with the synthesis and characterization of $\text{Bi}_2\text{Ti}_2\text{O}_7$ and other pyrochlores synthesized in this dissertation, gain a comprehensive understanding of the necessary conditions required in pyrochlores to display dielectric relaxation.

To start with a brief history, the phenomenon dielectric relaxation in bismuth based pyrochlore systems was first reported by Golovshchikova *et al.* in the 1970's,¹⁰⁴ finding that this dielectric anomaly had two main characteristics for relaxation:

1. Dispersive decrease in the dielectric permittivity with increasing frequency
2. The maximum in ϵ'' is observed at a lower temperature than that of ϵ'

Cann *et al.* then performed a detailed investigation on the dielectric properties of several compounds confirming the presence of dielectric relaxation in various bismuth pyrochlores.²¹ Since then significant progress has been made to further the knowledge of dielectric relaxation in pyrochlores, including by the Nino research group. Over the last 20 years there has been an explosive growth of interest in the dielectric properties of pyrochlores. It is not surprising perhaps, as bismuth pyrochlores combine a focus on materials with very strong practical properties and a challenging fundamental consideration. The focus on understanding relaxation in pyrochlores stemmed from the synthesis and characterization of $\text{Bi}_{1.5}\text{Zn}_{1.0}\text{Nb}_{1.5}\text{O}_7$ (BZN), which has become the archetypal material for pyrochlore relaxation behavior.^{13,105}

The dielectric relaxation phenomenon was introduced in Chapter 2, where the temperature and frequency dependence of ϵ' and ϵ'' was presented. In order to develop an understanding of relaxation in pyrochlores relevant experimental and theoretical

facts observed in the areas of investigation covered in this thesis, as well as results reported in literature, are summarized below:

1. T_m follows an Arrhenius behavior. This allows for the calculation of attempt jump frequency (ν_0). In BZN this corresponds to the bending phonon mode assigned to the A-site.⁴⁵
2. Calculated activation energies range between 0.112-0.559 eV^{21-23,45,72,87,88}. These values are similar to those found in similar relaxing systems such as relaxor ferroelectrics and dipolar glasses.
3. The A-cations in displaced pyrochlores are randomly displaced (along six $\langle 0\bar{1}\bar{1}\rangle$ equivalent directions) from the ideal pyrochlore positions. In addition, the O' ions are randomly displaced among six directions. These displacements are seen in BZN which also has similar displacements as well as chemical substitutions in both the A and B sites.
4. There have also been studies confirming the existence of short-range correlations between the O' displacements and both the occupancy and direction of displacement for the A-site cation in BZN.¹⁰⁶ This A-site random occupancy breaks up the translational symmetry of the lattice.
5. Vibrational spectroscopy of BZN determined that up to ~80% of the dielectric permittivity is due to the O'-A-O' and O-A-O bond bending phonon modes. Based on the phonon modes, activation energy, and attempt jump frequency it has been suggested that the dielectric relaxation may be due to local atomic hopping events of the A-site cations in the A_2O' sub-network.¹

In the remainder of this Chapter, a formalism on the necessary and sufficient conditions for the appearance of dielectric relaxation in pyrochlores will be discussed using the additional knowledge gained from the new pyrochlores systems studied in this dissertation.

7.2 Discussion

Table 7-1 shows a summary of the pyrochlores reported in literature that display dielectric relaxation and which of the three conditions for relaxation are present in each material. Cation substitution was further broken down to A-site only, B-site only, or both A- and B-site substitution.

Table 7-1. Pyrochlores and the conditions present for possible relaxation

Material	Polarizable Lone Pair A-site	A- and B- site substitution	A-site substitution	B-site substitution	Atomic Displacements	Relaxation	Key Reference
$\text{Bi}_2(\text{ScNb})\text{O}_7$	Yes	--	No	Yes	Yes	Yes	21
$\text{Bi}_2(\text{ScTa})\text{O}_7$	Yes	--	No	Yes	Yes	Yes	21
$(\text{Bi}_{1.5}\text{Zn}_{0.5})(\text{Zn}_{0.5}\text{Nb}_{1.5})\text{O}_7$	Yes	Yes	--	--	Yes	Yes	13
$(\text{Bi}_{1.5}\text{Zn}_{1.5})(\text{Zn}_{0.5}\text{Ta}_{1.5})\text{O}_7$	Yes	Yes	--	--	Yes	Yes	25
$\text{Bi}_{1.657}\text{Fe}_{1.092}\text{Nb}_{1.150}\text{O}_7$	Yes	Yes	--	--	Yes	Yes	24
$\text{Bi}_{1.67}\text{Mg}_{0.64}\text{Nb}_{1.53}\text{O}_7$	Yes	Yes	--	--	Yes	Yes	47
$\text{Bi}_{1.68}\text{Ni}_{0.747}\text{Nb}_{1.493}\text{O}_7$	Yes	Yes	--	--	Yes	Yes	47
$\text{Bi}_{1.657}(\text{Fe}_{0.983}\text{Al}_{0.109})\text{Nb}_{1.150}\text{O}_7$	Yes	Yes	--	--	Yes	Yes	48
$\text{Bi}_2(\text{InNb})\text{O}_7$	Yes	--	No	Yes	Yes	Yes	23
$(\text{Bi}_{1.93}\text{Fe}_{0.07})(\text{Fe}_{1.42}\text{Te}_{0.58})\text{O}_7$	Yes	Yes	--	--	Yes	Yes	49
$\text{Ca}_{1.46}\text{Ti}_{1.38}\text{Nb}_{1.11}\text{O}_7$	No	Yes	--	--	Yes	Yes	50

Since most of the research work has focused on Bi-pyrochlores, and especially BZN, a review of the phenomenon showed that in all cases investigated relaxation occurs when:

1. A polarizable lone-pair cation occupies the A-site
2. There is cation substitution
3. Atomic displacement is present

In order to isolate the effects of having a highly polarizable A-site on dielectric relaxation in pyrochlores Roth *et al.* synthesized a displaced and substituted pyrochlore without a lone pair containing cation in the A-site, $\text{Ca}_{1.5}\text{Ti}_{1.5}\text{NbO}_7$ (CTN).⁵⁰ While this pyrochlore does not contain a highly polarizable A-site, it still has the displacive disorder in the $\text{A}_2\text{O}'$ sub-network and chemical substitution in both the A and B site similar to the other pyrochlores that exhibit relaxation, such as BZN. CTN does in fact display dielectric relaxation behavior, this behavior suggests that the presence of polarizable lone-pair cations (such as Bi^{3+}) is not necessary in order for pyrochlores to display dielectric relaxation.

The work in this dissertation has focused on $\text{Bi}_2\text{Ti}_2\text{O}_7$ due to the fact that it is the only stoichiometric bismuth based cubic pyrochlore which also exhibits atomic displacement. Bismuth titanate presents an opportunity to isolate the effect of atomic displacements without cation substitutions on dielectric relaxation.

In an effort to isolate the effects of cation substitution without atomic displacements several different pyrochlores were synthesized. In particular, the $(\text{Sm}_x\text{Yb}_{1-x})_2\text{Ti}_2\text{O}_7$ and $\text{Sm}_2(\text{Sn}_x\text{Ti}_{1-x})_2\text{O}_7$ pyrochlore present a unique opportunity to isolate A- and B-site substitution without atomic displacements.

Table 7-2. New pyrochlores from this work and the conditions present for possible relaxation

Material	Polarizable Lone Pair A-site	A- and B-site substitution	A-site substitution	B-site substitution	Atomic Displacements	Relaxation	Reference
$\text{Bi}_2(\text{ScNb})\text{O}_7$	Yes	--	No	Yes	Yes	Yes	21
$\text{Bi}_2(\text{ScTa})\text{O}_7$	Yes	--	No	Yes	Yes	Yes	21
$(\text{Bi}_{1.5}\text{Zn}_{0.5})(\text{Zn}_{0.5}\text{Nb}_{1.5})\text{O}_7$	Yes	Yes	--	--	Yes	Yes	13
$(\text{Bi}_{1.5}\text{Zn}_{1.5})(\text{Zn}_{0.5}\text{Ta}_{1.5})\text{O}_7$	Yes	Yes	--	--	Yes	Yes	25
$\text{Bi}_{1.657}\text{Fe}_{1.092}\text{Nb}_{1.150}\text{O}_7$	Yes	Yes	--	--	Yes	Yes	24
$\text{Bi}_{1.67}\text{Mg}_{0.64}\text{Nb}_{1.53}\text{O}_7$	Yes	Yes	--	--	Yes	Yes	47
$\text{Bi}_{1.68}\text{Ni}_{0.747}\text{Nb}_{1.493}\text{O}_7$	Yes	Yes	--	--	Yes	Yes	47
$\text{Bi}_{1.657}(\text{Fe}_{0.983}\text{Al}_{0.109})\text{Nb}_{1.150}\text{O}_7$	Yes	Yes	--	--	Yes	Yes	48
$\text{Bi}_2(\text{InNb})\text{O}_7$	Yes	--	No	Yes	Yes	Yes	23
$(\text{Bi}_{1.93}\text{Fe}_{0.07})(\text{Fe}_{1.42}\text{Te}_{0.58})\text{O}_7$	Yes	Yes	--	--	Yes	Yes	49
$\text{Ca}_{1.46}\text{Ti}_{1.38}\text{Nb}_{1.11}\text{O}_7$	No	Yes	--	--	Yes	Yes	50
$\text{Bi}_2\text{Ti}_2\text{O}_7$	Yes	No	No	No	Yes	No	This Work
$\text{Sm}_2\text{Ti}_2\text{O}_7$	No	No	No	No	No	No	This Work
$(\text{Sm}_{0.25}\text{Yb}_{0.75})_2\text{Ti}_2\text{O}_7$							This Work
$(\text{Sm}_{0.5}\text{Yb}_{0.5})_2\text{Ti}_2\text{O}_7$	No	--	Yes	No	No	No	This Work
$(\text{Sm}_{0.75}\text{Yb}_{0.25})_2\text{Ti}_2\text{O}_7$							This Work
$\text{Sm}_2(\text{Sn}_{0.5}\text{Ti}_{0.5})_2\text{O}_7$	No	--	No	Yes	No	No	This Work

With the addition of these new pyrochlores to Table 7-2 one can provide key insights into what requirements are necessary in order to display dielectric relaxation.

As stated before, the observation of dielectric relaxation in the Ca-Ti-(Nb,Ta)-O pyrochlores⁵⁰ discards the presence of lone pair electrons or highly polarizable lone pair cations as a necessary condition for the emergence of dielectric relaxation in pyrochlores. Nevertheless, atomic displacements and substitutional cations are present in those Ca-pyrochlores. The dielectric and structural analysis of $\text{Bi}_2\text{Ti}_2\text{O}_7$ in this work has revealed that combined atomic displacements and high polarizability of the A-site are not enough to lead to the onset of dielectric relaxation. This result in combination with the observations in Ca-pyrochlores suggests that substitutional cations play an essential role in the emergence of relaxation behavior in these compounds.

The synthesis and characterization of the $(\text{Sm}_x\text{Yb}_{1-x})_2\text{Ti}_2\text{O}_7$ and $\text{Sm}_2(\text{Sn}_x\text{Ti}_{1-x})_2\text{O}_7$ pyrochlores allowed for the study of the effects of chemical substitution. Both systems are ideal pyrochlores and do not show evidence of displacements. As shown in Chapter 5 these pyrochlores do not display dielectric relaxation. While chemical substitutions are a necessary condition for dielectric relaxation, it is not sufficient to induce dielectric relaxation without the presence of atomic displacements.

It is clear that the combination of substitutional cations and atomic displacements play a key role in dielectric relaxation. In order to understand the impact of these two factors a further look into the dynamics of the local environment and electronic structure of BZN and $\text{Bi}_2\text{Ti}_2\text{O}_7$ is necessary.

The effect of substitutional cations in BZN on the local structure was investigated by Withers *et al.* using electron diffraction and Monte Carlo calculations. Guidelines for the preferred orientations of Zn cations in the $\text{A}_2\text{O}'$ and B_2O_6 sub-networks were proposed. These guidelines can be briefly summarized as randomly distributed Zn_B in

the B_2O_6 network and $\langle 211 \rangle$ directional ordering of Zn_A cations with one Zn_A per A_2O' tetrahedron. Building off these proposed guidelines, DFT calculations performed by Hinojosa *et al.* allowed for the visualization of the energy landscape of the A-site cation in BZN and $Bi_2Ti_2O_7$. Figure 7-1 presents the electronic localization function (ELF) for a portion of the $(\bar{1}11)$ plane for the $Bi_2Ti_2O_7$ and BZN systems. An outline (dashed hexagon) of the $O'A_4$ tetrahedra sub-network and the A-site displacement directions are also highlighted (black arrows for in-plane and white circles for out of plane displacements).

In Figure 6-2, the Bi lone pairs are asymmetric and point away from the cation and in the opposite direction of the atomic displacement in both BZN and $Bi_2Ti_2O_7$. Cation substitution considerably altered the ELF of the O' in BZN, the O' anions preferentially displace towards the Zn_A cations. The nature of the correlated atomic displacements in $Bi_2Ti_2O_7$ can be understood by comparing the ELF of $Bi_2Ti_2O_7$ and BZN. Without the presence of another cation on the A-site, the correlated displacement provides an even distribution of the lone pair electrons onto the BO_6 octahedra network reducing the stereochemical strain associated with the presence of the lone pair electrons.^{26,107-109} In BZN, however, the Zn_A cations reduce the interaction between the A_2O' and B_2O_6 sub-networks and open up the confined space allowing for the incorporation of the Bi lone pairs. Therefore by having substitutional cations, BZN breaks the correlated displacement arrangement of the Bi cation displayed by $Bi_2Ti_2O_7$.

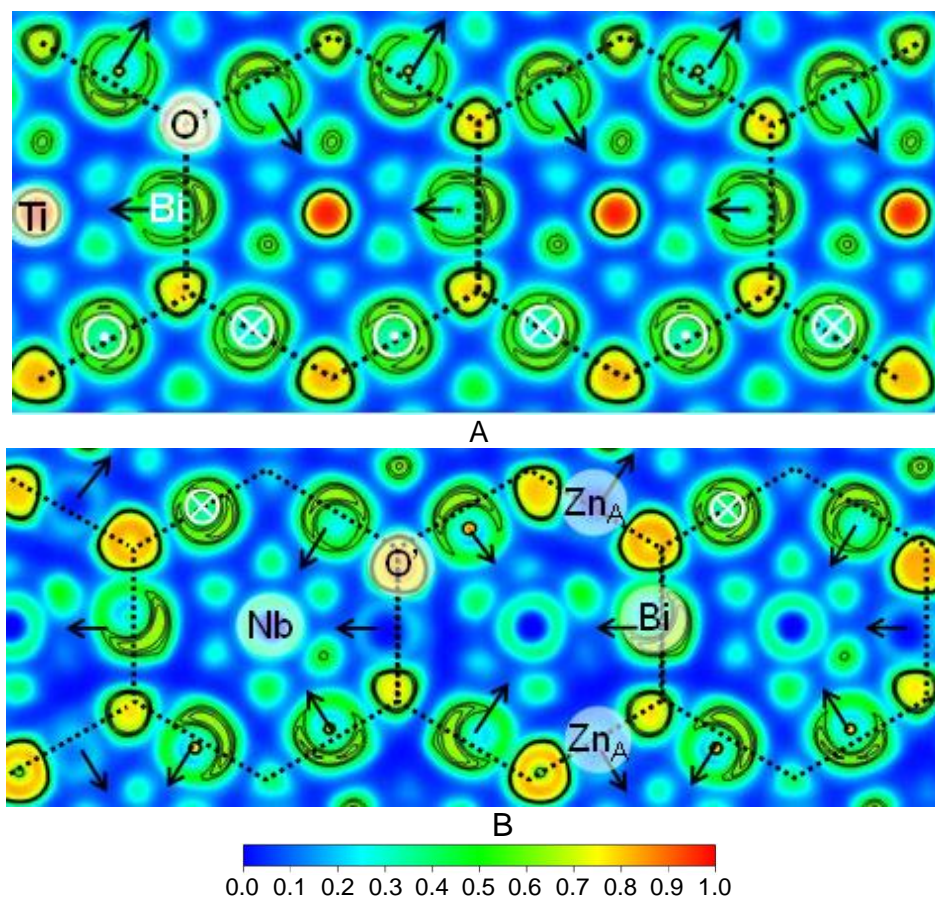


Figure 7-1. The electron localization function (ELF) for a portion of the $\bar{1}\bar{1}1$ plane for A) $\text{Bi}_2\text{Ti}_2\text{O}_7$ and B) BZN pyrochlore compounds from 0.0 (delocalized) in blue to 1.0 (fully localized) in red. The cation displacements are indicated by the solid black arrows (in plane displacement) or the white circles (out-of-plane displacement). Figures adapted from Hinojosa *et al.*¹⁰⁸

In addition to affecting the ELF, it is clear that the inclusion of cation substitutions significantly affect the energy profiles and cation pathways for hopping between crystallographic positions. Further calculations were undertaken by Hinojosa *et al.* to map the relative energy landscape of BZN and $\text{Bi}_2\text{Ti}_2\text{O}_7$, allowing for the visualization the atomic hopping among the 6 possible equivalent A-site positions.

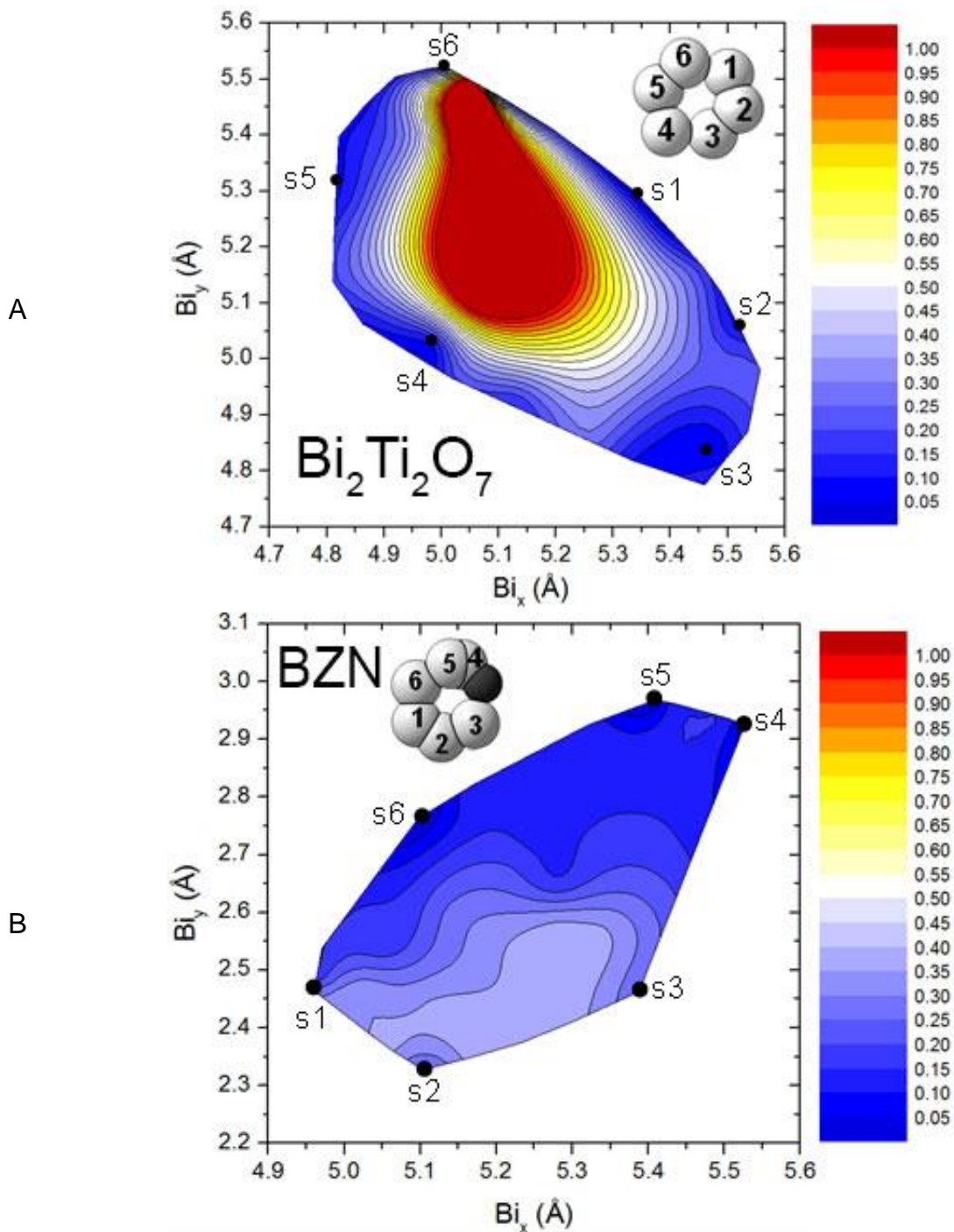


Figure 7-2. The relative energy landscape from 0.0 (blue) to 1.0 eV (red) plotted with respect to the x and y position for one Bi cation in A) $\text{Bi}_2\text{Ti}_2\text{O}_7$ and B) BZN. Figure adapted from Hinojosa *et al.*¹⁰⁸

The relative energy landscape of $\text{Bi}_2\text{Ti}_2\text{O}_7$ and BZN are shown in Figure 6-2. Through this type of plot it is easy to see that the Bi cations prefer to hop along the

periphery of the 96g ring in $\text{Bi}_2\text{Ti}_2\text{O}_7$. It is also evident that once Bi hops out of the lower energy states (s1, s2, and s3), the hopping events cost considerably more energy. However, unlike $\text{Bi}_2\text{Ti}_2\text{O}_7$, the Bi cations in BZN do not follow the 96g ring to jump between equivalent positions but instead the Bi cations transition through the center of the 96g ring. This type of jumping results in nearly the same energy costs for a single site hop or double or even a triple site hop.

Therefore, in BZN the Bi cations readily respond to an applied electric field and may undergo any type of hopping event, even flipping across the 96g ring with approximately the same activation energy. In contrast, the Bi cations in $\text{Bi}_2\text{Ti}_2\text{O}_7$ are limited in the types of hops (since they move along the outside of the 96g ring) they may undergo due to the local bonding environment and often these jumps cost considerably more energy.

The ELF and energy landscape visualizations help visualize why there needs to be both atomic displacements and substitution in order for dielectric relaxation in pyrochlores to take place. This is further confirmed by the absence of relaxation in both the Sm-systems and $\text{Bi}_2\text{Ti}_2\text{O}_7$ presented in Chapter 6.

7.3 Conclusion

The work presented in this dissertation adds a link to the conditions required in pyrochlores to exhibit dielectric relaxation. An in depth investigation into the structure and dielectric properties of $\text{Bi}_2\text{Ti}_2\text{O}_7$ showed that a pyrochlore displaying atomic displacements without substitution does not induce relaxation. This result points suggests that substitutional cations play a major role in the origin of dielectric relaxation in pyrochlores.

By investigating the dielectric response of the $(\text{Sm}_x\text{Yb}_{1-x})_2\text{Ti}_2\text{O}_7$ and $\text{Sm}_2(\text{Sn}_x\text{Ti}_{1-x})_2\text{O}_7$ pyrochlore systems the impact of cation substitutions on relaxation was targeted; as both systems are ideal pyrochlores and do not show evidence of displacements. As shown in Chapter 5 these pyrochlores do not display dielectric relaxation. While chemical substitutions are a necessary condition for dielectric relaxation, it is not sufficient on its own to induce dielectric relaxation without the presence of atomic displacements.

Therefore, in order to display dielectric relaxation in pyrochlores it is necessary to have both atomic displacements and cation substitutions. The presence of just one of these factors is not enough to induce relaxation. The DFT calculations of $\text{Bi}_2\text{Ti}_2\text{O}_7$ show that the Bi cation displays correlated displacements. However, by incorporating cation substitution into BZN this correlation is broken giving the Bi cation the freedom to hop to any possible site. On the other hand, $\text{Bi}_2\text{Ti}_2\text{O}_7$ shows a higher energy cost and is limited in the type and number of possible cation hops.

A break in the local symmetry of the material (impeding the coordinated displacements) may be the ultimate answer to the origin of relaxation, where random displacements are necessary in order to accommodate the cation hopping of the A-site cation through the center of the 96g ring.

CHAPTER 8
DIELECTRIC PROPERTIES OF TYPE-II Bi_3NbO_7

8.1 Introduction

It is well known that the high-temperature $\delta\text{-Bi}_2\text{O}_3$ form is stable between 729°C up to its melting point 825°C. This $\delta\text{-Bi}_2\text{O}_3$ phase can be described as an oxygen-deficient fluorite structure, also known as defect-fluorite. Since $\delta\text{-Bi}_2\text{O}_3$ exhibits a number of unique features, there is significant interest in stabilizing this phase below 729°C transition temperature. Examples of these unique crystallochemical characteristics include a high polarizability of the cation network, the ability of bismuth cations to dynamically accommodate asymmetric surroundings,¹¹⁰ and the anion network contains 25% intrinsic oxygen vacancies due to the stoichiometry of the unit cell.¹¹¹ Typically, in order to maintain these desirable properties a phase stabilization using Bi substitution with different metal cations is performed.¹¹²⁻¹¹⁴ Among the vast choice of possible cations that can be used to stabilize the $\delta\text{-Bi}_2\text{O}_3$ structure, the $(\text{Bi}_2\text{O}_3)_{1-x}(\text{Nb}_2\text{O}_3)_x$ ($\delta\text{-BN}_{\text{SS}}$) system is widely used due to the fact that these materials exhibit very high oxygen ion conductivity in combination with electronic conductivity.^{115,116}

Investigations of the $\delta\text{-BN}_{\text{SS}}$ have revealed four main superstructures (types I-IV). At 25 mol% Nb_2O_5 two crystal structures have been reported: type-I at the Bi rich end was found to be a sillenite related phase of composition $\text{Bi}_{12}\text{Nb}_{0.29}\text{O}_{18.7+x}$ ¹¹⁷ and is not related to the fluorite-type $\delta\text{-Bi}_2\text{O}_3$.¹¹⁸ Type II- Bi_3NbO_7 , a cubic defect fluorite structure,¹¹⁹ type III- Bi_3NbO_7 , an ordered tetragonal fluorite type superstructure,¹¹⁸ and type-IV $\delta\text{-BN}_{\text{SS}}$ ($\text{Bi}_5\text{Nb}_3\text{O}_{15}$) adopts an Aurivillius-related phase.¹²⁰ There has also been

investigation of the microwave dielectric properties of the $\text{Bi}_2\text{O}_3\text{-Nb}_2\text{O}_3$ system due to its possible compatibility with low-temperature cofired ceramic (LTCC) technology.¹²¹

Recently, single crystal type-II Bi_3NbO_7 has been synthesized via floating-zone crystal growth by Ling *et al.*¹²² In this work an investigation into the dielectric properties of type-II Bi_3NbO_7 single crystal as a function of temperature and frequency allows for correlations in the structure-dielectric properties within fluorite-related structures.

8.2 Dielectric Spectroscopy

Figure 8-1 shows the dielectric properties of type-II Bi_3NbO_7 as a function of temperature at different frequencies from 1 kHz to 2 MHz. The real part of the permittivity decreases from 87 to 81 between 300 and 20 K. The real part shows two slope variations with associated changes in the imaginary part with a peculiar cross-over at approximately 100 K, followed by a slight increase in loss around 40 K. Dielectric relaxation is a phenomenon observed in many bismuth pyrochlores,^{12,22,23,45,70,71} where these materials exhibit a step-like decrease in the real part of the dielectric permittivity accompanied by a frequency-dependent peak in the imaginary part. However, the imaginary peaks present in type II- Bi_3NbO_7 are very diffuse, and the behavior of Bi_3NbO_7 does not provide a clear evidence of a dipolar relaxation event. At higher temperatures (approx. 400 K) frequency dispersion in the real part of the relative permittivity occurs, accompanied by a sharp increase in the imaginary part at 1 kHz (~9 at 400 K). This behavior is consistent with the onset of electrical conduction.

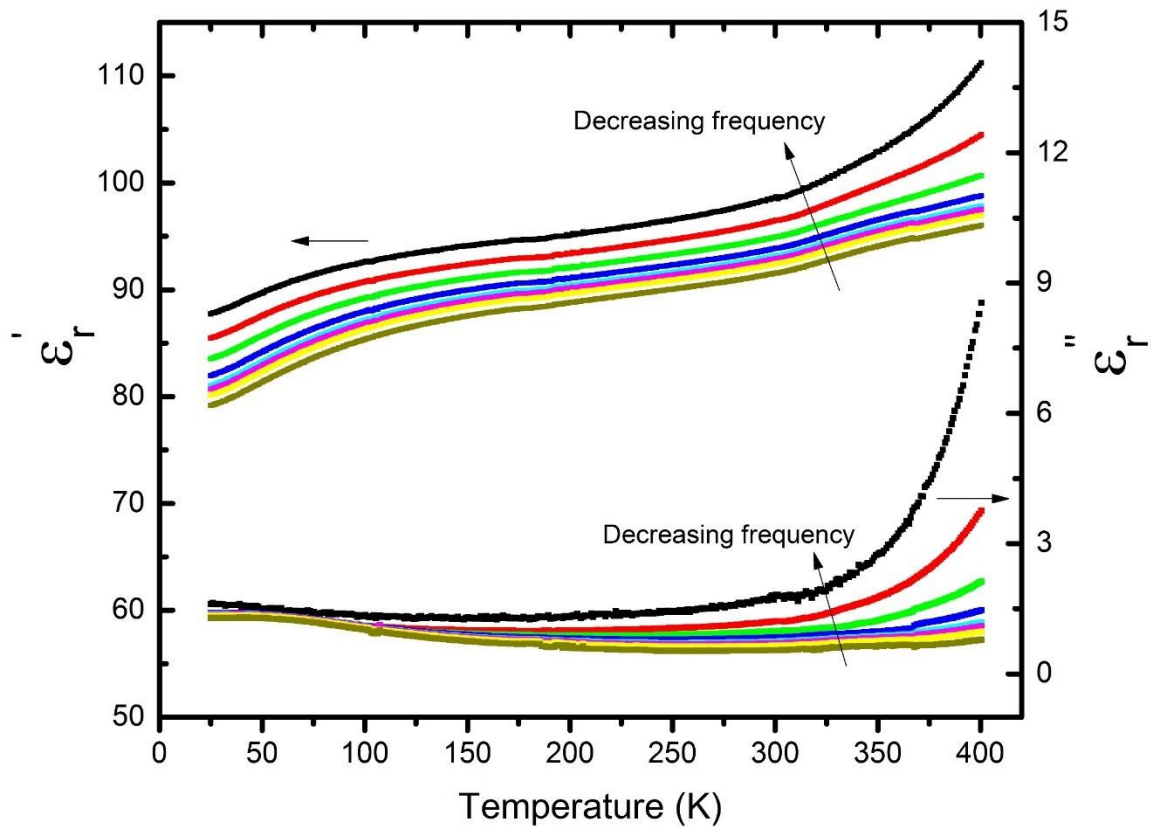
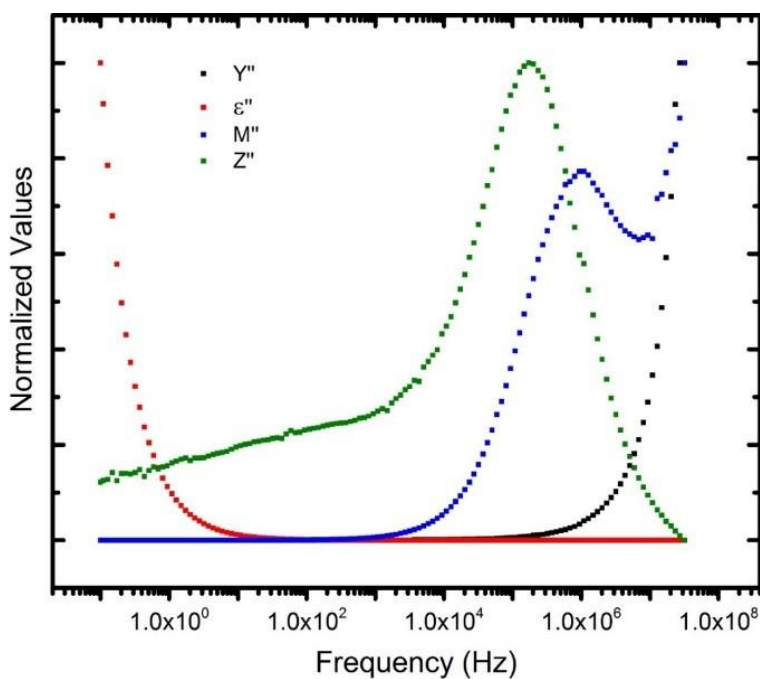


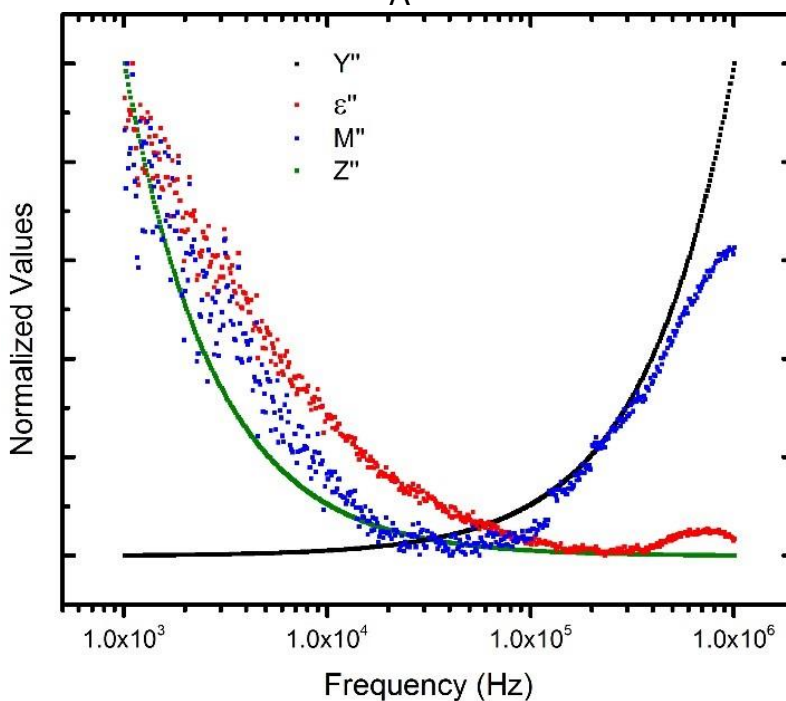
Figure 8-1. Real and imaginary part of the permittivity of single crystal type-II Bi_3NbO_7 at 1 kHz, 10 kHz, 100 kHz, 500 kHz, 1 MHz, 1.2 MHz, 1.5 MHz and 2MHz.

To further analyze the dielectric response of type-II Bi_3NbO_7 , one can characterize the onset of electrical conduction by viewing the imaginary components of the dielectric functions (i.e. impedance (Z), admittance (Y), permittivity (ϵ), and modulus (M)). This analysis also allows for the investigation of whether dielectric relaxation occurring along with conductivity. As shown in the work by Cao and Gerhardt⁸⁵ conductivity will result in $\tau_M = \tau_Z$, where τ is the relaxation time of the specific dielectric function. Therefore, both the M'' and the Z'' peaks will overlap throughout the entire frequency range, thereby giving a clear indication that conductivity is occurring. It

Figure 6-2 was observed that Bi_3NbO_7 begins to display this behavior at 473 K. In the normalized values of Y'' , Z'' , ϵ'' , and M'' are shown as a function of frequency at 473 K.



A



B

Figure 8-2. Normalized functions of the imaginary components of the impedance (Z''), admittance (Y''), modulus (M''), and permittivity (ϵ'') at A) 473 K and B) 150 K.

By analyzing the dielectric functions as a function of frequency in Figure 8-2A it is clearly evident that M'' and Z'' display clear peaks over the same frequency range while both the ϵ'' and Y'' have no observable peak in this frequency range, showing that the onset of conduction begins at 473 K and there is no observable dielectric relaxation occurring due to the fact that there is no observable ϵ'' over the measured frequency range. Figure 8-2B shows the dielectric functions as a function of temperature at 150 K. It is important to note that, unlike Figure 8-2A, the Z'' does not have an observable peak in this frequency range, ruling out conduction. Further, since the ϵ'' does not have an observable peak in this range, it can be inferred that no clear dielectric relaxation is occurring at 150 K over the observed frequency range.

It is worth noticing that the dielectric behavior displayed by type II-Bi₃NbO₇ is very similar to that displayed by Ln₃NbO₇ (Ln = Dy, Er, Yb and Y), rare earth niobates that also adopt a defect fluorite structure.¹¹³

8.3 Defect Fluorite Structure-Dielectric Property Relationship

To recall briefly, Weberite-type Ln₃BO₇ compounds (where Ln³⁺ is a rare earth element, and B is Os⁵⁺, Re⁵⁺, Ru⁵⁺, Re⁵⁺, Mo⁵⁺, Ir⁵⁺, Sb⁵⁺, Nb⁵⁺, or Ta⁵⁺) have attracted attention due to their interesting magnetic¹²³⁻¹²⁵, dielectric^{126,127}, and photocatalytic properties.^{128,129} Weberites and pyrochlores, expressed as A₂B₂O₇ can be seen as anion deficient superstructure derivatives of the fluorite structure (MO₂). A review on weberites was recently published by L. Cai and coworkers.¹³⁰ The series Ln₃NbO₇ (Ln = Nd, Gd, Dy, Er, Yb, and Y) has been previously investigated and a change in the crystal structure from defect cubic fluorite to orthorhombic weberite-type structures with increasing Ln³⁺ ionic radius was reported.¹²⁷

Specifically, the cubic defect-fluorite structure in Ln_3NbO_7 was shown to be stabilized when the ionic radius of the rare earth is equal or less than that of Dy^{3+} (1.207 Å).¹³¹ Unlike pyrochlores ($\text{A}_2\text{B}_2\text{O}_7$) in which A, B and the oxygen vacant sites have ordered arrangements, the defect-fluorite structure has both disordered cations as well as disordered oxygen deficiency sites.

The real part of the permittivity of the Ln_3NbO_7 follow the same trend although the permittivity of type-II Bi_3NbO_7 is significantly higher. The imaginary component of the permittivity is also very similar to that of that of Ln_3NbO_7 , although type-II Bi_3NbO_7 has higher losses and the onset of conduction occurs at significantly lower temperatures. For comparison, the lattice parameters of Bi_3NbO_7 and Ln_3NbO_7 ($\text{Ln} = \text{Dy}, \text{Er}, \text{Yb}$ and Y) are presented in Table 8-1. The parameters were calculated using the Nelson-Riley function for cubic structures and through neutron refinement for Bi_3NbO_7 .¹²² The structure of type-II Bi_3NbO_7 single crystal has been reported by Ling *et al.* through neutron diffraction as a cubic defect-fluorite structure with a lattice parameter of 5.479 Å.

Table 8-1. Lattice parameters of Ln_3NbO_7 ($\text{Ln} = \text{Dy}, \text{Er}, \text{Yb}, \text{Y}$) and Bi_3NbO_7 .

Compound	a (Å)	Ionic radius of A site (Å) ¹³²
typell- Bi_3NbO_7	5.479	1.17
Dy_3NbO_7	5.2701	1.027
Y_3NbO_7	5.2534	1.019
Er_3NbO_7	5.2318	1.004
Yb_3NbO_7	5.1944	0.985

Astafyev *et al.*¹³³ proposed that the “looseness” of the structure increases the probability of polar distortions of these structures. Using the lattice parameters and ionic radii found in Table 8-1, type II Bi_3NbO_7 has the largest specific free volume ratio of 50.4% while the other Ln_3NbO_7 have a ratio between (42-45%). Based on this, it can

be reconciled that the openness of the type-II Bi_3NbO_7 structure allows for the reorientation of the dipoles within the structure giving rise to a higher permittivity.

This comparative response can be observed in Figure 8-3 where the theoretical permittivity of the structure is calculated using the Clausius-Mossotti Equation and compared to the experimental permittivity. The Clausius-Mossotti Equation does not factor in dipolar contributions to the permittivity. Therefore, by comparing the theoretical values of permittivity to the experimental, a rough estimate of the dipolar contribution to the permittivity can be extracted.

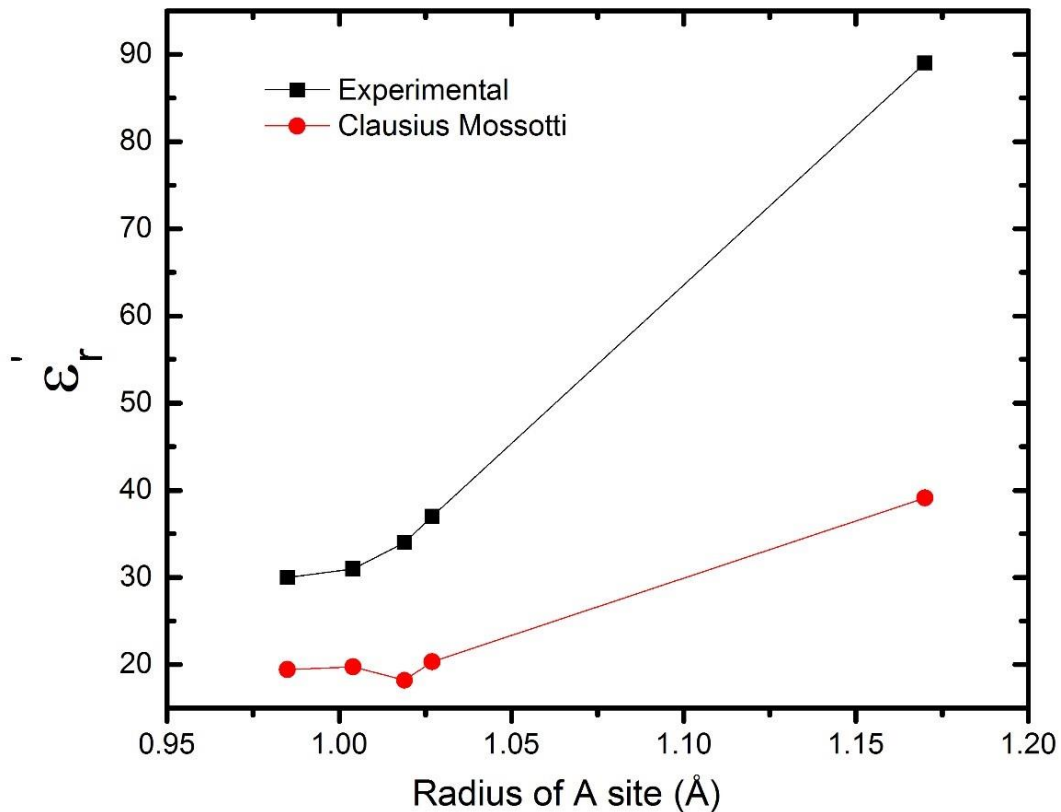


Figure 8-3. Experimental and theoretical (Clausius-Mossotti) permittivity of type-II Bi_3NbO_7 and Ln_3NbO_7 defect fluorites.

For the Ln_3NbO_7 the difference from the theoretical to experimental permittivity is relatively constant. However, for type-II Bi_3NbO_7 this difference is significantly higher

and can be attributed to the dipolar component of the permittivity as a result of both of the higher polarizability of Bi and the comparatively openness of the compound.

We now turn our attention to variation of permittivity as a function of temperature. The temperature coefficient of capacitance (TCC) describes the change in capacitance over a specified temperature range. A review by Harrop *et al.*¹³⁴ presented that materials with higher values of dielectric permittivity (paraelectrics) exhibit extremely negative values of TCC. For capacitive components in electronic applications stability is important and therefore, a flat TCC (e.g. $\pm 15\text{-}50$ ppm/ $^{\circ}\text{C}$ or MK^{-1}) is desirable. This is typically achieved by a composite approach mixing two dielectric compounds with opposite TCC or by compositional tailoring. Cai *et al.* demonstrated that it was possible to tailor the TCC of Ln_3NbO_7 ($\text{Ln} = \text{Dy}, \text{Er}, \text{Yb}, \text{and Y}$) as a function of ionic radius of the A site.¹³¹

Here, the TCC was calculated from 218 to 350 K for Ln_3NbO_7 ($\text{Ln} = \text{Dy}, \text{Er}, \text{Yb}, \text{and Y}$) and compared with the value obtained from type-II Bi_3NbO_7 as shown in Figure 8-4. It can be seen that as the atomic radius of the A site increases, the TCC of the defect-fluorite Ln_3NbO_7 decreases and that type-II Bi_3NbO_7 has a positive TCC. However, it is a lower value and seems to follow the general trend of the defect-fluorite Ln_3NbO_7 series, possessing the lowest TCC of the defect fluorite Ln_3NbO_7 's.

It has been proposed that the TCC in defect fluorite type Ln_3NbO_7 may increase with structural disorder as the local ordering should increase with an increasing difference between the ionic radius of Nb^{5+} and Ln^{3+} .¹³¹ Therefore, one would expect the TCC of type-II Bi_3NbO_7 to be significantly lower than any of the defect fluorite Ln_3NbO_7 as the ionic radius of Bi^{3+} is the largest of the series.

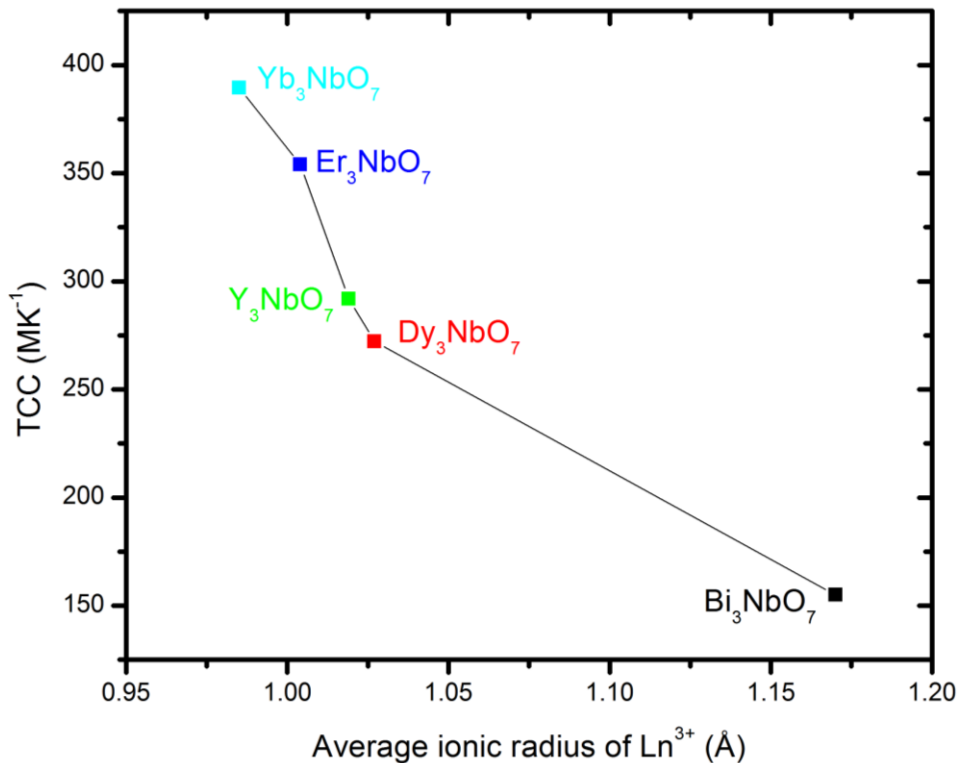


Figure 8-4. TCC of defect-fluorite Ln₃NbO₇ and type-II Bi₃NbO₇ from 218 K to 350 K.

It is also interesting to note that as the ionic radius of the Ln³⁺ increases across the Ln₃NbO₇ series, there is a change to an orthorhombic weberite related crystal structure when the Ln³⁺ > Dy³⁺ (1.027 Å). However, the structure of type-II Bi₃NbO₇ is a defect fluorite despite the fact that the ionic radius of bismuth is larger than the Ln³⁺ series. That is, one would expect type-II Bi₃NbO₇ to be orthorhombic rather than a stable defect cubic fluorite. A possible explanation for this exception may be the fact that bismuth is stereochemically active and highly polarizable¹¹⁰ which may allow for the accommodation into a defect fluorite structure.

One can further probe into the optimization of the bonding requirements of the cation sites by contrasting bond valence sums (BVS)¹³⁵ of the A site in the Ln₃NbO₇ series with those of type-II Bi₃NbO₇. BVS can be used as a measure of the tendency of the structure to distort. For optimum bonding satisfaction, the BVS for the A site would

be equal to its oxidation state i.e., 3 for Bi, in this case. BVS can also show if an atom is under or over-coordinated. BVS is calculated using Equation 8-1:

$$|BVS_i| = \sum_j \exp\left(\frac{R_o - R_{ij}}{b}\right) \quad (8-1)$$

R_o and B are empirical parameters¹³⁵ unique to the A site cation. R_{ij} is the bond length from the i site to the j site, in this case A to O.

Figure 8-5 shows the BVS for the A-site atom in the defect fluorite structure. This structure leads to two possible A-O bond lengths (one short, one long), for each of the 7 A-O bonds with one oxygen vacancy. The x-axis shows the different possible configurations of the structure with the number of longer bonds. For the A-site, the most preferable configuration would be one where the BVS is ~3. For most of the Ln₃NbO₇ series the BVS of ~3 occurs when there are between 2 and 3 longer bonds. However, for type-II Bi₃NbO₇, the preferred configuration lies between 4 and 5 longer bonds. For comparison, a theoretical ideal structure of Bi₃NbO₇ was calculated (with and without an oxygen vacancy) and it can be seen that by adopting a defect fluorite structure type-II Bi₃NbO₇ can attain a BVS closer to the ideal value of 3.

In addition, the bond strain index can also be used to determine the strain in the bonding arrangements of the structure. It is shown by Equation 8-2:

$$BSI = \langle (S_{ij} - s_{ij})^2 \rangle^{1/2} \quad (8-2)$$

S_{ij} is the experimental bond valence and s_{ij} is the theoretical bond valence of bond ij . A structure is typically considered strained when the BSI is greater than 0.05 valence units (vu).

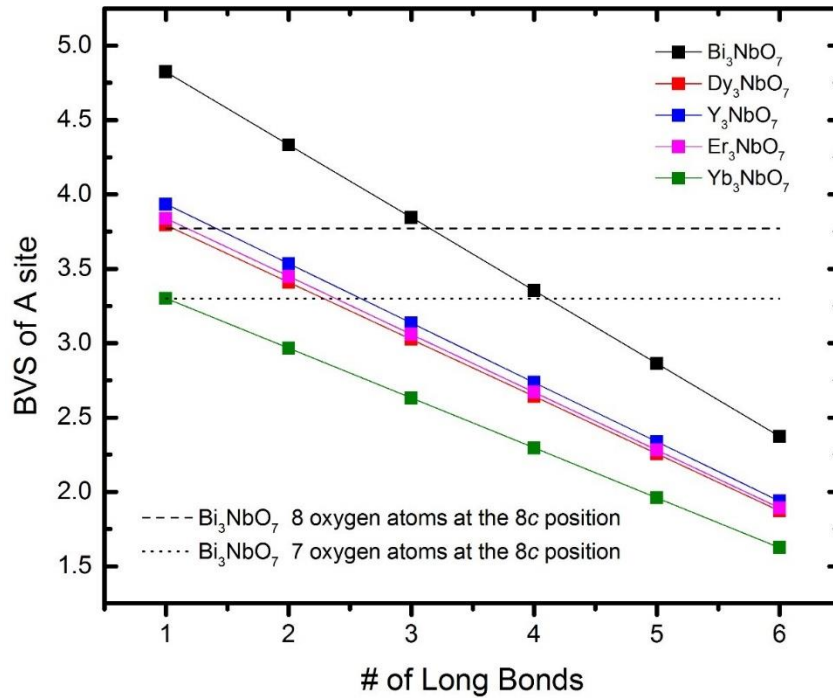


Figure 8-5. BVS of Ln₃NbO₇ and type-II Bi₃NbO₇ defect fluorite showing the possible bonding arrangements. The dashed and dotted lines represent Bi₃NbO₇ at the ideal fluorite position for comparison with the defect fluorite Bi₃NbO₇ structure.

Figure 8-6 shows the BSI for the Ln₃NbO₇ and type-II Bi₃NbO₇ in contrast to the ideal fluorite structure (shown as dotted and dashed line). By adopting the defect fluorite structure, the BSI becomes greater than the 0.2 indicating some strain in the structure. Higher strains are present in the structure with higher number of long bonds. However, Figure 8-5 shows that having around three long bonds the valence of the A site is favored.

Finally, another useful metric for analyzing the stability of the overall structure is the global instability index (GII), the root square mean of the deviation of the BVS's from the expected values for all atoms in the unit cell.

$$GII = \sqrt{\frac{\sum(BVS - BVS_0)^2}{N}} \quad (8-3)$$

N is the number of atoms in the unit cell and BVS_0 is the expected BVS. Typical values of stable structures have a $GII < 0.2$ vu. In Figure 8-7, the GII s of the Ln_3NbO_7 defect fluorites are shown along with type-II Bi_3NbO_7 in both defect fluorite and ideal fluorite positions for comparison.

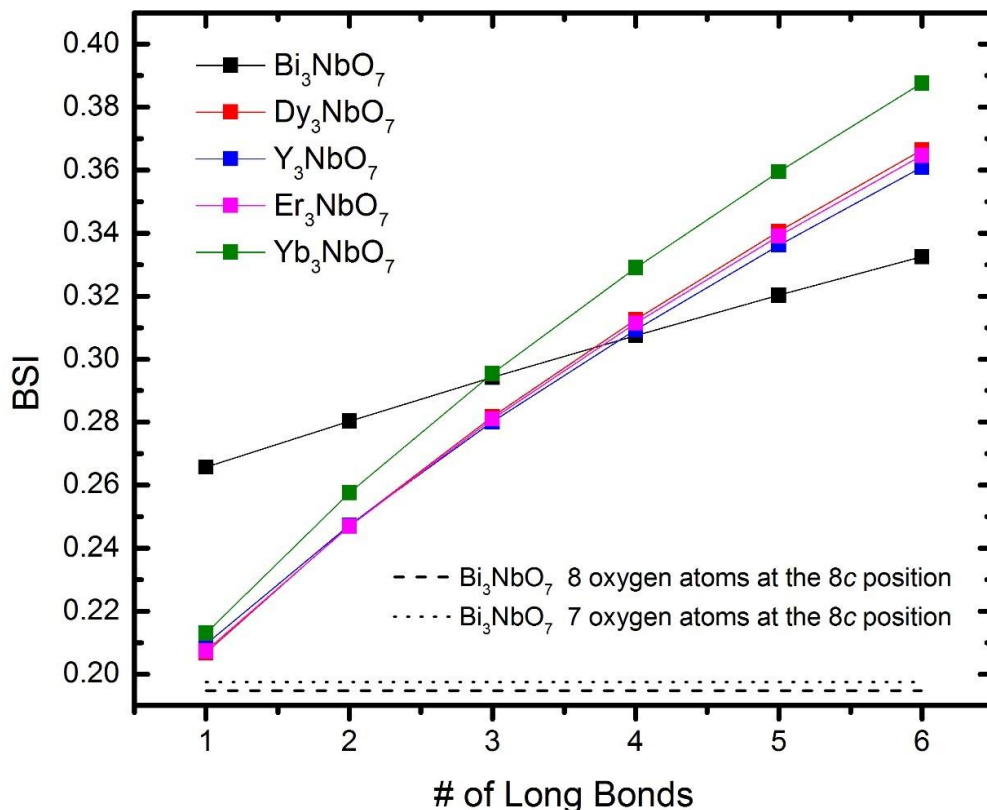


Figure 8-6. BSI of Ln_3NbO_7 and type-II Bi_3NbO_7 defect fluorite showing the possible bonding arrangements. The dashed and dotted lines represent Bi_3NbO_7 at the ideal fluorite position for comparison with the defect fluorite Bi_3NbO_7 structure.

While the Ln_3NbO_7 follows the same general trend with the GII decreasing as the number of long bonds decreases, type-II Bi_3NbO_7 does not follow the expected trend shown by the other defect fluorites. In fact, type-II Bi_3NbO_7 displays a minimum GII near three long bonds. This coincides with a BVS of ~ 4 which is higher than the ideal value of 3. Moving to a more favored BVS would lead to a cost in both BSI and GII .

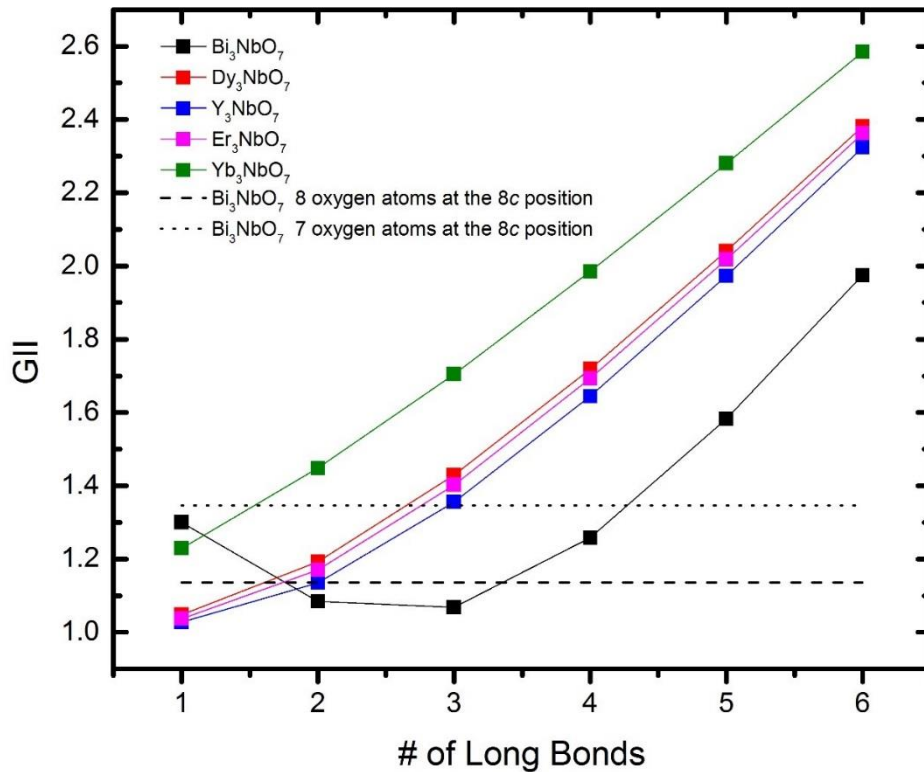


Figure 8-7. GII of Ln_3NbO_7 and type-II Bi_3NbO_7 defect fluorite showing the possible bonding arrangements. The dashed and dotted lines represent Bi_3NbO_7 at the ideal fluorite position for comparison with the defect fluorite Bi_3NbO_7 structure.

The Nb atom also plays a role in determining the behavior of the GII, which takes a look at the entire bonding environment. Since stabilized in a defect fluorite structure, the Nb atoms are located in the same crystallographic position as the Bi atoms, with the main difference being the oxidation state of Nb (+5). The BVS of the Nb atom also shows a similar trend to that shown in Figure 8-5, this is due to the fact that the only difference in the BVS calculation is the value empirical parameters R_0 and B . However, unlike the Bi atom, Nb would prefer a BVS of 5 to match the oxidation state of Nb. In the ideal fluorite structure the BVS of the Nb is 3.58 which is much lower than the preferred value of 5. By adopting a defect fluorite structure with 2 long bonds the BVS of the Nb atom increases to 4.23.

The GII of the defect fluorite structure of type-II Bi_3NbO_7 shows that the structure is most stable at 2-3 number of long bonds, at this point BVS of the Nb atom is closer to its ideal value than the Bi site. It has been proposed by Castro *et al.* that type-II Bi_3NbO_7 rearranges its structure in order to both satisfy the coordination of both the Bi and Nb atoms. In this configuration, the Nb atoms are in a classical oxygen octahedron and the Bi atoms are in a wide variety of oxygen polyhedra distorted by the stereochemical influence of its lone pair.¹³⁶

8.4 Conclusion

The dielectric properties of type-II Bi_3O_7 single crystal were investigated as a function of frequency and temperature. The dielectric response of type-II Bi_3NbO_7 follows the same behavior as the Ln_3NbO_7 defect fluorite series, where the real part of the permittivity decreases with decreasing temperature. Due to the fact that bismuth is highly polarizable it displays a permittivity of 85 at room temperature (1 MHz). The dielectric behavior as a function of frequency was also investigated and the onset of electrical conduction was identified at around 473 K. The TCC of Ln_3NbO_7 decreases with increasing Ln^{3+} ionic radius and type-II Bi_3NbO_7 was found to be 1.53×10^3 ppm/ $^\circ\text{C}$ and followed the same general trend.

CHAPTER 9 DIELECTRIC RESPONSE AND PHASE TRANSITION OF Gd₃NbO₇

9.1 Introduction

Weberite-type Ln₃BO₇ compounds (where Ln³⁺ is a rare earth element and *B* is Os⁵⁺, Re⁵⁺, Ru⁵⁺, Re⁵⁺, Mo⁵⁺, Ir⁵⁺, Sb⁵⁺, Nb⁵⁺, or Ta⁵⁺) attract great attention because they exhibit interesting properties including magnetic¹³⁷⁻¹³⁹, dielectric^{140,141}, as well as photocatalytic activity¹⁴²⁻¹⁴⁴. Gd₃NbO₇ belongs to this weberite-type family where the BO₆ are corner linked to each other and form chains of BO₆ octahedra with parallel chains of LnO₈ distorted cubes.

The crystal structure of Gd₃NbO₇ was first determined by Rossell *et al.*¹⁴⁵ and assigned a space group of C222₁ at room temperature. Gd₃NbO₇ undergoes a phase transition at about 340K, which is commonly observed in the Ln₃BO₇ family¹⁴⁶⁻¹⁴⁸. The existence of a transition has been confirmed through heat capacity measurements¹⁴⁹ and Raman spectroscopy¹⁵⁰. There are conflicting reports on the phase transition that occurs in Gd₃NbO₇, it has been suggested that the transition was between *Cmm2* to *Cmmm* without any proof. In a more recent study⁷⁵ high resolution X-ray diffraction (XRD) was performed, along with heat capacity and second harmonic generation proposed a phase transition from a centrosymmetric space group *Cmcm* with a transition below 340 K into a non-centrosymmetric structure with space group *Cm2m*.

However the proposed low temperature phase of *Cm2m* is a distinct anomaly when compared to other Weberite-type Ln₃NbO₇, where the phase transition goes from *Cmcm* to C222₁.¹³⁷ The difference between the C222₁ space group and *Cm2m* are nearly identical when looking at XRD data alone. Therefore, in this Chapter the low temperature structure debate of Gd₃NbO₇ will be resolved by examining its IR behavior,

high resolution XRD, and a comparison of the dielectric response of Gd_3NbO_7 to Gd_3TaO_7 .

9.2 Results and Discussion

The dielectric behavior of Gd_3NbO_7 as a function of temperatures at fixed frequencies from 1 kHz to 1MHz is shown in Figure 9-1. The real part of the permittivity is between 30 and 44 and the imaginary part of permittivity is on the order of 10^{-4} to 10^{-1} at 1 MHz from 25 K to 400 K.

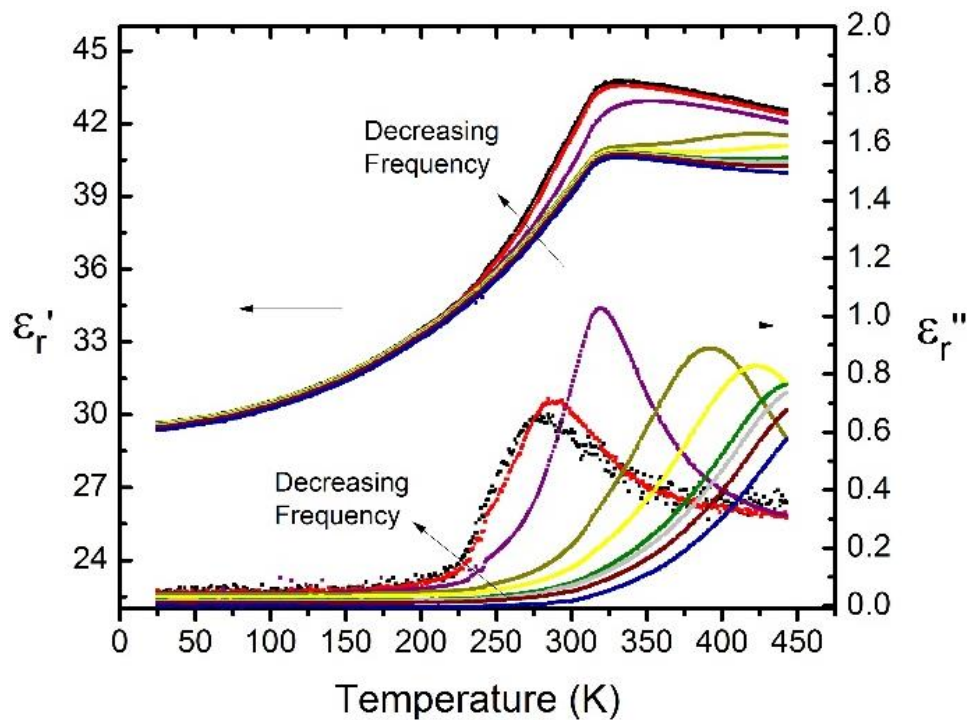


Figure 9-1. Real and imaginary components of the permittivity of Gd_3NbO_7 from 500 Hz to 2 MHz

It is observed that the dielectric response undergoes a frequency and temperature dependent dielectric relaxation behavior. The real part of the relative permittivity of Gd_3NbO_7 becomes more dispersive with increasing temperature, increasing sharply from 25 K to ~ 325 K where a maximum is reached. The temperature at the peaks of the imaginary components occur (T_m) shift to higher temperatures with

increasing frequency. This shift in the imaginary component of the permittivity is similar to those observed in Bi-pyrochlores, such as BZN, which are undergoing dielectric relaxation. However, unlike the typical Bi-pyrochlore relaxation behavior there is no clear shift in the maxima of the real part of the relative permittivity. To better understand the phenomena, the Arrhenius function is used to model the relaxation behavior of Gd_3NbO_7 :

$$v_r = v_0 \exp\left(\frac{-E_a}{k_B T_m}\right) \quad (9-1)$$

where v_r is the measuring frequency, the pre-exponential v_0 is the attempt jump frequency, E_a the activation energy and k_B is the Boltzmann's constant. T_m is determined by fitting the imaginary part of the permittivity for each frequency measured to a Gaussian function. The non-symmetric tails of the peaks are cut off during fitting.

The resulting Arrhenius plot is presented in Figure 9-2. From the linear fit, $v_0 = 1.12 \times 10^{11}$ Hz, and the activation energy E_a is 0.439 eV, which is larger than the typical values observed in Nb-based pyrochlores and relaxor ferroelectrics.^{151,152} However, other ionic and dipolar compound systems have even higher activation energies; for example, 0.53 eV for CaF_2 doped NaF and 1.02 eV for $(\text{Ba}_{0.8}\text{Sr}_{0.2})(\text{Ti}_{1-x}\text{Zr}_x)\text{O}_3$.^{153,154} Thus, the calculated activation energy is within an acceptable level.

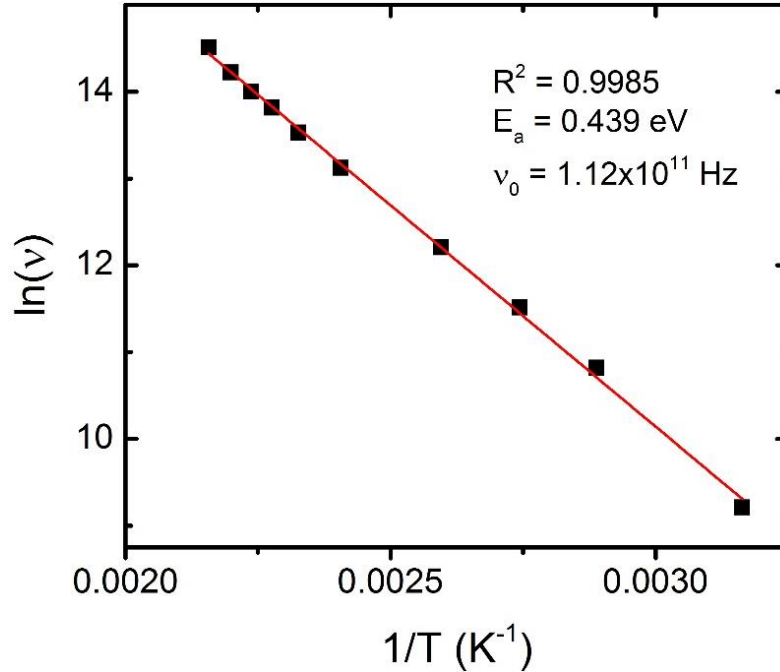


Figure 9-2. Arrhenius plot of temperature at which the maximum loss peak occurs in Gd_3NbO_7

While very similar to the dielectric relaxation discussed in Chapter 5 the lack of dispersion in the real part of the permittivity points to a possible phase transition which has been studied in other similar weberites such as Ln_3IrO_7 ,¹⁵⁵ Ln_3MoO_7 ,¹⁵⁶ and Ln_3RuO_7 .¹⁵⁷

The specific heat was measured by Cai *et al.* (Figure 9-3) showed a phase transition between 310 and 340 K. Approaching the structural phase transition, there is a divergence of the specific heat. This transition is consistent with a second order phase transition.

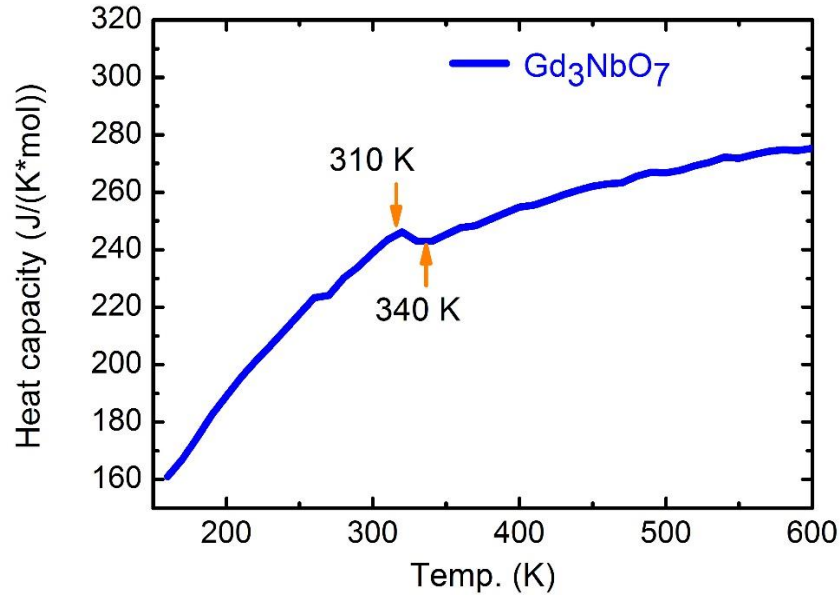


Figure 9-2. Heat capacity of Gd_3NbO_7 . Adapted from Cai *et al.*

Infrared spectroscopy as a function of temperature was performed at Professor Kamba's lab at the Institute of Physics of the ASCR, Czech Republic. There is a peak at $\sim 450\text{ cm}^{-1}$ that disappears above the phase transition temperature (Figure 9-3)

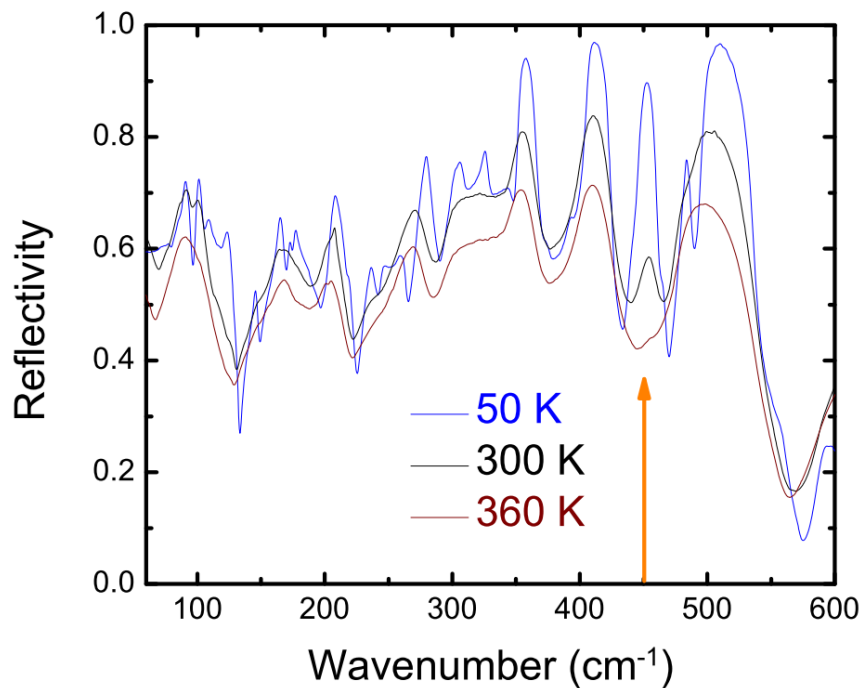


Figure 9-3. Infrared Spectroscopy of Gd_3NbO_7 at 50 K, 300 K, and 360 K. The arrow indicates the mode disappearing above the transition temperature.

A comparison of the crystal data and structural refinements of synchrotron XRD is shown in Table 9-1 for the previously proposed low temperature structure *Cm2m* (from Cai *et al.*) and the alternative *C222₁*.

Table 9-1. Crystal data and refinement parameters of the two proposed low temperature Gd_3NbO_7

Space Group	<i>Cm2m</i>	<i>C222₁</i>
Temperature	295 K	295 K
Lattice parameters	7.5324 Å 10.6108 Å 7.5327 Å	7.5342 Å 10.6185 Å 7.5461 Å
Z	4	4
λ (Å)	0.414201	0.414201
Refined 2θ range (deg)	0.5 ~ 29.999	0.5 ~ 29.999
No. of peaks	404	404
No. of parameters refined	71	65
R_{wp} (%)	10.39	12.14
R_p (%)	7.93	9.57
GOF (X^2)	5.169	9.104

Both of the refinements for Gd_3NbO_7 provide a satisfactory fit, while *Cm2m* has a lower X^2 the refinement needed more fitting parameters than *C222₁*. Ideally neutron diffraction would be used to compliment the synchrotron XRD results but Gd poses a significant challenge due to its extremely high neutron absorption. Transmission electron microscopy was also used to try to differentiate between the two space groups but the difficulty in identifying a mirror from a two-fold rotation proved inconclusive.

In an effort to identify the correct low temperature phase of Gd_3NbO_7 a similar well known Gd-weberite was synthesized, Gd_3TaO_7 . The key aspect of this weberite is the fact that it undergoes a transition from *Cmcm* to *C222₁*.¹⁵⁸⁻¹⁶⁰ The dielectric properties of Gd_3TaO_7 have not been reported and a comparison of its dielectric

response at the phase transition temperature to that of Gd_3NbO_7 could prove the link to understanding the phase transition of Gd_3NbO_7 .

The dielectric behavior of Gd_3TaO_7 as a function of temperatures at fixed frequencies from 1 kHz to 1MHz is shown in Figure 9-4. The real part of the permittivity is between 25 and 33 and the imaginary part of permittivity is on the order of 10^{-4} to 10^{-1} at 1 MHz from 25 K to 300 K.

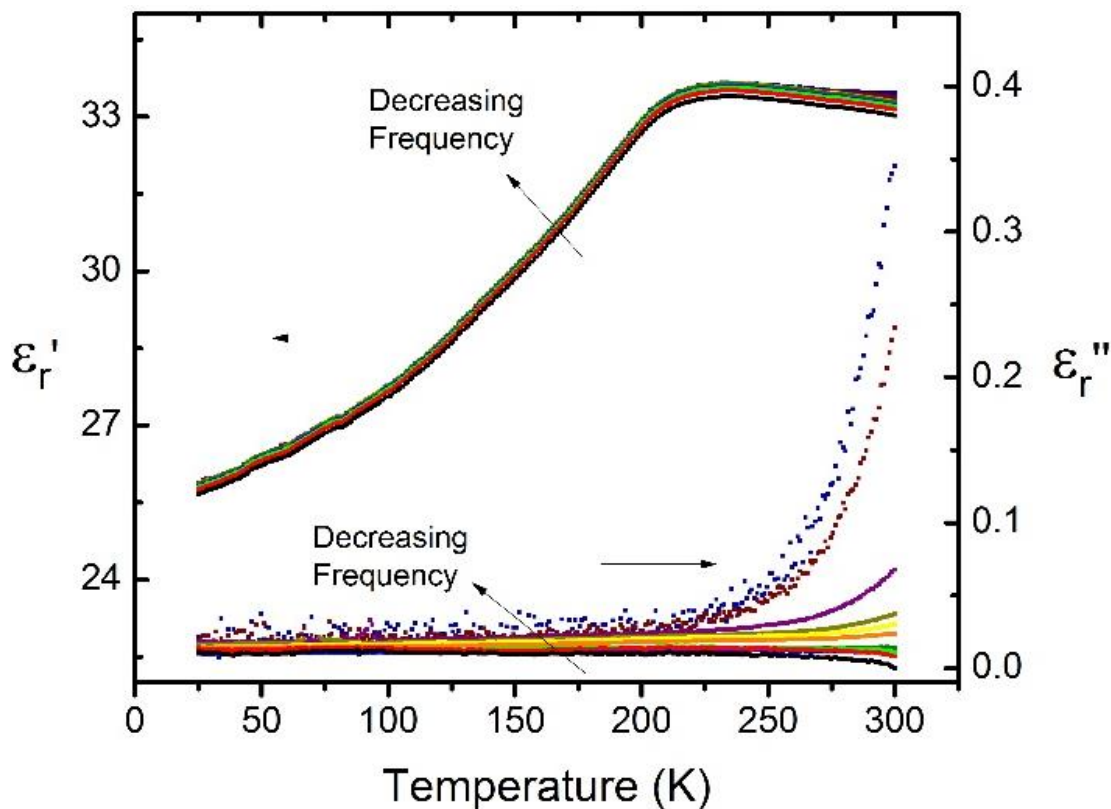


Figure 9-4. Imaginary and real part of the permittivity as a function of temperature from 500 Hz to 2 MHz of Gd_3TaO_7

Comparing the dielectric response of Gd_3TaO_7 (Figure 9-4) to that of Gd_3NbO_7 (Figure 9-1) reveals some interesting differences. The permittivity of Gd_3TaO_7 is ~ 25% lower than to that of Gd_3NbO_7 , which is to be expected as the dipolar polarizability of Nb is about 20 % higher than that of Ta.¹⁶¹ More importantly, however, is the behavior of the permittivity and loss at the phase transition temperatures. Both Gd_3TaO_7 and

Gd₃NbO₇ exhibit a sharp decrease in permittivity near the phase transition temperature, however, the major difference is found in the imaginary part of the permittivity. Gd₃NbO₇ has peaks in the imaginary component of the permittivity, where the maximum increases in temperature with increasing frequency, similar to dielectric relaxation in pyrochlores. On the other hand, Gd₃TaO₇, does not have any imaginary component anomaly while passing through the transition point from *Cmcm* to *C222*₁. This difference may provide the key for understanding the nature of the dielectric transition in Gd₃NbO₇, the difference in the dielectric behavior of Gd₃TaO₇ (*Cmcm* → *C222*₁) shows no accompanying loss peaks. The loss anomaly in Gd₃NbO₇ combined with IR, SHG, and XRD data all support a different transition to that seen in Gd₃TaO₇, the choice of *Cm2m* over *C222*₁ also generates a net dipole in the structure due to the displacements of the Nb⁵⁺ and Gd³⁺ ions along the [010]⁷⁵ which is not observed in Gd₃TaO₇ and may in fact lead to difference in the dielectric response.

9.3 Conclusion

The dielectric behavior of Gd₃NbO₇ was characterized as a function of temperature, the origin of the dielectric relaxation type behavior is ascribed to the phase transition. The imaginary component of the permittivity was fit to the Arrhenius function and an activation energy of 0.439 eV was obtained.

Second harmonic generation (SHG), heat capacity measurements and IR indicated a phase transition in Gd₃NbO₇ at about 340 K. The lambda-shape specific heat capacity near the phase transition suggests a 2nd order nature of the phase transition. High resolution XRD was performed by Lu Cai at 100 K, 295 K, 345 K and 400 K and confirmed a phase transition. The high temperature phase was refined to

Cmcm while significant controversy remained over the low temperature phase between *C222*₁ and *Cm2m* due to their nearly identical XRD refinement.

The dielectric behavior of Gd_3TaO_7 was characterized as a function of temperature, at the phase transition point the real part of the permittivity exhibit a sharp decrease as a function of temperature. Unlike Gd_3NbO_7 , Gd_3TaO_7 does not display peaks in the imaginary component of the permittivity, the phase transition of Gd_3TaO_7 is known to go from the *Cmcm* to *C222*₁. The difference in the dielectric loss response of Gd_3TaO_7 and Gd_3NbO_7 point to a different type of phase transition and the proposed polar group of *Cm2m* would account for the difference in the dielectric behavior.

CHAPTER 10 SUMMARY AND FUTURE WORK

10.1 Summary

The investigation for materials with high permittivity and low loss is necessary for the advancement of electronic components. The work reported in this thesis investigates the structure-dielectric properties of $\text{Bi}_2\text{Ti}_2\text{O}_7$ and defect fluorites, as well as uncovering the true cause for the dielectric relaxation phenomena in bismuth pyrochlores. Microwave sintering was used to sinter $\text{Bi}_2\text{Ti}_2\text{O}_7$ and dielectric spectroscopy, Raman and IR spectroscopy, and Neutron and HR-XRD as a function of temperature were performed and characterized for the first time in reported literature.

The structural characterization of $(\text{Sm}_x\text{Yb}_{1-x})_2\text{Ti}_2\text{O}_7$ and $\text{Sm}_2(\text{Sn}_x\text{Ti}_{1-x})_2\text{O}_7$ ($x = 0.25, 0.5, 0.75$) was presented here. It was found that both systems formed a phase pure pyrochlore phase and the presence of the (442) diffraction peak was not detected. Therefore, both of the Sm systems only have the presence of substitution and do not have atomic displacements found in most Bi-pyrochlores. A more in-depth structural study of $\text{Bi}_2\text{Ti}_2\text{O}_7$ was performed using neutron diffraction, synchrotron x-ray diffraction (SXR), and DFT. Both the neutron and SXR revealed displacements of the Bi cation to the 96g site and the displacement of the O' oxygen. The neutron and SXR both showed a better fit when vacancies were considered on the Bi and O(1) site, the energy of formation of non-stoichiometric $\text{Bi}_2\text{Ti}_2\text{O}_7$ was found to be 3.13 eV at room temperature.

A dielectric analysis of $\text{Bi}_2\text{Ti}_2\text{O}_7$ ceramic, a bismuth pyrochlore without substitutional disorder, revealed considerable differences with respect to the common dielectric behavior exhibited by this family of compounds. The dielectric relaxation

observed in BZN is absent in $\text{Bi}_2\text{Ti}_2\text{O}_7$; however, a relaxation of a different nature was found at low frequencies (<10 kHz) and at relatively high temperature (125 K) in $\text{Bi}_2\text{Ti}_2\text{O}_7$. The calculated activation energy and characteristic frequency of this behavior using the Arrhenius model were 0.162 eV and ~ 1 MHz, respectively. The low attempt jump frequency is consistent with space charge polarization and not the result of dipolar or ionic disorder. The relaxation behavior at low frequency was confirmed with a study of the electrical modulus, $\tan \delta$, admittance, and impedance as a function of frequency. The atypical dielectric response of $\text{Bi}_2\text{Ti}_2\text{O}_7$ suggests that substitutional cations (rather than ionic displacements, or lone pair electrons), play a major role in the origin of the dielectric relaxation in pyrochlores. A dielectric analysis of the $(\text{Sm}_x\text{Yb}_{1-x})_2\text{Ti}_2\text{O}_7$ and $\text{Sm}_2(\text{Sn}_x\text{Ti}_{1-x})_2\text{O}_7$ ($x = 0.25, 0.5, 0.75$) systems, pyrochlores without atomic displacements, revealed no evidence of dielectric relaxation to that observed in BZN. These responses suggest that substitutional cations

The Raman spectra of the pyrochlore $\text{Bi}_2\text{Ti}_2\text{O}_7$ was measured on both calcined powder and sintered ceramic. Raman modes were assigned by comparison to other bismuth and titanate pyrochlores found in literature, $\text{Bi}_2\text{Ti}_2\text{O}_7$ displays evidence of displacive disorder in both the *A* and *B* site. A low frequency F_{1u} mode (normally IR-active) is assigned in the Raman spectra, due to the relaxation of the selection rules resulting from the displacement of the Bi atom from its ideal crystallographic position. Additionally, evidence of displacement in the Ti atomic position is provided by the atypical spectroscopic behavior of the Ti-O modes at the higher range of the Raman spectra. The IR spectra were fit to an oscillator model from which the real and imaginary parts of the dielectric function were obtained. The low frequency O-A-O and

O'-A-O' phonon modes are pushed to lower frequencies due to the large mass of the Bi ion. The appearance of the ω_n^{**} also indicates a disorder of the A site and O' displacement.

The dielectric properties of type-II Bi_3O_7 single crystal were investigated as a function of frequency and temperature. The dielectric response of type-II Bi_3NbO_7 follows the same behavior as the Ln_3NbO_7 defect fluorite series, where the real part of the permittivity decreases with decreasing temperature. Due to the fact that bismuth is highly polarizable it displays a permittivity of 85 at room temperature (1 MHz). The dielectric behavior as a function of frequency was also investigated and the onset of electrical conduction was identified at around 473 K. The TCC of Ln_3NbO_7 decreases with increasing Ln^{3+} ionic radius and type-II Bi_3NbO_7 was found to be 1.53×10^3 ppm/ $^\circ\text{C}$ and followed the same general trend.

The work presented in this dissertation adds a final link to the question of what conditions are required in pyrochlores to exhibit dielectric relaxation. An in depth investigation into the structure and dielectric properties of $\text{Bi}_2\text{Ti}_2\text{O}_7$ showed that a pyrochlore displaying atomic displacements without substitution does not display relaxation. This result points suggests that substitutional cations play a major role in the origin of dielectric relaxation in pyrochlores.

10.2 Future Work

A study into the local structure of $\text{Bi}_2\text{Ti}_2\text{O}_7$ through TEM would give further insight into the proposed correlated displacements of the Bi cation in $\text{Bi}_2\text{Ti}_2\text{O}_7$. The synthesis of dielectric thin films of $\text{Bi}_2\text{Ti}_2\text{O}_7$ would allow for a comparison of the properties with bulk $\text{Bi}_2\text{Ti}_2\text{O}_7$. Raman measurements as a function of temperature of $\text{Bi}_2\text{Ti}_2\text{O}_7$ would also compliment the already measure IR data. An investigation into the dielectric properties

at microwave frequencies for all the pyrochlores synthesized in this work would shed some light on the microwave dielectric properties of the synthesized pyrochlores.

APPENDIX A EQUIVALENT CIRCUIT ANALYSIS OF $\text{Bi}_2\text{Ti}_2\text{O}_7$

A.1. Introduction

Compounds with the nominal composition $\text{A}_2\text{B}_2\text{O}_7$ containing the B_2O_6 octahedral and the $\text{A}_2\text{O}'$ tetrahedral sub-structures are known as pyrochlores. Bismuth based pyrochlores have been extensively studied due to their attractive composition-dependent dielectric properties.^{12,13,20-24,71,162} A combination of high permittivity values (usually above 100), low dielectric loss, and low sintering temperatures ($1000^\circ\text{C} \pm 150$) makes them good materials for dielectric components for embedded capacitors and multilayer ceramic capacitors (MLCC).

The recent findings presented in Chapter 5 showed that $\text{Bi}_2\text{Ti}_2\text{O}_7$ did not display typical bismuth pyrochlore relaxation, as seen in $\text{Bi}_{1.5}\text{Zn}_{0.92}\text{Nb}_{1.5}\text{O}_{6.92}$ (BZN), a relaxation of a different nature was found at low frequencies ($<10\text{kHz}$) and at relatively high temperatures (125 K) in $\text{Bi}_2\text{Ti}_2\text{O}_7$. The calculated low attempt jump frequency of ~ 1 MHz is consistent with space charge polarization.

Equivalent circuit analysis provides a good basis for the understanding of the electrical behavior as physical processes can be assigned to capacitor (C), resistor (R), and constant phase elements (CPE) components. Recently, the electrical properties of both bismuth zinc niobate titanate (BZNT)¹⁶³ and BZN¹⁶⁴ have been characterized using equivalent circuit analysis by Osman and coworkers in an effort to understand the origin of the relaxor-like behavior displayed by both BZNT and BZN.

The main objective is to characterize the space charge dielectric relaxation behavior of $\text{Bi}_2\text{Ti}_2\text{O}_7$ using equivalent circuits that model the impedance data from room

temperature to 30 K, in order to provide a model of the electrical response of $\text{Bi}_2\text{Ti}_2\text{O}_7$ compared to other pyrochlores that display typical Bi-pyrochlore relaxation behavior.

A.2. Equivalent Circuit Analysis

Equivalent circuit analysis is commonly used to model impedance spectroscopy data in terms of ideal circuit elements (R,L, and C). The circuit elements are commonly used to provide a physical interpretation of the electrical response of the material¹⁶⁵. Recently, Osman and West have applied equivalent circuit analysis to relaxor ceramics in order to further characterize and understand the nature of dielectric relaxation in ceramics^{166,167}. There has not, however, been an equivalent circuit that models dielectric relaxation due to space charge polarization.

In order to find an appropriate equivalent circuit response the experimental capacitance, C' , data extracted from the impedance measurements is shown as a function of frequency for a selection of temperatures over the range of 30K to 300K in Figure A-1. At low temperatures, 30K-180K, the C' data shows a slight dispersion to lower values with increasing frequency. Temperatures between 190K-300K display an increase of C' as the frequency decreases, the onset of the increase shifts towards higher frequencies as the temperature increases. This increase in capacitance is most likely due to the relaxation event occurring at lower frequencies at these temperatures, shown in Chapter 5.

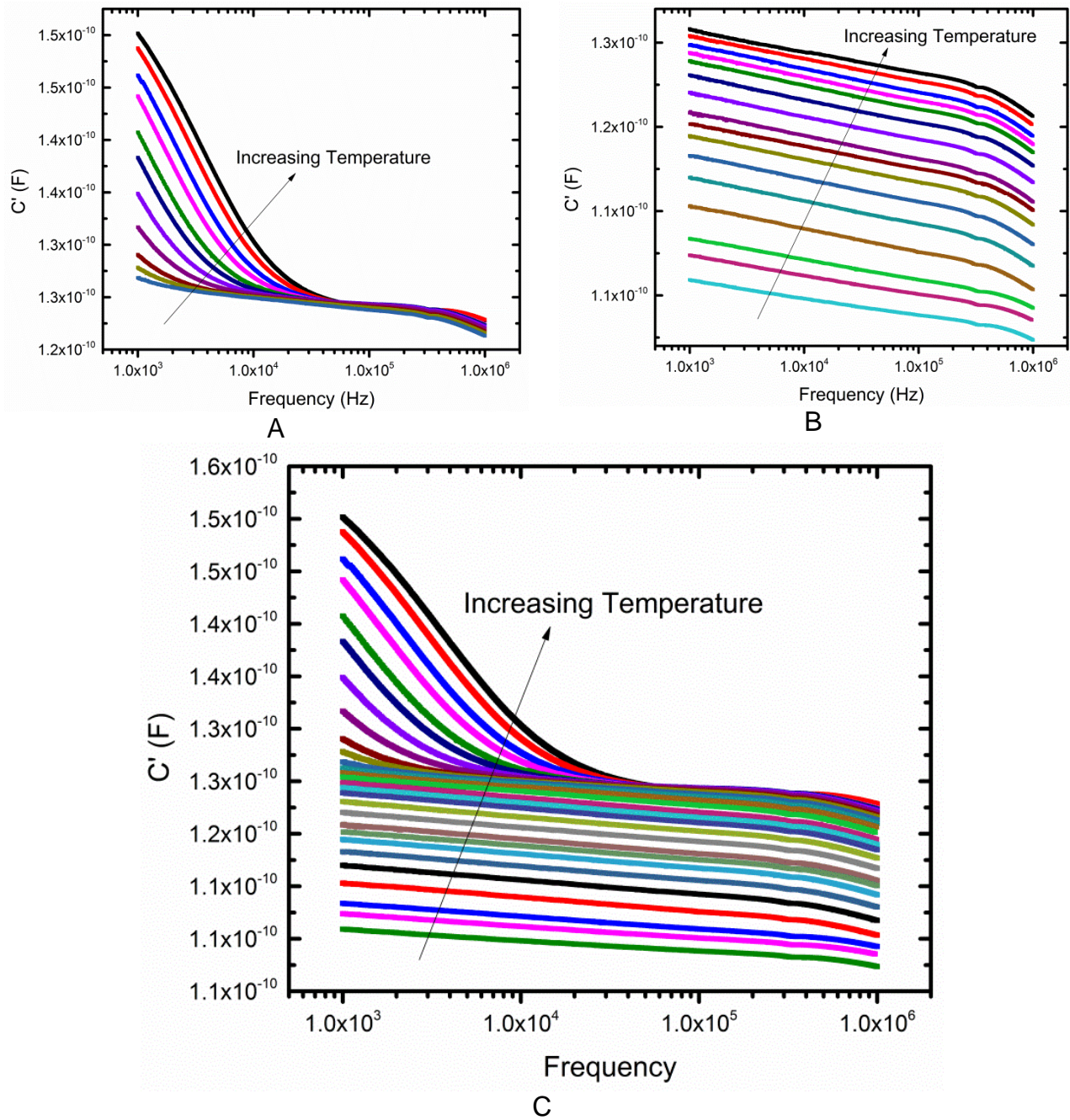


Figure A-1. Capacitance, C' vs frequency for A) 300K-190K, B) 190K-30K and C) 300K-30K.

Admittance, Y' , data was also extracted from impedance measurements and is shown from the temperature range of 30 K - 300 K against frequency on logarithmic scales in Figure A-2. The data below 170 K show a frequency-dependent admittance

with an approximately linear, power law dependence with a slope $n \approx 1.14$ at 70 K. As temperature decreases the Y' values also decrease, however, at temperatures above 190 K there is an increase in Y' at lower frequency. This increase can also be ascribed to the low frequency, moderate temperature relaxation occurring in $\text{Bi}_2\text{Ti}_2\text{O}_7$.

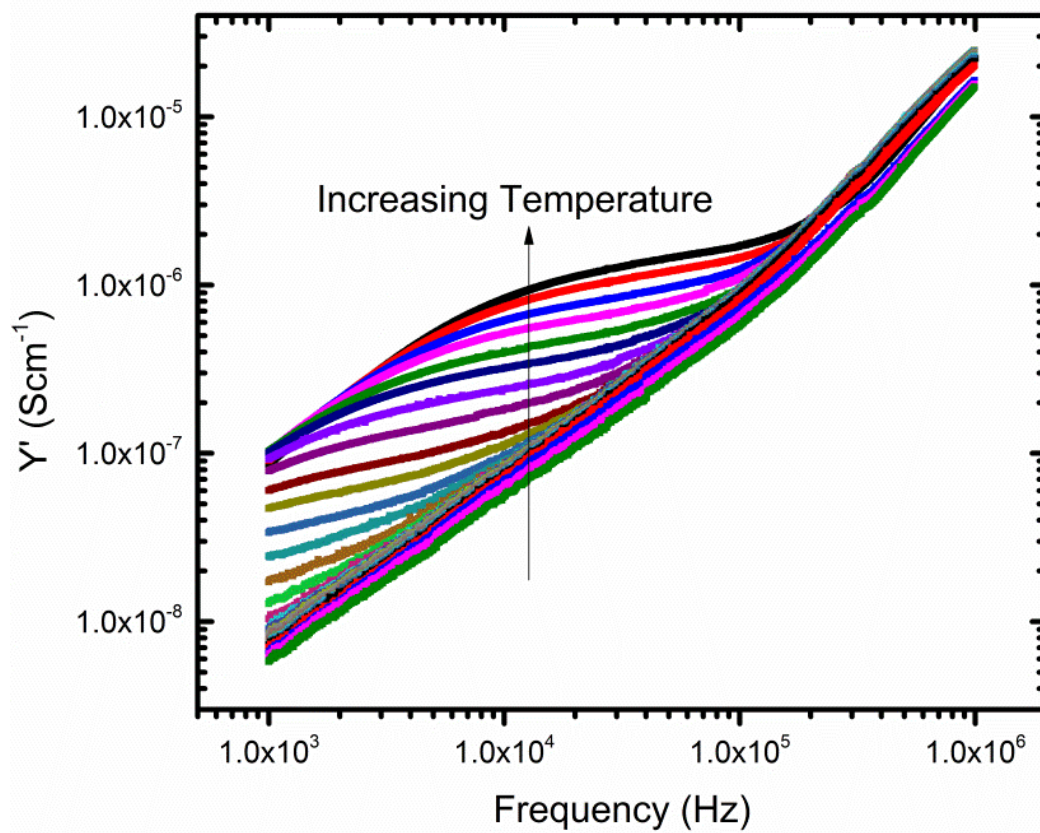


Figure A-2. Admittance, Y' vs frequency for 30K-300K

From the data shown in Figure A-2 there are two different responses as the temperature decreases. From 300K-190K there is low frequency relaxation which can be modeled by the equivalent circuit shown in Figure A-3A, this circuit is similar to what Osman and West proposed for $(\text{Bi}_{1.5}\text{Zn}_{0.5})(\text{Nb}_{0.5}\text{Ti}_{1.5})\text{O}_7$ relaxation process¹⁶⁶ but in $\text{Bi}_2\text{Ti}_2\text{O}_7$ an extra R and C element are added in parallel to model the loss of capacitance at higher frequencies.

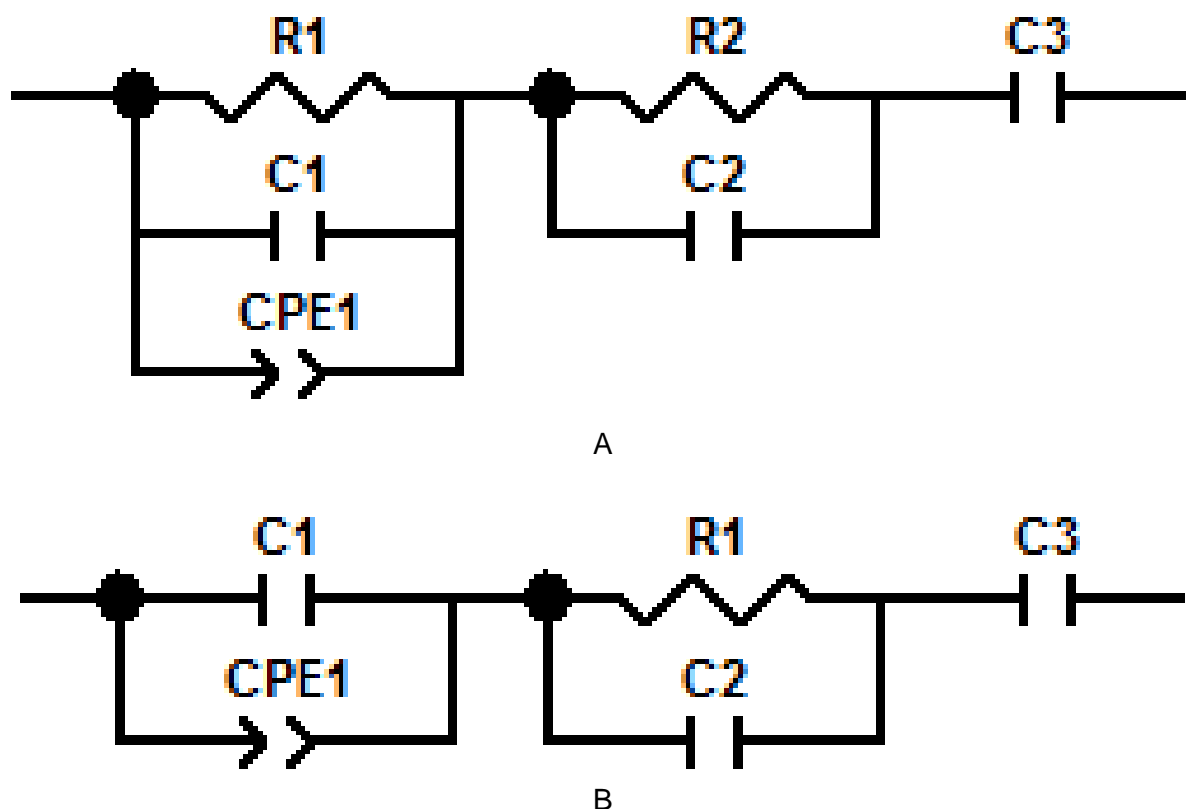
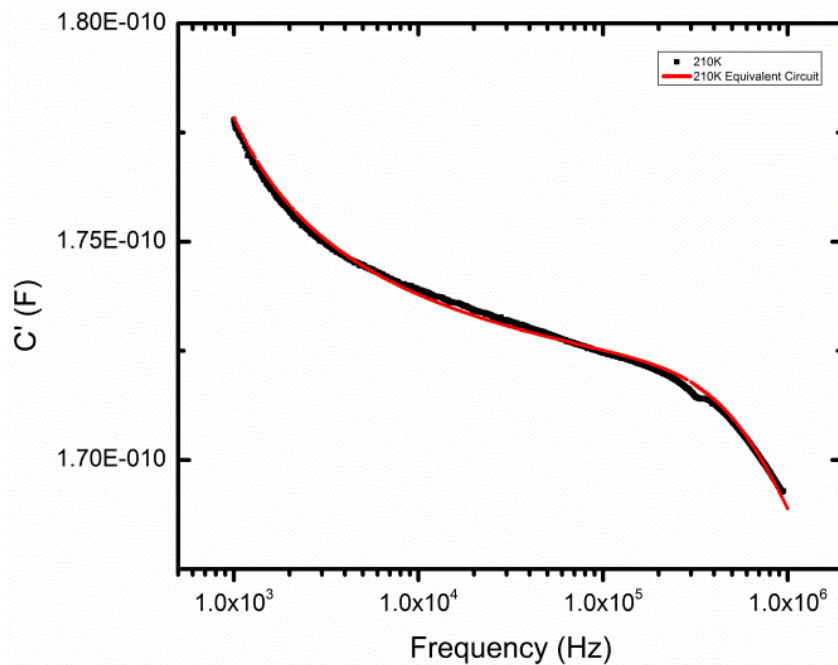


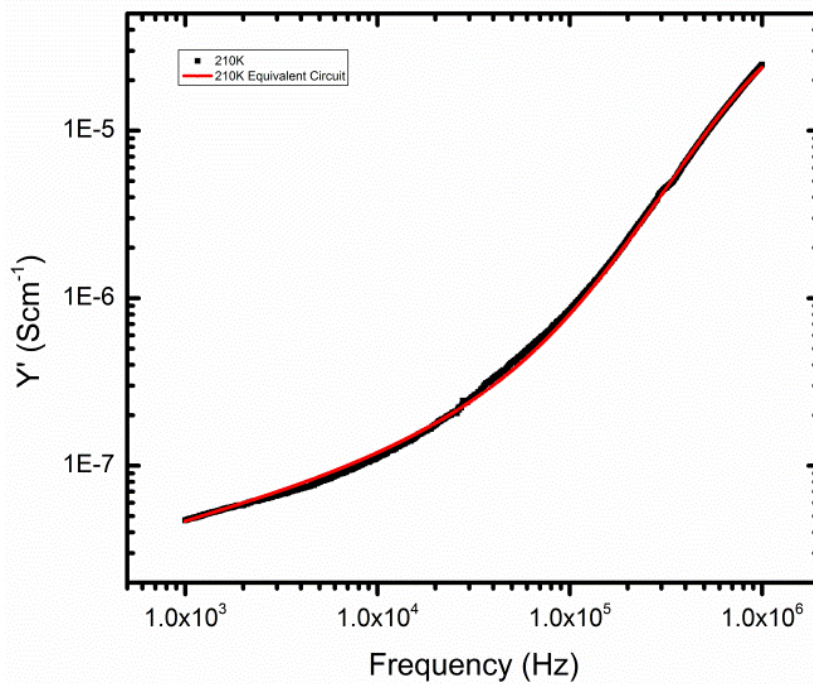
Figure A-3. Equivalent circuit showing different R, C, and CPE combinations

Figure A-4 shows the capacitance and admittance data and the fit of the equivalent circuit at 210K.

As the temperature drops below 190K the relaxation event occurring at low frequencies is no longer evident (Figure A-3A), therefore R₁ was eliminated from the circuit and the CPE was maintained due to the linear power law dependence with a slope greater than 1 is still exhibited at temperatures below 180K. Figure A-5 shows the equivalent circuit fit at 110K using the equivalent circuit from Figure A-3B.

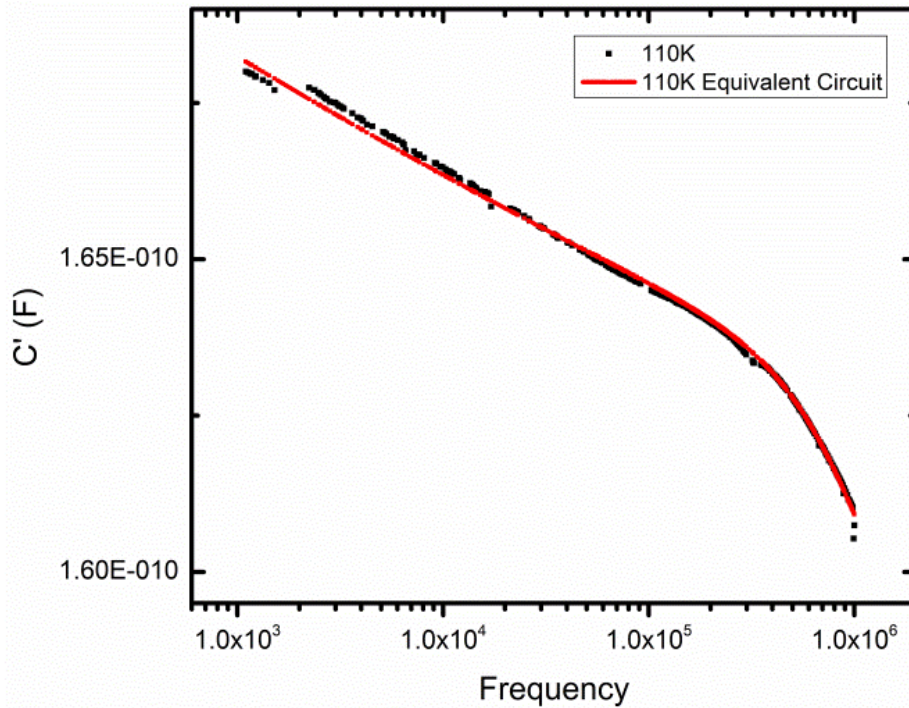


A

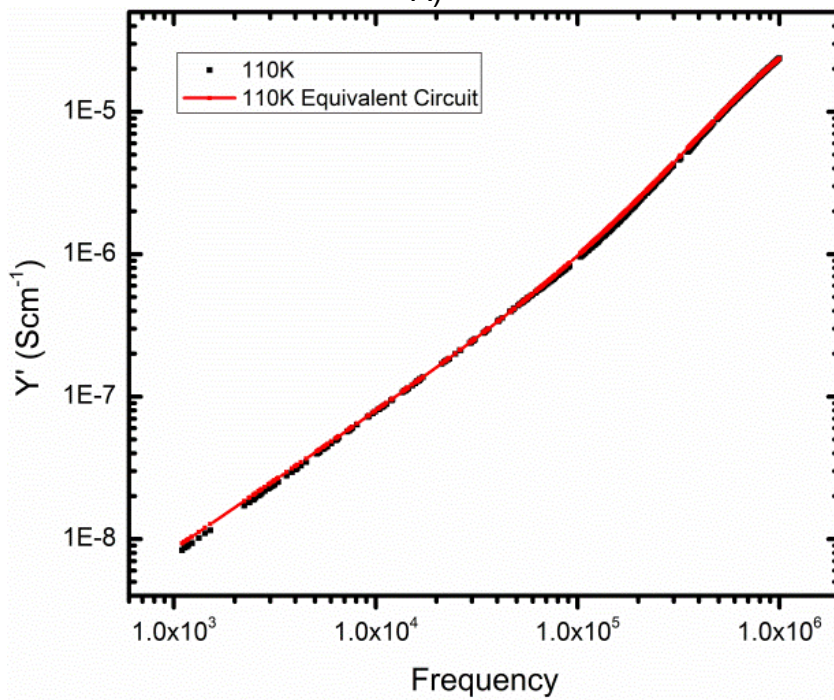


B

Figure A-4. Fit of the 210K to circuit in Figure A-3A for A) C' and B) Y'



A)



B

Figure A-5. Fit of the 210K to circuit in Figure A-3B for A) C' and B) Y'

The equivalent circuits give a potential insight into the electrical response of dielectric relaxation. Due to the frequency dispersions that are shown in Y' and C' spectroscopic plots the equivalent circuit cannot be fit using only R and C components

alone, and by introducing a constant phase element (CPE) into both equivalent circuits a good fit is observed. The circuit, Figure A-3A, is a proposed circuit model for dielectric relaxation due to space charge polarization.

APPENDIX B
Bi₂Ti₂O₇ TEMPERATURE EFFECTS ON STRUCTURE AND DIELECTRIC
PROPERTIES

The data presented in this dissertation along with low temperature heat capacity are all presented as a function of temperature. Figure B-1 attempts to show the low temperature anomalies in each dataset (permittivity, neutron, heat capacity) and show any correlation between the structure/phase changes and dielectric properties.

Both the neutron and specific heat capacity (C_p) performed at low temperatures revealed an anomaly. The lattice saturation at low temperatures discussed in Chapter 4 occurs at 210 K and the specific heat shows a deviation at 127 K. When overlaying these anomalies on the dielectric properties it is interesting to note that at 127 K is where the dielectric relaxation stops appearing in Bi₂Ti₂O₇. In fact the analysis as a function of frequency shows that under 130 K the relaxation behavior is no longer present. The lattice stiffening temperature of 210 K does not correlate with the dielectric or C_p measurements, however, at 127 K the lattice stiffening seems to be clearer indicating a possible correlation between the C_p , neutron, and dielectric permittivity.

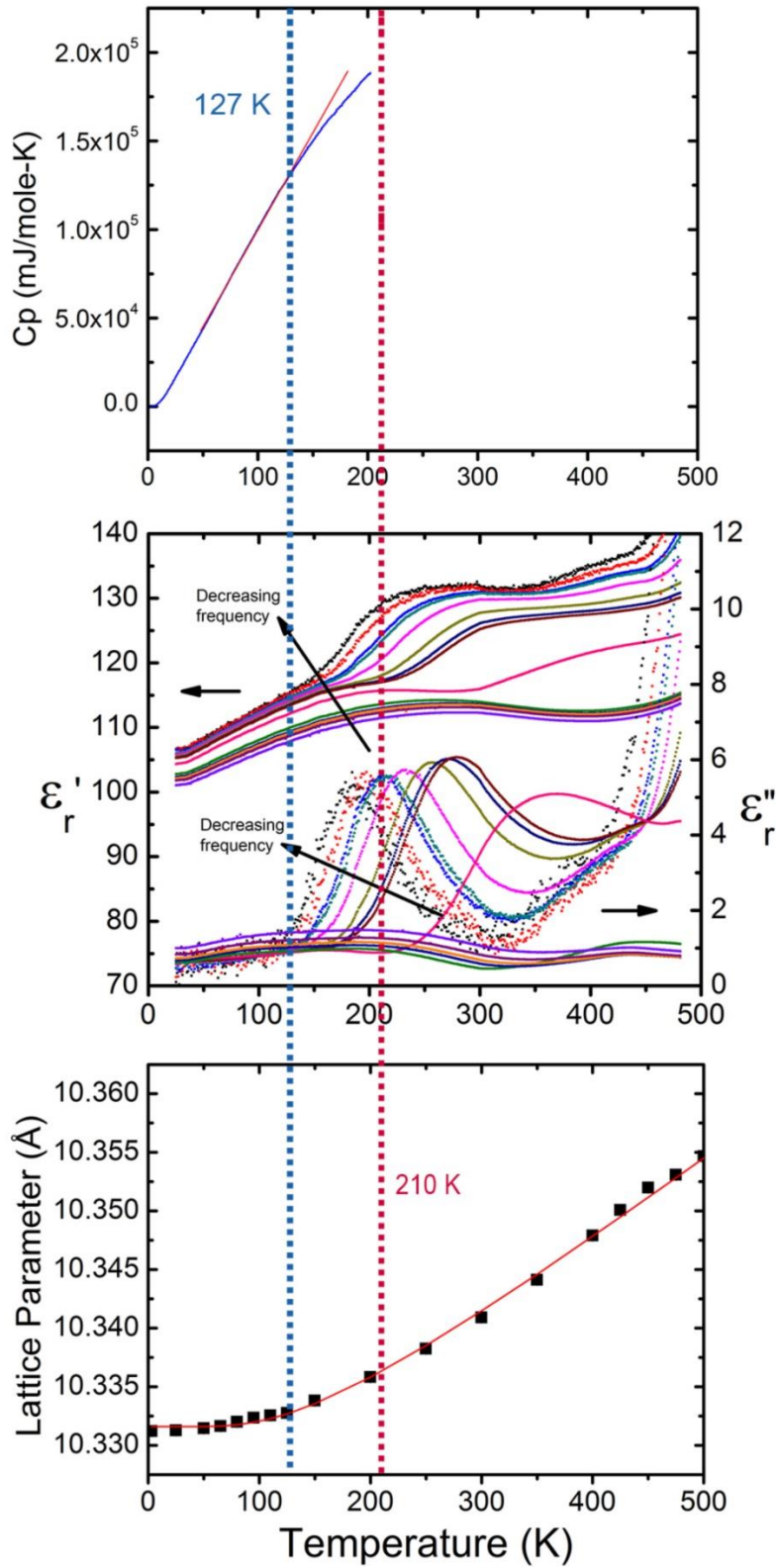


Figure B-1. A comparison of the temperature anomalies found in the specific heat, neutron diffraction and dielectric permittivity.

LIST OF REFERENCES

- 1 Kamba, S. *et al.* Anomalous broad dielectric relaxation in Bi_{1.5}Zn_{1.0}Nb_{1.5}O₇ pyrochlore. *Phys Rev B* **66**, doi:Artn 054106 (2002).
- 2 Levin, I. *et al.* Structural Study of an Unusual Cubic Pyrochlore Bi_{1.5}Zn_{0.92}Nb_{1.5}O_{6.92}. *Journal of Solid State Chemistry* **168**, 69-75, doi:10.1006/jssc.2002.9681 (2002).
- 3 Nino, J. C., Lanagan, M. T. & Randall, C. A. Phase formation and reactions in the Bi₂O₃-ZnO-Nb₂O₅-Ag pyrochlore system. *J Mater Res* **16**, 1460-1464, doi:Doi 10.1557/Jmr.2001.0203 (2001).
- 4 Jones, R. E., Jr. *et al.* Memory applications based on ferroelectric and high-permittivity dielectric thin films. *Microelectron. Eng.* **29**, 3-10, doi:10.1016/0167-9317(95)00106-9 (1995).
- 5 Keyes, R. W. Miniaturization of Electronics and Its Limits. *Ibm J Res Dev* **32**, 24-28 (1988).
- 6 Ahn, J. K., Cuong, N. D., Yoon, S. G. & Kim, C. S. Structural and electrical properties of Bi(1.5)Mg(1.0)Nb(1.5)O(7) thin films deposited on Pt/TiO(2)/SiO(2)/Si substrates by rf-magnetron sputtering. *J Vac Sci Technol B* **26**, 1277-1280, doi:Doi 10.1116/1.2932090 (2008).
- 7 Budianto, Y., Aoki, A. & Miyashita, T. Ultrathin polymer film capacitor composed of poly(N-alkylacrylamide) Langmuir-Blodgett films. *Macromolecules* **36**, 8761-8765, doi:Doi 10.1021/Ma034395t (2003).
- 8 Cai, L. & Nino, J. C. Complex ceramic structures. I. Weberites. *Acta Crystallogr B* **65**, 269-290, doi:Doi 10.1107/S0108768109011355 (2009).
- 9 Burggraaf, A. J., Vandijk, T. & Verkerk, M. J. Structure and Conductivity of Pyrochlore and Fluorite Type Solid-Solutions. *Solid State Ionics* **5**, 519-522, doi:Doi 10.1016/0167-2738(81)90306-4 (1981).
- 10 Mandal, B. P., Deshpande, S. K. & Tyagi, A. K. Ionic conductivity enhancement in Gd₂Zr₂O₇ pyrochlore by Nd doping. *J Mater Res* **23**, 911-916, doi:Doi 10.1557/Jmr.2008.0112 (2008).
- 11 Moon, P. K. & Tuller, H. L. Ionic-Conduction in the Gd₂ti₂o₇-Gd₂zr₂o₇ System. *Solid State Ionics* **28**, 470-474, doi:Doi 10.1016/S0167-2738(88)80085-7 (1988).
- 12 Kamba, S. *et al.* Anomalous broad dielectric relaxation in Bi_{1.5}Zn_{1.0}Nb_{1.5}O₇ pyrochlore. *Phys Rev B* **66**, 054106, doi:10.1103/PhysRevB.66.054106 (2002).

- 13 Nino, J. C., Lanagan, M. T. & Randall, C. A. Dielectric relaxation in Bi₂O₃-ZnO-Nb₂O₅ cubic pyrochlore. *J Appl Phys* **89**, 4512-4516, doi:Doi 10.1063/1.1357468 (2001).
- 14 Wang, H., Elsebrock, R., Waser, R. & Yao, X. Low temperature microwave properties of bismuth based dielectric ceramics. *Ferroelectrics* **327**, 33-37, doi:Doi 10.1080/00150190500316200 (2005).
- 15 Buixaderas, E., Kamba, S., Petzelt, J., Savinov, M. & Kolpakova, N. N. Phase transitions sequence in pyrochlore Cd₂Nb₂O₇ studied by IR reflectivity. *Eur Phys J B* **19**, 9-16, doi:DOI 10.1007/s100510170344 (2001).
- 16 Fischer, M., Malcherek, T., Bismayer, U., Blaha, P. & Schwarz, K. Structure and stability of Cd₂Nb₂O₇ and Cd₂Ta₂O₇ explored by ab initio calculations. *Phys Rev B* **78**, doi:Artn 014108 (2008).
- 17 Gardner, J. S., Gingras, M. J. P. & Greedan, J. E. Magnetic pyrochlore oxides. *Rev Mod Phys* **82**, 53-107, doi:DOI 10.1103/RevModPhys.82.53 (2010).
- 18 Gurgul, J., Rams, M., Swiatkowska, Z., Kmiec, R. & Tomala, K. Bulk magnetic measurements and Ru-99 and Gd-155 Mossbauer spectroscopies of Gd₂Ru₂O₇. *Phys Rev B* **75**, doi:Artn 064426 (2007).
- 19 Abe, R., Higashi, M., Sayama, K., Abe, Y. & Sugihara, H. Photocatalytic activity of R₃MO₇ and R₂Ti₂O₇ (R = Y, Gd, La; M = Nb, Ta) for water splitting into H₂ and O₂. *J Phys Chem B* **110**, 2219-2226, doi:Doi 10.1021/Jp0552933 (2006).
- 20 Banys, J., Ivanov, M., Rudys, S., Li, J. & Wang, H. Dielectric properties of cubic bismuth based pyrochlores containing lithium and fluorine. *J Eur Ceram Soc* **30**, 385-388, doi:10.1016/j.jeurceramsoc.2009.06.032 (2010).
- 21 Cann, D. P., Randall, C. A. & Shrout, T. R. Investigation of the dielectric properties of bismuth pyrochlores. *Solid State Commun* **100**, 529-534, doi:Doi 10.1016/0038-1098(96)00012-9 (1996).
- 22 Du, H. L., Yao, X. & Wang, H. Relaxor-like behavior of bismuth-based pyrochlores containing Sn. *J Electroceram* **21**, 222-225, doi:10.1007/s10832-007-9098-2 (2008).
- 23 Liu, Y. *et al.* Displacive disorder and dielectric relaxation in the stoichiometric bismuth-containing pyrochlores, Bi₂MIIIInbO₇ (M=In and Sc). *Journal of Solid State Chemistry* **182**, 2748-2755, doi:10.1016/j.jssc.2009.07.007 (2009).
- 24 Lufaso, M. W. *et al.* Phase formation, crystal chemistry, and properties in the system Bi₂O₃-Fe₂O₃-Nb₂O₅. *Journal of Solid State Chemistry* **179**, 3900-3910, doi:10.1016/j.jssc.2006.08.036 (2006).

- 25 Ang, C. *et al.* Low-temperature dielectric relaxation in the pyrochlore $(\text{Bi}_{3/4}\text{Zn}_{1/4})_2(\text{Zn}_{1/4}\text{Ta}_{3/4})_2\text{O}_7$ compound. *Appl Phys Lett* **80**, 4807-4809, doi:Doi 10.1063/1.1486045 (2002).
- 26 Esquivel-Elizondo, J. R., Hinojosa, B. B. & Nino, J. C. $\text{Bi}_2\text{Ti}_2\text{O}_7$: It Is Not What You Have Read. *Chemistry of Materials* **23**, 4965-4974, doi:10.1021/cm202154c (2011).
- 27 Christopher Turner, B. K., Beverly Hinojosa, Juan C Nino. Structure of $\text{Bi}_2\text{Ti}_2\text{O}_7$. *In preparation* (2014).
- 28 Turner, C. G., Esquivel-Elizondo, J. R., Nino, J. C. & Troiler-McKins, S. Dielectric Properties and Relaxation of $\text{Bi}_2\text{Ti}_2\text{O}_7$. *J Am Ceram Soc*, n/a-n/a, doi:10.1111/jace.12803 (2014).
- 29 Christopher Turner, P. J., Evan Thatcher, David Tanner, Juan C. Nino. Vibrational modes in $\text{Bi}_2\text{Ti}_2\text{O}_7$: Displacive Disorder Effects. *Phys Rev B* Submitted (2014).
- 30 Christopher Turner, B. E., Juan C. Nino. Dielectric Properties of Single Crystal type-II Bi_3NbO_7 . *Journal of Solid State Chemistry* Submitted (2014).
- 31 Christopher Turner, J. C. N. Gd_3NbO_7 revisited: structure dielectric response relationship. (2014).
- 32 Han, H. *et al.* Origin of colossal permittivity in BaTiO_3 via broadband dielectric spectroscopy. *J Appl Phys* **113**, doi:Artn 024102 (2013).
- 33 Mumme, W. G. *et al.* BiNb_3O_9 , a metastable perovskite phase with Bi/vacancy ordering: Crystal structure and dielectric properties. *Journal of Solid State Chemistry* **200**, 323-327, doi:DOI 10.1016/j.jssc.2013.01.052 (2013).
- 34 Subramanian, M. A., Aravamudan, G. & Rao, G. V. S. Oxide Pyrochlores - a Review. *Prog Solid State Ch* **15**, 55-143, doi:Doi 10.1016/0079-6786(83)90001-8 (1983).
- 35 Abe, R. *et al.* Photocatalytic water splitting into H_2 and O_2 over R_3TaO_7 and R_3NbO_7 (R = Y, Yb, Gd, La): Effect of crystal structure on photocatalytic activity. *J Phys Chem B* **108**, 811-814, doi:Doi 10.1021/Jp036300v (2004).
- 36 Rooksby, H. P. & White, E. A. D. Rare-Earth Niobates and Tantalates of Defect Fluorite-Type and Weberite-Type Structures. *J Am Ceram Soc* **47**, 94-96, doi:DOI 10.1111/j.1151-2916.1964.tb15663.x (1964).
- 37 Vente, J. F., Helmholtz, R. B. & Ijdo, D. J. W. The Structure and Magnetic-Properties of Pr_3Mo_7 with M=Nb, Ta, and Sb. *Journal of Solid State Chemistry* **108**, 18-23, doi:DOI 10.1006/jssc.1994.1003 (1994).

- 38 Cai, L. & Nino, J. C. Structure and dielectric properties of Ln(3)NbO(7) (Ln = Nd, Gd, Dy, Er, Yb and Y). *J Eur Ceram Soc* **27**, 3971-3976, doi:DOI 10.1016/j.jeurceram.2007.02.077 (2007).
- 39 Brown, I. D. *The chemical bond in inorganic chemistry : the bond valence model*. (Oxford University Press, 2002).
- 40 Brown, I. D. Recent Developments in the Methods and Applications of the Bond Valence Model. *Chem Rev* **109**, 6858-6919, doi:Doi 10.1021/Cr900053k (2009).
- 41 Brown, I. D. & Altermatt, D. Bond-Valence Parameters Obtained from a Systematic Analysis of the Inorganic Crystal-Structure Database. *Acta Crystallogr B* **41**, 244-247, doi:Doi 10.1107/S0108768185002063 (1985).
- 42 Kao, K. C. *Dielectric Phenomena in Solids*. (Elsevier Science, 2004).
- 43 Moulson, A. J. & Herbert, J. M. *Electroceramics: Materials, Properties, Applications*. (Wiley, 2003).
- 44 Debye, P. J. W. *Polar molecules*. (The Chemical Catalog Company, inc., 1929).
- 45 Nino, J. C., Lanagan, M. T., Randall, C. A. & Kamba, S. Correlation between infrared phonon modes and dielectric relaxation in Bi₂O₃-ZnO-Nb₂O₅ cubic pyrochlore. *Appl Phys Lett* **81**, 4404-4406, doi:Doi 10.1063/1.1524699 (2002).
- 46 Courtens, E. Vogel-Fulcher Scaling of the Susceptibility in a Mixed-Crystal Proton Glass. *Phys Rev Lett* **52**, 69-72, doi:DOI 10.1103/PhysRevLett.52.69 (1984).
- 47 Nguyen, H. B. *et al.* The disordered structures and low temperature dielectric relaxation properties of two misplaced-displacive cubic pyrochlores found in the Bi₂O₃-(MO)-O-II-Nb₂O₅ (M = Mg, Ni) systems. *Journal of Solid State Chemistry* **180**, 2558-2565, doi:DOI 10.1016/j.jssc.2007.07.003 (2007).
- 48 Vanderah, T. A., Guzman, J. & Nino, J. C. Stability Phase-Fields and Pyrochlore Formation in Sections of the Bi₂O₃-Al₂O₃-Fe₂O₃-Nb₂O₅ System. *J Am Ceram Soc* **91**, 3659-3662, doi:10.1111/j.1551-2916.2008.02648.x (2008).
- 49 Valant, M. *et al.* Pyrochlore Range from Bi₂O₃-Fe₂O₃-TeO₃ System for LTCC and Photocatalysis and the Crystal Structure of New Bi₃(Fe_{0.56}Te_{0.44})₃O₁₁. *J Am Ceram Soc* **95**, 644-650, doi:10.1111/j.1551-2916.2011.04801.x (2012).
- 50 Roth, R. S. *et al.* Pyrochlore formation, phase relations, and properties in the CaO-TiO₂-(Nb,Ta)₂O₅ systems. *Journal of Solid State Chemistry* **181**, 406-414, doi:DOI 10.1016/j.jssc.2007.12.005 (2008).

- 51 Rousseau, D. L., Bauman, R. P. & Porto, S. P. S. Normal Mode Determination in Crystals. *J Raman Spectrosc* **10**, 253-290, doi:DOI 10.1002/jrs.1250100152 (1981).
- 52 Colthup, N. *Introduction to Infrared and Raman Spectroscopy*. 2nd ed. edn, (Elsevier Science, 1975).
- 53 Larkin, P. *Infrared and raman spectroscopy principles and spectral interpretation*. (Elsevier, 2011).
- 54 Su, W. F. & Lu, Y. T. Synthesis, phase transformation and dielectric properties of sol-gel derived Bi₂Ti₂O₇ ceramics. *Mater Chem Phys* **80**, 632-637, doi:Doi 10.1016/S0254-0584(03)00089-0 (2003).
- 55 Wang, J. *et al.* A dedicated powder diffraction beamline at the Advanced Photon Source: Commissioning and early operational results. *Rev Sci Instrum* **79**, doi:Artn 085105 (2008).
- 56 Kresse, G. & Furthmüller, J. Efficiency of ab-initio total energy calculations for metals and semiconductors using a plane-wave basis set. *Computational Materials Science* **6**, 15-50 (1996).
- 57 Kresse, G. & Furthmüller, J. Efficient iterative schemes for ab initio total-energy calculations using a plane-wave basis set. *Physical Review B* **54**, 11169-11186 (1996).
- 58 Kresse, G. & Hafner, J. Ab initio molecular dynamics for liquid metals. *Physical Review B* **47**, 558-561 (1993).
- 59 Kresse, G. & Hafner, J. *Ab initio* molecular-dynamics simulation of the liquid-metal-amorphous-semiconductor transition in germanium. *Physical Review B* **49**, 14251-14269 (1994).
- 60 Blöchl, P. E. Projector augmented-wave method. *Physical Review B* **50**, 17953-17979 (1994).
- 61 Kresse, G. & Joubert, D. From ultrasoft pseudopotentials to the projector augmented-wave method. *Physical Review B* **59**, 1758-1775 (1999).
- 62 Kohn, W. & Sham, L. J. Self-Consistent Equations Including Exchange and Correlation Effects. *Physical Review* **140**, A1133 (1965).
- 63 Hinojosa, B. B., Nino, J. C. & Asthagiri, A. First-principles study of cubic Bi pyrochlores. *Physical Review B* **77**, 104123 (2008).
- 64 Pruneda, J. M. & Artacho, E. First-principles study of structural, elastic, and bonding properties of pyrochlores. *Physical Review B* **72**, 085107 (2005).

- 65 Methfessel, M. & Paxton, A. T. High-Precision Sampling for Brillouin-Zone Integration in Metals. *Physical Review B* **40**, 3616-3621 (1989).
- 66 Brisse, F. & Knop, O. Pyrochlores .3. X-Ray Neutron Infrared and Dielectric Studies of $A_2Sn_2O_7$ Stannates. *Can J Chemistry* **46**, 859-&, doi:Doi 10.1139/V68-148 (1968).
- 67 Avdeev, M., Haas, M. K., Jorgensen, J. D. & Cava, R. J. Static disorder from lone-pair electrons in $Bi_{2-x}M_xRu_2O_{7-y}$ (M=Cu,Co; x=0,0.4) pyrochlores. *J. Solid State Chem.* **169**, 24-34 (2002).
- 68 Djermouni, M., Zaoui, A., Kacimi, S. & Bouhafs, B. Vacancy defects in strontium titanate: Ab initio calculation. *Computational Materials Science* **49**, 904-909 (2010).
- 69 Lee, H. S., Mizoguchi, T., Yamamoto, T., Kang, S. J. L. & Ikuhara, Y. First-principles calculation of defect energetics in cubic-BaTiO₃ and a comparison with SrTiO₃. *Acta Materialia* **55**, 6535-6540 (2007).
- 70 Nguyen, H. B. *et al.* The disordered structures and low temperature dielectric relaxation properties of two misplaced-displacive cubic pyrochlores found in the Bi_2O_3 -M^{II}O-Nb₂O₅ (M = Mg, Ni) systems. *Journal of Solid State Chemistry* **180**, 2558-2565, doi:10.1016/j.jssc.2007.07.003 (2007).
- 71 Valant, M. Dielectric Relaxations in Bi_2O_3 -Nb₂O₅-NiO Cubic Pyrochlores. *Journal of the American Ceramic Society* **92**, 955-958, doi:10.1111/j.1551-2916.2009.02984.x (2009).
- 72 Ang, C. *et al.* Low-temperature dielectric relaxation in the pyrochlore $(Bi_{3/4}Zn_{1/4})_2(Zn_{1/4}Ta_{3/4})_2O_7$ compound. *Appl Phys Lett* **80**, 4807-4809, doi:10.1063/1.1486045 (2002).
- 73 Roth, R. S. *et al.* Pyrochlore formation, phase relations, and properties in the CaO-TiO₂-(Nb,Ta)₂O₅ systems. *Journal of Solid State Chemistry* **181**, 406-414, doi:http://dx.doi.org/10.1016/j.jssc.2007.12.005 (2008).
- 74 Hinojosa, B. B., Asthagiri, A. & Nino, J. C. Capturing dynamic cation hopping in cubic pyrochlores. *Appl Phys Lett* **99**, 082903 (2011).
- 75 Cai, L., Denev, S., Gopalan, V. & Nino, J. C. Phase Transition in Weberite-Type Gd₃NbO₇. *Journal of the American Ceramic Society* **93**, 875-880, doi:10.1111/j.1551-2916.2009.03494.x (2010).
- 76 Swainson, I. P. & Dove, M. T. Low-Frequency Floppy Modes in Beta-Cristobalite. *Phys Rev Lett* **71**, 193-196 (1993).

- 77 Wells, S. A., Dove, M. T., Tucker, M. G. & Trachenko, K. Real-space rigid-unit-mode analysis of dynamic disorder in quartz, cristobalite and amorphous silica. *J Phys-Condens Mat* **14**, 4645-4657 (2002).
- 78 Dunn, P. C. *Gateways Into Electronics*. 223-236 (John Wiley & Sons, 2000).
- 79 Singh, A. K. *Electronic Devices And Integrated Circuits*. 208-219 (Prentice-Hall of India Private Limited, 2008).
- 80 Barsoukov, E. & Macdonald, J. R. *Impedance spectroscopy : theory, experiment, and applications*. (Wiley-Interscience, 2005).
- 81 Cole, K. Dispersion and Absorption in Dielectrics I. Alternating Current Characteristics. *J. Chem. Phys.* **9**, 341 (1941).
- 82 Davidson, D. Dielectric Relaxation in Glycerol, Propylene Glycol, and n-Propanol. *J. Chem. Phys.* **19**, 1484 (1951).
- 83 Havriliak, S. & Negami, S. A complex plane representation of dielectric and mechanical relaxation processes in some polymers. *Polymer* **8**, 161-205, appendix 206-110, doi:10.1016/0032-3861(67)90021-3 (1967).
- 84 Gerhardt, R. Impedance and dielectric spectroscopy revisited: Distinguishing localized relaxation from long-range conductivity. *Journal of Physics and Chemistry of Solids* **55**, 1491-1506, doi:10.1016/0022-3697(94)90575-4 (1994).
- 85 Cao, W. & Gerhardt, R. Calculation of various relaxation times and conductivity for a single dielectric relaxation process. *Solid State Ionics* **42**, 213-221, doi:10.1016/0167-2738(90)90010-o (1990).
- 86 Kao, K. C. *Dielectric Phenomena in Solids*. 75-78 (Elsevier, 2004).
- 87 Babu, G. S. *et al.* New $(\text{Bi}_{1.88}\text{Fe}_{0.12})(\text{Fe}_{1.42}\text{Te}_{0.58})\text{O}_{6.87}$ Pyrochlore with Spin-Glass Transition. *Chemistry of Materials* **23**, 2619-2625, doi:10.1021/cm200281z (2011).
- 88 Du, H. & Yao, X. Dielectric relaxation characteristics of bismuth zinc niobate pyrochlores containing titanium. *Physica B: Condensed Matter* **324**, 121-126, doi:10.1016/s0921-4526(02)01284-x (2002).
- 89 Roth, R. S. *et al.* Pyrochlore formation, phase relations, and properties in the $\text{CaO-TiO}_2\text{-(Nb,Ta)}_2\text{O}_5$ systems. *Journal of Solid State Chemistry* **181**, 406-414, doi:10.1016/j.jssc.2007.12.005 (2008).
- 90 Christopher G. Turner, B. K., Juan C. Nino. Probing the structure of $\text{Bi}_2\text{Ti}_2\text{O}_7$ *Unpublished* (2013).

- 91 McCauley, R. A. Infrared absorption characteristics of the pyrochlore structure. *J. Opt. Soc. Amer.* **63**, 721-725, doi:10.1364/josa.63.000721 (1973).
- 92 Chen, M. H., Tanner, D. B. & Nino, J. C. Infrared study of the phonon modes in bismuth pyrochlores. *Physical Review B* **72**, doi:10.1103/PhysRevB.72.054303 (2005).
- 93 Vandendorre, M. T., Husson, E., Chatry, J. P. & Michel, D. Rare-earth titanates and stannates of pyrochlore structure; vibrational spectra and force fields. *J. Raman Spectrosc.* **14**, 63-71, doi:10.1002/jrs.1250140202 (1983).
- 94 Melot, B., Rodriguez, E., Proffen, T., Hayward, M. A. & Seshadri, R. Displacive disorder in three high-k bismuth oxide pyrochlores. *Mater Res Bull* **41**, 961-966, doi:http://dx.doi.org/10.1016/j.materresbull.2006.02.004 (2006).
- 95 Arenas, D. J. *et al.* Raman study of phonon modes in bismuth pyrochlores. *Phys Rev B* **82**, doi:Artn 214302 (2010).
- 96 Gupta, H. C., Brown, S., Rani, N. & Gohel, V. B. Lattice dynamic investigation of the zone center wavenumbers of the cubic $A_2Ti_2O_7$ pyrochlores. *Journal of Raman Spectroscopy* **32**, 41-44, doi:10.1002/1097-4555(200101)32:1<41::aid-jrs664>3.0.co;2-r (2001).
- 97 Vandendorre, M. T. & Husson, E. Comparison of the force field in various pyrochlore families. I. The $A_2B_2O_7$ oxides. *J. Solid State Chem.* **50**, 362-371, doi:10.1016/0022-4596(83)90205-0 (1983).
- 98 Patterson, C. H. First-principles calculation of the structure and dielectric properties of $Bi_2Ti_2O_7$. *Phys Rev B* **82**, doi:Artn 155103 (2010).
- 99 Lummen, T. T. A. *et al.* Phonon and crystal field excitations in geometrically frustrated rare earth titanates. *Phys Rev B* **77**, doi:Artn 214310 (2008).
- 100 Saha, S. *et al.* Temperature-dependent Raman and x-ray studies of the spin-ice pyrochlore $Dy_2Ti_2O_7$ and nonmagnetic pyrochlore $Lu_2Ti_2O_7$. *Phys. Rev. B: Condens. Matter Mater. Phys.* **78**, 214102/214101-214102/214110, doi:10.1103/PhysRevB.78.214102 (2008).
- 101 Wooten, F. *Optical properties of solids.* (Academic Press, 1972).
- 102 Henke, B. L., Gullikson, E. M. & Davis, J. C. X-Ray Interactions - Photoabsorption, Scattering, Transmission and Reflection at $E=50-30,000$ Ev, $Z=1-92$ (Vol 54, Pg 181, 1993). *Atom Data Nucl Data* **55**, 349-349 (1993).
- 103 Kumar, S. & Gupta, H. C. First principles study of zone centre phonons in rare-earth pyrochlore titanates, $RE_2Ti_2O_7$ ($RE = Gd, Dy, Ho, Er, Lu; Y$). *Vib Spectrosc* **62**, 180-187, doi:DOI 10.1016/j.vibspec.2012.06.001 (2012).

- 104 Golovshc.Gi *et al.* Relaxation Character of Dielectric Polarization in New Compounds with Pyrochlorine Type Structure near Phase-Transition. *Fiz Tverd Tela+* **14**, 2952-& (1972).
- 105 Nino, J. C., Youn, H. J., Lanagan, M. T. & Randall, C. A. Bi₂O₃ solubility of Bi-based pyrochlores and related phases. *J Mater Res* **17**, 1178-1182, doi:Doi 10.1557/Jmr.2002.0174 (2002).
- 106 Withers, R. L. *et al.* Local crystal chemistry, induced strain and short range order in the cubic pyrochlore (Bi_{1.5-α} Zn_{0.5-β})(Zn_{0.5-γ} Nb_{1.5-δ})O(7-1.5 α-β-γ-2.5-δ) (BZN). *Journal of Solid State Chemistry* **177**, 231-244, doi:DOI 10.1016/j.jssc.2003.07.005 (2004).
- 107 Hinojosa, B. B., Asthagiri, A. & Nino, J. C. Capturing dynamic cation hopping in cubic pyrochlores. *Appl Phys Lett* **99**, doi:Artn 082903 (2011).
- 108 Hinojosa, B. B., Asthagiri, A. & Nino, J. C. Energy landscape in frustrated systems: Cation hopping in pyrochlores. *Appl Phys Lett* **103**, doi:Artn 022901 (2013).
- 109 Hinojosa, B. B., Nino, J. C. & Asthagiri, A. First-principles study of cubic Bi pyrochlores. *Phys Rev B* **77**, doi:Artn 104123
Doi 10.1103/Physrevb.77.104123 (2008).
- 110 Boivin, J. C. & Mairesse, G. Recent material developments in fast oxide ion conductors. *Chem Mater* **10**, 2870-2888, doi:Doi 10.1021/Cm980236q (1998).
- 111 Harwig, H. A. Structure of Bismuthsesquioxide - Alpha,Beta,Gamma and Delta-Phase. *Z Anorg Allg Chem* **444**, 151-166, doi:DOI 10.1002/zaac.19784440118 (1978).
- 112 Kharton, V. V., Naumovich, E. N., Yaremchenko, A. A. & Marques, F. M. B. Research on the electrochemistry of oxygen ion conductors in the former Soviet Union - IV. Bismuth oxide-based ceramics. *J Solid State Electr* **5**, 160-187, doi:DOI 10.1007/s100080000141 (2001).
- 113 Iwahara, H., Esaka, T., Sato, T. & Takahashi, T. Formation of High Oxide Ion Conductive Phases in the Sintered Oxides of the System Bi₂O₃-La-Yb₂O₃. *J Solid State Chem* **39**, 173-180, doi:Doi 10.1016/0022-4596(81)90328-5 (1981).
- 114 Fung, K. Z. & Virkar, A. V. Phase-Stability, Phase-Transformation Kinetics, and Conductivity of Y₂O₃-Bi₂O₃ Solid Electrolytes Containing Alivalent Dopants. *J Am Ceram Soc* **74**, 1970-1980, doi:DOI 10.1111/j.1151-2916.1991.tb07817.x (1991).

- 115 Joshi, A. V. *et al.* Phase-Stability and Oxygen-Transport Characteristics of Yttria-Stabilized and Niobia-Stabilized Bismuth Oxide. *J Mater Sci* **25**, 1237-1245 (1990).
- 116 Hu, K., Chen, C. H., Peng, D. K. & Meng, G. Y. Bi₂O₃-Based Oxide Ion Conductors Doped with Mixed Heavy Rare-Earth-Oxides. *Solid State Ionics* **28**, 566-570, doi:Doi 10.1016/S0167-2738(88)80103-6 (1988).
- 117 Levin, E. M. & Roth, R. S. POLYMORPHISM OF BISMUTH SESQUIOXIDE .2. EFFECT OF OXIDE ADDITIONS ON POLYMORPHISM OF BI₂O₃. *Journal of Research of the National Bureau of Standards Section a-Physics and Chemistry* **A 68**, 197-+, doi:10.6028/jres.068A.020 (1964).
- 118 Ling, C. D., Withers, R. L., Schmid, S. & Thompson, J. G. A review of bismuth-rich binary oxides in the systems Bi₂O₃-Nb₂O₅, Bi₂O₃-Ta₂O₅, Bi₂O₃-MoO₃, and Bi₂O₃-WO₃. *J Solid State Chem* **137**, 42-61, doi:DOI 10.1006/jssc.1997.7677 (1998).
- 119 Tang, D. & Zhou, W. An Electron-Diffraction Study of the Type-II Bi₂-Xnbx₃O₃+X Solid-Solution. *J Solid State Chem* **119**, 311-318, doi:Doi 10.1016/0022-4596(95)80046-R (1995).
- 120 Tahara, S., Shimada, A., Kumada, N. & Sugahara, Y. Characterization of Bi₅Nb₃O₁₅ by refinement of neutron diffraction pattern, acid treatment and reaction of the acid-treated product with n-alkylamines. *J Solid State Chem* **180**, 2517-2524, (2007).
- 121 Valant, M. & Suvorov, D. Dielectric properties of the fluorite-like Bi₂O₃-Nb₂O₅ solid solution and the tetragonal Bi₃NbO₇. *J Am Ceram Soc* **86**, 939-944 (2003).
- 122 Ling, C. D. *et al.* Oxide-ionic conduction and the (3+3)-D incommensurately modulated structure of Type II Bi₂O₃-Nb₂O₅. (2013).
- 123 Wakeshima, M., Nishimine, H. & Hinatsu, Y. Crystal structures and magnetic properties of rare earth tantalates RE₃TaO₇ (RE = rare earths). *J. Phys.: Condens. Matter* **16**, 4103-4120, doi:10.1088/0953-8984/16/23/025 (2004).
- 124 Wakeshima, M. & Hinatsu, Y. Magnetic properties of lanthanide rhenium oxides Ln₃ReO₇ (Ln=Sm, Eu, Ho). *J. Solid State Chem.* **179**, 3575-3581, doi:10.1016/j.jssc.2006.07.033 (2006).
- 125 Nishimine, H., Wakeshima, M. & Hinatsu, Y. Crystal structures, magnetic and thermal properties of Ln₃IrO₇ (Ln = Pr, Nd, Sm, and Eu). *J. Solid State Chem.* **177**, 739-744, doi:10.1016/j.jssc.2003.08.036 (2004).
- 126 Cai, L. & Nino, J. C. Phase formation and dielectric properties of Ln₂(Ln'_{0.5}Nb_{0.5})₂O₇ (Ln = rare earth element). *J. Eur. Ceram. Soc.* **30**, 307-313, doi:10.1016/j.jeurceramsoc.2009.05.026 (2010).

- 127 Cai, L. & Nino, J. C. Structure and dielectric properties of Ln_3NbO_7 (Ln=Nd, Gd, Dy, Er, Yb and Y). *J. Eur. Ceram. Soc.* **27**, 3971-3976, doi:10.1016/j.jeurceramsoc.2007.02.077 (2007).
- 128 Abe, R., Higashi, M., Sayama, K., Abe, Y. & Sugihara, H. Photocatalytic Activity of R_3MO_7 and $\text{R}_2\text{Ti}_2\text{O}_7$ (R = Y, Gd, La; M = Nb, Ta) for Water Splitting into H_2 and O_2 . *J. Phys. Chem. B* **110**, 2219-2226, doi:10.1021/jp0552933 (2006).
- 129 Abe, R. *et al.* Photocatalytic Water Splitting into H_2 and O_2 over R_3TaO_7 and R_3NbO_7 (R = Y, Yb, Gd, La): Effect of Crystal Structure on Photocatalytic Activity. *J. Phys. Chem. B* **108**, 811-814, doi:10.1021/jp036300v (2004).
- 130 Cai, L. & Nino, J. C. Complex ceramic structures. I. Weberites. *Acta Crystallogr., Sect. B: Struct. Sci.* **B65**, 269-290, doi:10.1107/s0108768109011355 (2009).
- 131 Cai, L. *Fundamental Structure-Dielectric Property Relationships in Fluorite-Related Ceramics* PhD thesis, University of Florida, (2010).
- 132 Shannon, R. D. Revised Effective Ionic-Radii and Systematic Studies of Interatomic Distances in Halides and Chalcogenides. *Acta Crystallogr A* **32**, 751-767, doi:Doi 10.1107/S0567739476001551 (1976).
- 133 Astafyev, A. V., Sirotkin, V. P. & Stefanovich, S. Y. PHASE-TRANSITIONS IN THE COMPOUNDS SM_3NBO_7 AND GD_3NBO_7 WITH A FLUORITE-LIKE STRUCTURE. *Kristallografiya* **30**, 603-604 (1985).
- 134 Harrop, P. J. Temperature Coefficients of Capacitance of Solids. *J Mater Sci* **4**, 370-&, doi:Doi 10.1007/Bf00550407 (1969).
- 135 Brown, I. D. *The Chemical Bond in Inorganic Chemistry: The Bond Valence Model.* (Oxford University Press, Incorporated, 2006).
- 136 Castro, A. *et al.* The New Oxygen-Deficient Fluorite Bi_3NbO_7 : Synthesis, Electrical Behavior and Structural Approach. *Mater Res Bull* **33**, 31-41, (1998).
- 137 Doi, Y., Harada, Y. & Hinatsu, Y. Crystal structures and magnetic properties of fluorite-related oxides Ln_3NbO_7 (Ln=lanthanides). *Journal of Solid State Chemistry* **182**, 709-715, doi:http://dx.doi.org/10.1016/j.jssc.2008.12.012 (2009).
- 138 Makoto, W., Hiroaki, N. & Yukio, H. Crystal structures and magnetic properties of rare earth tantalates RE_3TaO_7 (RE = rare earths). *Journal of Physics: Condensed Matter* **16**, 4103 (2004).
- 139 Nishimine, H., Wakeshima, M. & Hinatsu, Y. Crystal structures, magnetic and thermal properties of Ln_3IrO_7 (Ln=Pr, Nd, Sm, and Eu). *J Solid State Chem* **177**, 739-744, doi:http://dx.doi.org/10.1016/j.jssc.2003.08.036 (2004).

- 140 Cai, L. & Nino, J. C. Structure and dielectric properties of Ln_3NbO_7 ($\text{Ln}=\text{Nd, Gd, Dy, Er, Yb}$ and Y). *Journal of the European Ceramic Society* **27**, 3971-3976, doi:<http://dx.doi.org/10.1016/j.jeurceramsoc.2007.02.077> (2007).
- 141 Ebbinghaus Stefan, G., Kalytta, A., Kopf, J., Weidenkaff, A. & Reller, A. in *Zeitschrift für Kristallographie/International journal for structural, physical, and chemical aspects of crystalline materials* Vol. 220 269 (2005).
- 142 Abe, R. *et al.* Photocatalytic Water Splitting into H_2 and O_2 over R_3TaO_7 and R_3NbO_7 ($\text{R} = \text{Y, Yb, Gd, La}$): Effect of Crystal Structure on Photocatalytic Activity. *The Journal of Physical Chemistry B* **108**, 811-814, doi:10.1021/jp036300v (2003).
- 143 Abe, R., Higashi, M., Sayama, K., Abe, Y. & Sugihara, H. Photocatalytic Activity of R_3MO_7 and $\text{R}_2\text{Ti}_2\text{O}_7$ ($\text{R} = \text{Y, Gd, La}$; $\text{M} = \text{Nb, Ta}$) for Water Splitting into H_2 and O_2 . *The Journal of Physical Chemistry B* **110**, 2219-2226, doi:10.1021/jp0552933 (2006).
- 144 Lin, X. *et al.* Photocatalytic activities of $\text{M}_2\text{Sb}_2\text{O}_7$ ($\text{M}=\text{Ca, Sr}$) for degrading methyl orange. *Applied Catalysis A: General* **313**, 218-223, doi:<http://dx.doi.org/10.1016/j.apcata.2006.08.001> (2006).
- 145 Allpress, J. G. & Rossell, H. J. Fluorite-Related Phases Ln_3MO_7 , $\text{Ln} = \text{Rare Earth, Y, or Sc}$, $\text{M} = \text{Nb, Sb, or Ta}$. I. Crystal Chemistry. *J Solid State Chem* **27**, 105-114 (1979).
- 146 Nishimine, H., Doi, Y., Hinatsu, Y. & Sato, M. Phase Transition of Ln_3IrO_7 ($\text{Ln}=\text{Pr, Nd, Sm, Eu}$) and its Low-Temperature Structure. *Journal of the Ceramic Society of Japan* **115**, 577-581 (2007).
- 147 Gemmill, W. R., Smith, M. D., Mozharivsky, Y. A., Miller, G. J. & zur Loye, H.-C. Crystal Growth, Structural Transitions, and Magnetic Properties of the Fluorite-Related Osmates: Sm_3OsO_7 , Eu_3OsO_7 , and Gd_3OsO_7 . *Inorg Chem* **44**, 7047-7055, doi:10.1021/ic0506106 (2005).
- 148 Greedan, J. E., Raju, N. P., Wegner, A., Gougeon, P. & Padiou, J. A Study of the Structure and Electronic and Thermal Properties of Quasi-One-Dimensional La_3MoO_7 . *J Solid State Chem* **129**, 320-327, doi:<http://dx.doi.org/10.1006/jssc.1996.7259> (1997).
- 149 Klimenko, A. N., Ionov, V. M., Tomilin, N. A., Sergeev, V. S. & Sirotkin, V. P. PHASE-TRANSFORMATIONS IN RARE-EARTH-METALS OF R_3NBO_7 NIOBATES AT HIGH-TEMPERATURES. *ZHURNAL NEORGANICHESKOI KHIMII* **35**, 599-603 (1990).

- 150 Bontchev, R., Jacobson, A. J., Gospodinov, M. M., Skumryev, V. & Popov, V. N. Crystal structure, electric and magnetic properties, and Raman spectroscopy of Gd₃RuO₇. *Physical review. B, Condensed matter* **62**, 12235-12240, doi:10.1103/PhysRevB.62.12235 (2000).
- 151 Bokov, A. A., Leshchenko, M. A., Malitskaya, M. A. & Raevski, I. P. Dielectric spectra and Vogel-Fulcher scaling in Pb(In_{0.5}Nb_{0.5})O₃ relaxer ferroelectric. *J Phys-Condens Mat* **11**, 4899-4911, doi:Doi 10.1088/0953-8984/11/25/309 (1999).
- 152 Elissalde, C., Ravez, J. & Gaucher, P. Dielectric Relaxations in Ceramics with Compositions (1-X)Pb(Mg_{1/3}Nb_{2/3})O₃-Xpbtio(3) (X=0, 0.05, 0.10 and 0.25). *Mat Sci Eng B-Solid* **22**, 303-309, doi:Doi 10.1016/0921-5107(94)90261-5 (1994).
- 153 Cheng, B. L. *et al.* Temperature stability of permittivity and dielectric relaxation in multilayered thin films of (Ba_{0.80}Sr_{0.20})(Ti_{1-x}Zr_x)O₃ with a compositionally graded layer. *Appl Phys Lett* **84**, 5431-5433, doi:Doi 10.1063/1.1767605 (2004).
- 154 Johnson, H. B., Tolar, N. J., Miller, G. R. & Cutler, I. B. Electrical and Mechanical Relaxation in CaF₂ Doped with NaF. *Journal of Physics and Chemistry of Solids* **30**, 31-&, doi:Doi 10.1016/0022-3697(69)90336-9 (1969).
- 155 Nishimine, H., Doi, Y., Hinatsu, Y. & Sato, M. Phase transition of Ln₃IrO₇ (Ln = Pr, Nd, Sm, Eu) and its low-temperature structure. *J Ceram Soc Jpn* **115**, 577-581, doi:DOI 10.2109/jcersj2.115.577 (2007).
- 156 Barrier, N., Gall, P. & Gougeon, P. Rare-earth site splitting in Sm₃MoO₇. *Acta Crystallogr C* **63**, I102-I104, doi:Doi 10.1107/S0108270107045416 (2007).
- 157 Harada, D., Hinatsu, Y. & Ishii, Y. Studies on the magnetic and structural phase transitions of Nd₃RuO₇. *J Phys-Condens Mat* **13**, 10825-10836, doi:Doi 10.1088/0953-8984/13/48/308 (2001).
- 158 Allpress, J. G. & Rossell, H. J. Fluorite-related phases Ln₃MO₇, Ln = rare earth, Y, or Sc, M = Nb, Sb, or Ta. I. Crystal chemistry. *Journal of Solid State Chemistry* **27**, 105-114, doi:http://dx.doi.org/10.1016/0022-4596(79)90149-X (1979).
- 159 Wakeshima, M., Nishimine, H. & Hinatsu, Y. Crystal structures and magnetic properties of rare earth tantalates RE₃TaO₇ (RE = rare earths). *J. Phys.: Condens. Matter* **16**, 4103-4120, doi:10.1088/0953-8984/16/23/025 (2004).
- 160 Yokogawa, Y., Yoshimura, M. & Sōmiya, S. Order-disorder in R₃TaO₇ (R=rare earth) phases. *Solid State Ionics* **28-30, Part 2**, 1250-1253, doi:http://dx.doi.org/10.1016/0167-2738(88)90365-7 (1988).
- 161 Shannon, R. D. & Fischer, R. X. Empirical electronic polarizabilities in oxides, hydroxides, oxyfluorides, and oxychlorides. *Phys Rev B* **73**, 235111 (2006).

- 162 Vanderah, T. A., Guzman, J., Nino, J. C. & Roth, R. S. Stability Phase-Fields and Pyrochlore Formation in Sections of the $\text{Bi}_2\text{O}_3\text{-Al}_2\text{O}_3\text{-Fe}_2\text{O}_3\text{-Nb}_2\text{O}_5$ System. *Journal of the American Ceramic Society* **91**, 3659-3662, doi:10.1111/j.1551-2916.2008.02648.x (2008).
- 163 Osman, R. A. M. & West, A. R. Electrical characterization and equivalent circuit analysis of $(\text{Bi}(1.5)\text{Zn}(0.5))(\text{Nb}(0.5)\text{Ti}(1.5))\text{O}(7)$ Pyrochlore, a relaxor ceramic. *Journal of Applied Physics* **109**, doi:10.1063/1.3553883 (2011).
- 164 Osman, R. A. M., Maso, N. & West, A. R. Bismuth Zinc Niobate Pyrochlore, a Relaxor-Like Non-Ferroelectric. *Journal of the American Ceramic Society* **95**, 296-302, doi:10.1111/j.1551-2916.2011.04779.x (2012).
- 165 Macdonald, J. R. Impedance Spectroscopy. *Ann Biomed Eng* **20**, 289-305 (1992).
- 166 Osman, R. A. M. & West, A. R. Electrical characterization and equivalent circuit analysis of $(\text{Bi}1.5\text{Zn}0.5)(\text{Nb}0.5\text{Ti}1.5)\text{O}7$ Pyrochlore, a relaxor ceramic. *J Appl Phys* **109**, 074106, doi:10.1063/1.3553883 (2011).
- 167 Osman, R. A. M., Masó, N., West, A. R. & Johnson, D. W. Bismuth Zinc Niobate Pyrochlore, a Relaxor-Like Non-Ferroelectric. *Journal of the American Ceramic Society* **95**, 296-302, doi:10.1111/j.1551-2916.2011.04779.x (2012).

BIOGRAPHICAL SKETCH

Christopher Turner was born in Santiago, Chile in 1987. He has since lived in Redondo Beach (California, USA), Sao Paulo (Brazil), Bangkok (Thailand) and finally Weston, Florida in 2004 where he graduated from Cypress Bay High School in 2006. Christopher began attending the University of Florida the following June and graduated with a B.S. in Materials Science and Engineering, specializing in Biomaterials, in May of 2010. In 2011, he began his Ph.D. studies in Dr. Juan C. Nino's research group. After spending nearly 8 years and 3 national championships at UF in Gainesville, he received his Ph.D. in the Spring of 2014.